Tip-Enhanced Optical Spectroscopy:

Resonance, Hotspot, Imaging, and Radiation

Dissertation

der Mathematisch-Naturwissenschaftlichen Fakultät

der Eberhard Karls Universität Tübingen

zur Erlangung des Grades eines

Doktors der Naturwissenschaften

(Dr. rer. nat.)

vorgelegt von

Yu-Ting Chen

aus Taichung/Taiwan

Tübingen

2021

Gedruckt mit Genehmigung der Mathematisch-Naturwissenschaftlichen Fakultät der Eberhard Karls Universität Tübingen.

Tag der mündlichen Qualifikation:	20.01.2022
Dekan:	Prof. Dr. Thilo Stehle
1. Berichterstatter:	Prof. Dr. Alfred Meixner
2. Berichterstatterin:	Prof. Dr. Monika Fleischer
3. Berichterstatterin:	PD Dr. Dai Zhang

The dissertation is dedicated to my parents …

Abstract

The work aims to deepen the understanding of light-matter interaction at the nanometer scale using home-built confocal and tip-enhanced (TE) optical spectroscopy with apertureless scanning near-field optical microscopy (aSNOM). This technique achieves high spatial resolution beyond the diffraction limit utilizing the strong local field enhancement in the vicinity of the Au tip. TE Raman and photoluminescence (PL) from Metal-Phthalocyanine (Pc) molecular thin film (CuPc, CoPc) adsorbed on single-crystal Au or nanostructured Au are investigated. By performing approach curves of the optical signals, the enhancement for the TE Raman and PL can be revealed. By implementing the back-focal plane (BFP) imaging technique with a high-numerical-aperture (NA) parabolic mirror (PM), the radiation properties of the Au tip and the plasmonic gap are observed. By carrying out electrodynamics simulations in the FDTD scheme, quantitative insights into the measurements are provided.

Chapter 1 provides a general introduction to microscopy and tip-enhanced spectroscopy. Fundamentals of the Raman effect and related optical spectroscopy are introduced. The principle of surface-enhanced (SE) and tip-enhanced (TE) spectroscopy is elaborated in the following works. Higher-order laser modes are fundamental in optical microscopy, whose focal fields are explicitly expressed and visualized. The Hertz dipole radiation and the dipole antennas of different lengths are formulated and visualized. Electrodynamics simulations in the finite-difference time-domain (FDTD) scheme are introduced with practical examples.

Chapter 2 studies surface plasmon resonance (SPR), charge transfer (CT) resonance, and molecular resonance by two-color SERS and TERS using Au nanodisks (NDs). The Au NDs array with the molecular thin film deposited exhibits SERS and TERS effects in imaging and corresponding optical spectra by two-color excitation (532 and 636 nm). The three contributions to SERS are presented with an analytic expression and discussed factor by factor.

Chapter 3 reveals the gap-dependent optical signals in the Au tip-Au substrate configuration. The variable gap between Au tip and Au substrate enables one to reveal the enhancement process. The Raman enhancements and background emission are observed and discussed with nice agreement with FDTD simulations.

Chapter 4 The fine structure of a CuPc film is investigated with sub-10 nm optical resolution by tip-enhanced microscopy and spectroscopy. The TE optical images are inversely correlated to topography. This inverse correlation between optical and topography is compared with the FDTD simulations. Fundamental mechanisms of imaging at the nanometer scale are discussed.

Chapter 5 unravels the radiation patterns of the plasmonic gap. Radiation is experimentally and systematically realized by BFP imaging. The plasmonic modes on Au tapers are discussed. The electric fields calculated by FDTD simulations with radial polarization as the source are visualized. The radiation of the conical taper is unraveled with the reciprocal picture of adiabatic compression. The geometry and the tilted tip or tilted substrate can influence the emission patterns. The BFP imaging with the on-axis parabolic mirror of high numerical aperture (NA) can capture the angular distributions of radiation. Based upon the FDTD simulations, we can predict the influence of the tilted geometry.

The resonant behaviors in the EM enhancement and the chemical enhancement in SERS and TERS are revealed. The evolution of Raman scattering with varying gap sizes is explored. The optical spatial resolution of sub-10 nm is realized and agrees with the simulations. The radiation properties of the Au taper are revealed by BFP imaging. The far-field contributions from the plasmonic gap are discussed. All these works provide more insights into spectroscopy and microscopy at the nanometer scale, which helps people to design and develop new optical techniques in the relevant fields.

Zusammenfassung

Die Arbeit zielt darauf ab, das Verständnis der Licht-Materie-Wechselwirkung im Nanometerbereich mithilfe von selbstgebauter konfokaler und spitzenverstärkter (TE) optischer Spektroskopie mit aperturloser optischer Nahfeldmikroskopie (aSNOM) zu vertiefen. Diese Technik erreicht eine hohe räumliche Auflösung über die Beugungsgrenze hinaus unter Ausnutzung der starken lokalen Feldverstärkung in der Nähe der Au-Spitze. TE Raman und PL von molekularen Metall-Pc-Dünnfilmen (CuPc, CoPc) auf einkristallinem Au oder nanostrukturiertem Au werden untersucht. Durch Durchführen von Annäherungskurven optischer Signale kann die Verbesserung für TE Raman und PL aufgedeckt werden. Durch Implementierung der Back-Focal-Plane (BFP)-Abbildungstechnik mit einem Parabolspiegel mit hoher numerischer Apertur (NA) werden die Strahlungseigenschaften der Au-Spitze und der plasmonischen Lücke beobachtet. Durch die Durchführung der elektrodynamischen Simulationen im FDTD-Schema werden quantitative Einblicke in die Messungen geliefert.

Kapitel 1 bietet eine allgemeine Einführung in die Mikroskopie und die spitzenverstärkte Spektroskopie. Grundlagen des Raman-Effekts und der damit verbundenen optischen Spektroskopie werden eingeführt. Das Prinzip der oberflächenverstärkten (SE) und spitzenverstärkten (TE) Spektroskopie wird in den folgenden Arbeit erläutert. Lasermoden höherer Ordnung sind grundlegend in der optischen Mikroskopie, deren Fokusfelder explizit ausgedrückt und visualisiert werden. Die Hertz-Dipolstrahlung und die Dipolantennen unterschiedlicher Länge werden formuliert und visualisiert. Elektrodynamische Simulationen im Finite-Difference-Time-Domain-(FDTD)-Schema werden mit praktischen Beispielen eingeführt.

Kapitel 2 untersucht die Oberflächenplasmonenresonanz (SPR), die Charge-Transfer-Resonanz (CT) und die molekulare Resonanz durch zweifarbige SERS und TERS unter Verwendung von Au-Nanoscheiben (NDs). Das Au-NDs-Array mit dem abgeschiedenen molekularen Dünnfilm zeigt SERS- und TERS-Effekte bei der Bildgebung

und entsprechende optische Spektren durch Zweifarbenanregung (532 und 636 nm). Die drei Beiträge zu SERS werden mit einem analytischen Ausdruck dargestellt und Faktor für Faktor diskutiert.

Kapitel 3 zeigt die lückenabhängigen optischen Signale in der Spitze-Au-Substrat Konfiguration. Der variable Abstand zwischen Au-Spitze und Au-Substrat ermöglicht es, den Kopplungsprozess aufzudecken. Die Raman-Verstärkungen und die Hintergrundemission werden beobachtet und mit ausgezeichneter Übereinstimmung mit FDTD-Simulationen diskutiert.

Kapitel 4 Die Feinstruktur von CuPc-Filmen wird mit einer optischen Auflösung von weniger als 10 nm durch spitzenverstärkte Mikroskopie und Spektroskopie untersucht. Die optischen TE-Bilder sind invers mit der Topographie korreliert. Diese inverse Korrelation zwischen Optik und Topographie wird mit FDTD-Simulationen verglichen. Grundlegende Mechanismen der Bildgebung im Nanometerbereich werden diskutiert.

Kapitel 5 enträtselt die Strahlungsmuster der plasmonischen Lücke. Strahlung wird experimentell und systematisch durch BFP-Bildgebung realisiert. Die plasmonischen Moden auf Au-Tapern werden diskutiert. Die durch FDTD-Simulationen berechneten elektrischen Felder mit radialer Polarisation als Quelle werden visualisiert. Die Strahlung der Kegelverjüngung wird mit dem reziproken Bild der adiabatischen Kompression entwirrt. Die Geometrie und die geneigte Spitze oder das geneigte Substrat können die Emissionsmuster beeinflussen. Die BFP-Bildgebung mit dem auf der Achse liegenden Parabolspiegel mit hoher numerischer Apertur (NA) kann die Winkelverteilungen der Strahlung erfassen. Basierend auf den FDTD-Simulationen können wir den Einfluss der geneigten Geometrie vorhersagen.

Das Resonanzverhalten bei der EM-Verstärkung und der chemischen Verstärkung in SERS und TERS wird aufgezeigt. Es wird die Entwicklung der Raman-Streuung bei unterschiedlichen Spaltgrößen untersucht. Die optische Ortsauflösung von sub-10 nm wird realisiert und stimmt mit den Simulationen überein. Die Strahlungseigenschaften des Au-Tapers werden durch BFP-Bildgebung aufgedeckt. Die Fernfeldbeiträge der plasmonischen Lücke werden diskutiert. Alle diese Arbeiten bieten weitere Einblicke in

die Spektroskopie und Mikroskopie im Nanometerbereich, die den Menschen helfen, neue optische Techniken in relevanten Bereichen zu entwerfen und zu entwickeln.

Contents

Abbreviations

1D	One dimension
2D	Two dimensions
3D	Three dimensions
NA	numerical aperture
Au	gold
UHV	Ultra-high vacuum
LSP	Localized surface plasmons
SPR	Surface plasmon resonance
SPPs	Surface plasmon polaritons
SERS	Surface-enhanced Raman scattering/spectroscopy
SMSERS	Single-molecule Surface-enhanced Raman scattering/spectroscopy
SE	Surface-enhanced
SNOM	Scanning near-field optical microscope
aSNOM	Apertureless scanning near-field optical microscope
QFT	Quartz tuning fork
TEOS	Tip-enhanced optical spectroscopy
TERS	Tip-enhanced Raman scattering/spectroscopy
TE	Tip-enhanced
TER	Tip-enhanced Raman
CE	Chemical enhancement

EM	Electromagnetic
APD	Avalanche photodiode
LN_2	Liquid Nitrogen
CoPc	Cobalt Phthalocyanine
CuPc	Cupper Phthalocyanine
fwhm	full width at half maximum
APDM	azimuthally polarized doughnut mode
RPDM	radially polarized doughnut mode
QY	quantum yield
PL	photoluminescence
EL	electroluminescence
CL	cathodeluminescence
PDE	partial differential equations
FEM	Finite Element Method
FDTD	Finite Difference Time Domain
PML	perfectly matched layer
SRR	split-ring resonator
ROC	radius of curvature
fs	femtosecond

Chapter 1
Introduction

"There's plenty of room at the bottom."[1] was given by the Nobel prize laureate, R. Feynman, who has enlightened us in nanoscience manufacturing and characterizations all the time. Science and technology at the nanometer scale are fast-growing during these decades, which is driven by miniaturization and the integration of electronic circuits in electronic devices. This year Taiwan Semiconductor Manufacture Company (TSMC) with leading-edge fabs put 3-nm semiconductor node into commercial production for chips in laptops, smartphones, and even self-driving cars. As the dimension becomes smaller and smaller, new physical effects will become notable. Acquisition of fundamental understanding in nanoscience using the optical microscope plays a vital role in nanotechnology and can even shape our way of life.

Tip-enhanced optical spectroscopy (TEOS) and microscopy enable us to observe fine structures optically at the nanometer scale well beyond confocal microscopy. TEOS is an overlap of plasmonics, scanning probe microscopy, and optical spectroscopy, including Raman and luminescence spectroscopy. Optical spectroscopy reveals the optical responses from the molecule. Raman spectroscopy helps one to chemically specify molecules. The interaction of light at the surface of metals significantly amplifies the optical intensity due to the surface plasmons (SPs). Scanning probe microscopy (SPM) equips us to observe the surface properties of materials at the nanometer scale. The TEOS enables one to perform high-resolution optical imaging.

Next, we will show the basic background knowledge related to TEOS step by step, including optical microscopy, Raman spectroscopy, physics of the SPs, and surface- or tip-enhanced Raman spectroscopy. Higher-order laser modes as excitation come to play a critical role in field enhancement in the near-field regions. The dipole radiation describes the fundamental physics of a single emitter. Electrodynamics simulations in the finite-difference time-domain (FDTD) scheme are introduced for providing quantitative insights into the plasmon-enhanced light-matter interactions.

1.1 Optical Microscopy

With electron microscopes, scanning probe microscopes, and focused ion beam milling systems, we can characterize, manipulate nanostructures with high magnification and precision. Undoubtedly, optical microscopes are great tools to reveal fine features in small objects in a noncontact way. A prototype of an optical microscope is done by Galilei[2] in the 17th century, and the theory of optical resolution in the optical microscope are formulated by Abbe[3] and Rayleigh[4].

If NA denotes the numerical aperture of the objective, then the minimum lateral distance d for distinguishing two point objects is given by [2, 5]

$$d \sim 0.6098 \cdot \frac{\lambda}{NA} \tag{1-1}$$

where the λ is the wavelength. Thus, the resolution by a conventional optical microscope is limited to roughly 200 nm.

Confocal microscopy[6] and super-resolution fluorescence microscopy were invented to surpass the diffraction limit. Several approaches have been developed for super-resolution fluorescence microscopy, e.g. stimulated emission depletion microscopy (STED)[7, 8], saturated structured-illumination microscopy (SSIM)[9], stochastic optical reconstruction microscopy (STORM)[10], and fluorescence photoactivation localization microscopy (FPALM)[11]. Super-resolution microscopy is developed to image biological

samples well beyond the diffraction limit while relying on specific fluorophores and technologies[12].

Another alternative approach is scanning near-field optical microscopy (SNOM), which can optically and topographically image nano-objects by bringing a probe in the proximity to the sample surface with high spatial resolution. SNOM was firstly proposed by Synge[13] and later was experimentally realized by Ash and Nichols[14] in the microwave frequency range. SNOM operated at optical frequencies was presented[15] and by Lewis *et al*[16] independently in the same year. SNOM with an apertureless probe (aSNOM) is utilized in spectroscopy and over the decades, various techniques were developed, which all utilize highly concentrated photon intensity between sample and probe to enhance optical resolution. These techniques help us to explore the light-matter interactions at the nanometer scale with deeper insight.

1.2 Raman Spectroscopy

Raman spectroscopy is based upon the analysis of inelastic scatterings from molecules or solids. This type of inelastic scattering was discovered by C.V. Raman. Here, we introduce the general concept of optical spectroscopy and before we enter Raman spectroscopy in the remainder of the section.

1.2.1 Absorption and Fluorescence Spectroscopy

Jablonski Diagram

A Jablonski diagram offers a straightforward way to visualize the transitions between different electronic states[17-21] as shown in Figure 1.1. The electrons occupy their lowest energy state (permitted by the Pauli exclusion principle) for a molecule in its ground electronic state. Generally speaking, all electrons are paired with two electrons of opposite spins. The ground state is then called a *singlet state* (S_0), which denotes that this state has zero total spins. The Pauli exclusion principle no more prohibits the two electrons from having the same spin as one electron in a pair is transferred to its excited state.

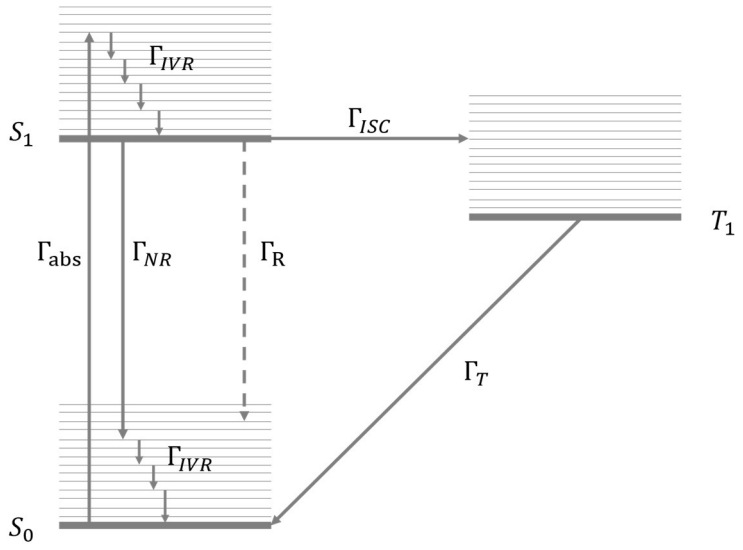

Figure 1.1 Jablonski diagram of a molecule[20]. The arrows indicate electronic transitions between different states.

The electronically excited state gives four degeneracies since there are four possible spin states. These spin states are grouped as: a *singlet state* (S_1) corresponding to the only excited state configuration with a total spin of zero, and a *triplet state* (T_1) corresponding to a triply-degenerate excited state with a total spin of one. In the Jablonski diagram, the electronic states are arranged vertically by increasing energy and grouped horizontally by spin multiplicity. Equivalently, the triplet state is presented to the right of the singlet state S_1, itself represented above S_0. Particularly, the triplet state T_1 is not degenerate with S_1 and normally lies below S_1 in terms of energy.

Luminescence

If a transition between two different electronic states occurs, it is called an electronic transition. The transitions between two states in the sub-structure of the same electronic state are called *internal* or *vibrational transitions*. After absorption of a photon that prompts the molecule from the ground state to the excited state, both radiative transition (luminescence) and non-radiative decay occur. These two processes compete and are further quantified as the *quantum yield* (QY)[20] Φ

$$\Phi = \frac{\Gamma_R}{\Gamma_R + \Gamma_{NR}} \tag{1-2}$$

where Γ_R denotes radiative decay rate and Γ_{NR} denotes non-radiative decay rate as shown in Figure 1.1.

Photoluminescence (PL) is a process that a molecule emits photons after absorption. If the emission process is induced in response to a current, then the process is called electroluminescence (EL).

Radiative transitions are generally forbidden between singlet and triplet states because a photon cannot induce a change in the total spin. However, intersystem crossing (ISC) may not be prohibited as a spin relaxation mechanism exists (e.g. spin-orbit coupling). The transitions from the triplet state T_1 to singlet state S_1 (Γ_T) is phosphorescence, which often decays with a long lifetime.

Non-radiative transitions may stem from interactions with the environment (solvent, other molecules) or other internal interactions. Intra-molecular vibrational redistribution (IVR)[22, 23] secures relaxation from excited vibrational states to the ground vibrational state as indicated as Γ_{IVR} in Figure 1.1.

More detailed descriptions of the transitions can be found in the books[18, 20].

1.2.2 Fundamentals of the Raman Effect

In addition to the absorption and the luminescence processes that occur in a molecule in response to incident photons, the inelastic scattering, the Raman effect, is introduced here from a phenomenological point of view[20]. Let us consider a molecule in a static field. The *change with respect to equilibrium* is defined as the induced static dipole, which is defined as[20]

$$\vec{p}_{static} = \vec{\vec{\alpha}}_{static} \cdot \vec{E} \tag{1-3}$$

where $\overleftrightarrow{\alpha}_{static}$ denotes the static polarizability tensor. Due to the tensorial effect of $\overleftrightarrow{\alpha}_{static}$, $\vec{p}_{static}$ and $\vec{E}$ may not be parallel to each other.

It is worth noting that some molecules have a *permanent dipole* in absence of an applied field. This results from the symmetry of the wave functions in the ground state at equilibrium. The dipole $\vec{p}_n$ is not related to the permanent dipole, but exhibits the change in dipole moment with respect to equilibrium. This dipole $\vec{p}_n$ is named as an *induced dipole*.

Let us consider Stokes Raman scattering from a dipole from an energy $\hbar\omega_\nu$. The Raman scattering at an angular frequency is denoted as $\omega_R = \omega_L - \omega_\nu$ with the incident field angular frequency ω_L. Then the induced Raman dipole in response to $\vec{E}(\omega_L)$ can be written as

$$\vec{p}_R(\omega_R) = \overleftrightarrow{\alpha}_R \cdot \vec{E}(\omega_L) \tag{1-4}$$

The $\overleftrightarrow{\alpha}_R$ is called *Raman polarizability tensor*, which does not depend on time. A prefactor needs to be introduced to correct the dipole response in a liquid[20], which is omitted in the following content. The $\overleftrightarrow{\alpha}_R$ is a second-rank tensor, which represents the linear relation between two vectors and is written as

$$\begin{pmatrix} p_x \\ p_y \\ p_z \end{pmatrix} = \begin{pmatrix} \alpha_{xx} & \alpha_{xy} & \alpha_{xz} \\ \alpha_{yx} & \alpha_{yy} & \alpha_{yz} \\ \alpha_{zx} & \alpha_{zy} & \alpha_{zz} \end{pmatrix} \begin{pmatrix} E_x \\ E_y \\ E_z \end{pmatrix} \tag{1-5}$$

Normally, the $\overleftrightarrow{\alpha}_R$ is symmetric, i.e. $\alpha_{ij} = \alpha_{ji}$ except for some cases[20]. And it can be diagonalized as

$$\begin{pmatrix} p_{x'} \\ p_{y'} \\ p_{z'} \end{pmatrix} = \begin{pmatrix} \alpha_{x'x'} & 0 & 0 \\ 0 & \alpha_{y'y'} & 0 \\ 0 & 0 & \alpha_{z'z'} \end{pmatrix} \begin{pmatrix} E_{x'} \\ E_{y'} \\ E_{z'} \end{pmatrix} \tag{1-6}$$

The transformed axes are called principle axes, which are attached to the molecule. Thus, it can be seen that the induced dipole depends on polarizability and orientation of the molecule as well.

1.2.3 Differential Raman Scattering Cross-Section

Radiated Power

The electromagnetic (EM) field by an oscillating dipole will be described in Section 1.6 and Appendix B for details. Here, the most important aspect presented here is the radiated power in the far-field regions. For a dipole aligned along the z-axis, the dipole moment is expressed as $\vec{p} = p\hat{e}_z$. The differential radiated power at solid angle $\Omega(\theta, \phi)$ in the spherical coordinate can be written as[24]

$$\frac{dP}{d\Omega}(\Omega) = \frac{\omega^4}{32\pi^2\varepsilon_0 c^3}|p|^2 \sin^2\theta \tag{1-7}$$

Let us consider an induced Raman dipole $\vec{p}_R = \vec{\vec{\alpha}}_1 \cdot \vec{E}_{inc}$ with the incident field $\vec{E}_{inc}$ polarized along $\hat{e}_{inc}$. The scattered field is detected by a polarizer along the direction $\hat{e}_P$. The detected differential radiated power $\frac{dP_R}{d\Omega}$ of Raman of a fixed orientation at $\theta = 90°$ can be written as

$$\frac{dP_R}{d\Omega}(\theta = 90°) = \frac{\omega_R^4}{32\pi^2\varepsilon_0 c^3}|\hat{e}_P \cdot \alpha \cdot \hat{e}_{inc}|^2 \cdot \left|\vec{E}_{inc}\right|^2 \tag{1-8}$$

where ω_R denotes the Raman frequency of a Raman mode.

Then the scattered radiation from a fixed molecule can be measured according to this expression. For example, if the incident field is polarized along x, $\hat{e}_{in} \parallel \hat{e}_x$, and propagates from z towards the molecule (placed at the origin), the scattered signals propagating in y and detected by a polarized analyzer along x ($\hat{e}_p \parallel \hat{e}_x$) will be $\propto |\alpha_{xx}|^2$. The process is illustrated in Figure 1.2. Likewise, if the analyzer is turned to be polarized along y, then the scattered signals will be $\propto \left|\alpha_{yx}\right|^2$.

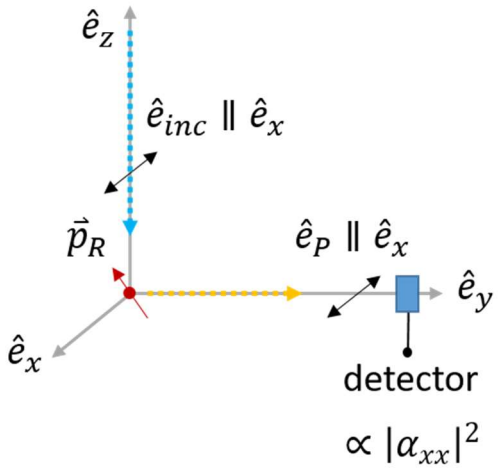

Figure 1.2 Detected differential power of the Raman dipole $\vec{p}_R$. The incident field propagates along $\hat{e}_{inc} \parallel \hat{e}_x$ (blue dashed line) and the scattered field along the y axis (yellow dashed line) is detected with a analyzer polarized along x, $\hat{e}_P \parallel \hat{e}_x$.

Averaging Over all Orientations

Definition of differential scattering requires consideration of molecules with random orientations. Let us consider an incident excitation along $\hat{e}_x$ polarized along $\hat{e}_z$. The scattered signals are detected by a polarized along $\hat{e}_z$. The differential radiated power detected at 90° per molecule with random orientations can then be written as

$$\frac{dP_R^{\parallel}}{d\Omega}(\theta = 90°) = \frac{\omega_R^4}{32\pi^2\varepsilon_0 c^3}\langle|\hat{e}_z \cdot \alpha \cdot \hat{e}_z|^2\rangle \cdot \left|\vec{E}_{inc}\right|^2 \qquad (1\text{-}9)$$

where the angle bracket denotes averaging all orientations.

The corresponding differential scattering cross-section for parallel detection $\frac{d\sigma_R^{\parallel}}{d\Omega}$ and for perpendicular detection $\frac{d\sigma_R^{\perp}}{d\Omega}$ are

$$\frac{d\sigma_R^{\parallel}}{d\Omega} = \frac{\omega_R^4}{16\pi^2{\varepsilon_0}^2 c^3}\langle|\hat{e}_z \cdot \alpha \cdot \hat{e}_z|^2\rangle \qquad (1\text{-}10)$$

$$\frac{d\sigma_R^{\perp}}{d\Omega} = \frac{\omega_R^4}{16\pi^2{\varepsilon_0}^2c^3}\langle\left|\hat{e}_y \cdot \alpha \cdot \hat{e}_z\right|^2\rangle \tag{1-11}$$

The factors $\langle|\hat{e}_z \cdot \alpha \cdot \hat{e}_z|^2\rangle$ and $\langle\left|\hat{e}_y \cdot \alpha \cdot \hat{e}_z\right|^2\rangle$ are independent of the choice of $\hat{e}_y$ or $\hat{e}_z$ due to orientational averaging. With group theory[25-28], these factors will depend on symmetry invariants. The differential scattering cross-sections $\frac{d\sigma_R^{\parallel}}{d\Omega}$ and $\frac{d\sigma_R^{\perp}}{d\Omega}$ become

$$\frac{d\sigma_R^{\parallel}}{d\Omega} = \frac{\omega_R^4}{16\pi^2\varepsilon_0 c^3}\frac{45\bar{\alpha} + 4\bar{\gamma}}{45} \tag{1-12}$$

$$\frac{d\sigma_R^{\perp}}{d\Omega} = \frac{\omega_R^4}{16\pi^2\varepsilon_0 c^3}\frac{3\bar{\gamma}}{45} \tag{1-13}$$

where $\bar{\alpha}$ and $\bar{\gamma}$ are symmetry invariants[20, 29] of the tensor $\vec{\vec{\alpha}}$, defined by their matrix representation

$$\bar{\alpha} = \frac{1}{3}\left[\alpha_{xx} + \alpha_{yy} + \alpha_{zz}\right] \tag{1-14}$$

$$\begin{aligned}\bar{\gamma} = \frac{1}{2}\Big[\left(\alpha_{xx} - \alpha_{yy}\right)^2 + \left(\alpha_{zz} - \alpha_{yy}\right)^2 + \left(\alpha_{xx} - \alpha_{zz}\right)^2\Big] \\ + 3\left[\alpha_{xy}^2 + \alpha_{xz}^2 + \alpha_{yz}^2\right]\end{aligned} \tag{1-15}$$

With equations (1-9) and (1-10), we can derive an absolute value of *differential Raman cross-section* $\frac{d\sigma_R}{d\Omega}$ by sum of $\frac{d\sigma_R^{\parallel}}{d\Omega}$ and $\frac{d\sigma_R^{\perp}}{d\Omega}$

$$\begin{aligned}\frac{d\sigma_R}{d\Omega} &= \frac{d\sigma_R^{\parallel}}{d\Omega} + \frac{d\sigma_R^{\perp}}{d\Omega} \\ &= \frac{\omega_R^4}{16\pi^2{\varepsilon_0}^2c^3} \cdot \frac{45\bar{\alpha} + 7\bar{\gamma}}{45} = \frac{\omega_R^4}{16\pi^2{\varepsilon_0}^2c^3} \cdot \tilde{\alpha}\end{aligned} \tag{1-16}$$

where $\tilde{\alpha}$ denotes an invariant scalar. The *depolarization ratio* ρ_R by taking the ratio of $\frac{d\sigma_R^{\perp}}{d\Omega}$ and $\frac{d\sigma_R^{\parallel}}{d\Omega}$ is defined as

$$\rho_R = \frac{3\bar{\gamma}}{45\bar{\alpha} + 4\bar{\gamma}} \tag{1-17}$$

One can define a *normalized Raman tensor* as $\vec{\vec{\alpha}}/\tilde{\alpha}$ according to equation (1-16). It's clear now that the differential Raman cross-section is linked to the Raman polarizability tensor. The depolarization ratio ρ_R shows how much the polarization of the Raman dipole alters from one polarization to another. Notably, the ratio ρ_R is always included in $0 \leq \rho_R \leq 3/4$. If the Raman polarizability tensor with zero trace $\bar{\alpha} = 0$, then this results in the maximum $\rho_R = 3/4$. All these definitions are useful in the following contents for surface-enhanced and tip-enahnced Raman spectroscopy (SERS, TERS).

1.2.4 Raman Tensor

Vibrational analysis

A molecule of N atoms possesses three degrees of freedom corresponding to translations and three more degrees of freedom to rotations. The rest of them is $3N - 6$ ($3N - 5$ for linear molecule) corresponding to vibrations. The vibrational modes can be studied by vibrational analysis. A given vibrational mode k belongs to one of $3N - 6$ modes, which corresponds to a vibrational pattern in a molecule with a vibrational frequency ω_k. These modes can be expressed in the *reduced mass coordinates*, which can be further transformed into the *normal coordinates* Q_k. More details about the normal coordinates are shown in Appendix A.

Raman tensor

The linear optical polarizability $\vec{\vec{\alpha}}_L$ excited by a laser of angular frequency ω_L with small perturbation can be expressed through Taylor expansion in terms of the normal coordinate $Q_k = 0$ for a vibrational mode k:

$$\overleftrightarrow{\alpha}_L(Q_k) = (\overleftrightarrow{\alpha}_L)_{Q_k=0} + Q_k\left(\frac{\partial \overleftrightarrow{\alpha}_L}{\partial Q_k}\right)_{Q_k=0} + \frac{1}{2}\cdot Q_k^2\left(\frac{\partial^2 \overleftrightarrow{\alpha}_L}{\partial Q_k^2}\right)_{Q_k=0} + \mathcal{O}(Q_k^3) \tag{1-18}$$

where $\mathcal{O}$ denotes big O notation[30, 31] corresponding to the higher order terms.

The Raman tensor $\overleftrightarrow{R}_k$ of the k mode is thus defined as

$$\overleftrightarrow{R}_k = \left(\frac{\partial \overleftrightarrow{\alpha}_L}{\partial Q_k}\right)_{Q_k=0} \tag{1-19}$$

$\overleftrightarrow{R}_k$ basically represents the change in linear polarizability $\overleftrightarrow{\alpha}_L$.

Raman polarizability and Raman tensor

The motion of a vibrational mode is written in the *k*th normal coordinate as $Q_k(t) = Q_k^0\cos(\omega_k t + \phi)$, and the Raman polarizability is denoted as $\overleftrightarrow{\alpha}_R$. Then the Raman dipole is written as $\vec{p}_R = \overleftrightarrow{\alpha}_R \cdot \vec{E} = p_R^0\cos(\omega_R t)$ where $\omega_R = \omega_L - \omega_k$ for Stokes Raman and $\omega_R = \omega_R + \omega_k$ for anti-Stokes Raman.

With consideration of a small motion Q_k in the vibrational mode, the Taylor series for $\overleftrightarrow{\alpha}_L(Q_k)$ is trimmed and described as

$$\overleftrightarrow{\alpha}_L(Q_k) = (\overleftrightarrow{\alpha}_L)_{Q_k=0} + Q_k \cdot \overleftrightarrow{R}_k \tag{1-20}$$

The dipole moment of an induced dipole can thus be written as

$$\begin{aligned}\vec{p} &= \overleftrightarrow{\alpha}_L(Q_k)\cdot\vec{E} \\ &= \left[(\overleftrightarrow{\alpha}_L)_{Q_k=0} + Q_k(t)\overleftrightarrow{R}_k\right]\cdot\vec{E}_0\cos(\omega_L t) \\ &= (\overleftrightarrow{\alpha}_L)_{Q_k=0}\cdot\vec{E}_0\cos(\omega_L t) + Q_k(t)\overleftrightarrow{R}_k\cdot\vec{E}_0\cos(\omega_L t)\end{aligned} \tag{1-21}$$

$$= (\overleftrightarrow{\alpha}_L)_{Q_k=0} \cdot \vec{E}_0 \cos(\omega_L t) + Q_k^0 \cos(\omega_k t + \phi)\, \overrightarrow{R}_k \cdot \vec{E}_0 \cos(\omega_L t)$$

$$= (\overleftrightarrow{\alpha}_L)_{Q_k=0} \cdot \vec{E}_0 \cos(\omega_L t) + Q_k^0 \overrightarrow{R}_k \cdot \vec{E}_0 [\cos(\omega_L t) \cos(\omega_k t + \phi)]$$

$$= (\overleftrightarrow{\alpha}_L)_{Q_k=0} \cdot \vec{E}_0 \cos(\omega_L t) + \frac{1}{2} Q_k^0 \overrightarrow{R}_k \cdot \vec{E}_0 \{\cos[(\omega_L - \omega_k) - \phi] + \cos[(\omega_L + \omega_k) + \phi]\}$$

$$= \vec{p}_L + \vec{p}_{aS} + \vec{p}_S$$

where $\vec{p}_L$ denotes the induced dipole for Rayleigh scattering, which oscillates at ω_L

$$\vec{p}_L = (\overleftrightarrow{\alpha}_L)_{Q_k=0} \cdot \vec{E}_0 \cos(\omega_L t) \tag{1-22}$$

and $\vec{p}_{aS}$ and $\vec{p}_S$ denote induced dipoles for anti-Stokes Raman and Stokes Raman, which oscillate at $\omega_L + \omega_k$ and $\omega_L - \omega_k$ respectively and are written as

$$\vec{p}_{aS} = \frac{Q_k^0}{2} \overrightarrow{R}_k \cdot \vec{E}_0 \cos[(\omega_L + \omega_k)t + \phi] \tag{1-23}$$

$$\vec{p}_S = \frac{Q_k^0}{2} \overrightarrow{R}_k \cdot \vec{E}_0 \cos[(\omega_L - \omega_k)t - \phi] \tag{1-24}$$

Eventually, we can relate the Raman polarizability to the Raman tensor through the phenomenological approach

$$\overleftrightarrow{\alpha}_R = \frac{Q_k^0}{2} \overrightarrow{R}_k \tag{1-25}$$

It is worth noting that $Q_k^0/2$ implies the amplitude of Raman scattering, and its intensity is thus derived $\propto (Q_k^0)^2$. If $\overleftrightarrow{\alpha}_L$ does not depend on Q_k (e.g. the highly symmetric molecule) or equivalently $\partial \overleftrightarrow{\alpha}_L / \partial Q_k = 0$, then the vibrational mode is *Raman inactive*. Likewise, if $\overleftrightarrow{\alpha}_L$ depends on Q_k ($\partial \overleftrightarrow{\alpha}_L / \partial Q_k \neq 0$), the vibrational mode is *Raman active*. This

becomes Raman selection rules. Measuring each component of the Raman tensor is impossible but the symmetry can be partly manifested by the depolarization ratio ρ_R.

1.2.5 More on Raman Scattering

The excited state in the Raman scattering process is assumed to be a virtual state. Resonance Raman scattering (RRS) takes place if the incoming photon energy coincides with the electronic transition of a molecule. The RRS intensity will be amplified for many orders. The physical origin can be found in Long's book[32].

The phenomenological approach to Raman scattering cannot explain the intensity ratio of Stokes and anti-Stokes Raman. The quantum mechanical description is required[20, 29] for the explanation. One can find more details in the books[20, 29].

1.3 Electromagnetics of Metal Surfaces

In addition to knowledge of the electronic transitions in molecules and Raman scattering, electromagnetic (EM) waves at metal surfaces play a fundamental role in surface-enhanced (SE) and tip-enhanced (TE) light-matter interactions and corresponding spectroscopy.

1.3.1 Surface Plasmon Polaritons (SPPs)

Dispersion relation

Let us consider a p-polarized (or TM[33]) electromagnetic (EM) wave (lies in the xz-plane) is incident at metal-dielectric surface $z = 0$. (There are no surface modes with s-polarization[20, 33].) Domain 1 is defined by $z > 0$ and domain 2 is defined by $z < 0$. The dispersion relation of the SPP can be derived as (see Appendix B for more details)

$$k_x = \frac{\omega}{c}\sqrt{\frac{\epsilon_1\epsilon_2}{\epsilon_1 + \epsilon_2}} \tag{1-26}$$

The $k_{z,j}$ in domains $j = 1,2$ are deduced as

$$k_{z,j}^2 = \left[\epsilon_j \left(\frac{\omega}{c}\right)^2 - k_x^2\right]^2 \text{ for } j = 1,2 \tag{1-27}$$

It's assumed that ϵ_1 is complex in domain 1 as metal $\epsilon_1 = \epsilon_1{}' + i\epsilon_1{}''$ where $|\epsilon_1{}'| \gg |\epsilon_1{}''|$ and ϵ_2 is real for the dielectric.

Quasi-Particles and Damping

Many physical systems are affected by the damping of losses, which prevents an EM wave from propagating or oscillating constantly. The amplitude of the EM wave must decay in time and (or) in space. Note that SPs are always quasi-particles except for ideal metals. The damping can be expressed from different points of view:

(1) The most common way to consider ω real, which results in complex $k = k' + ik''$. This will usher in an exponentially decaying amplitude $\propto \exp(-k''t)$. The waves with this property are called evanescent waves or modes.

(2) The alternative way is to take k real, which leads to complex $\omega = \omega' + i\omega''$. The resulting field amplitude will decay in time $\propto \exp(-\omega''t)$. These modes are called *virtual modes* (equivalent to quasi-particles). These modes appear as resonances $\omega = \omega'$ in frequency response. The width is characterized by $\omega\,''$, which corresponds to the lifetime $\tau = 1/(2\omega'')$.

Skin Depth and Propagating Length

Here, we adopt the expressions using complex k for the SPPs. Consequently, the wavenumber k_x become complex as $k_x' + ik_x''$, which is written as[34]

$$k_x' \approx \frac{\omega}{c}\sqrt{\frac{\epsilon_1{}'\epsilon_2}{\epsilon_1{}' + \epsilon_2}}$$
$$k_x'' \approx \frac{\omega}{c}\left(\frac{\epsilon_1{}'\epsilon_2}{\epsilon_1{}' + \epsilon_2}\right)^{3/2}\frac{\epsilon_1{}''}{2(\epsilon_1')^2} \tag{1-28}$$

where the k_x' and k_x'' are derived provided that $|\epsilon_1{}'| \gg |\epsilon_1{}''|$.

In z direction, fields fall to $1/e$ perpendicular to the surface and the value of skin depth as $z_{sd,j} = 1/|k_{z,j}|$ where $j = 1,2$ for domain 1,2.

$$z_{sd,1} = |k_{z,1}|^{-1} = \frac{\lambda}{2\pi}\left(\frac{\epsilon_1' + \epsilon_2}{\epsilon_2^2}\right)^{1/2}$$
$$z_{sd,2} = |k_{z,2}|^{-1} = \frac{\lambda}{2\pi}\left(\frac{\epsilon_1' + \epsilon_2}{\epsilon_1'^{\,2}}\right)^{1/2} \quad (1\text{-}29)$$

The propagating length of SPs can be defined as L_i in x direction when intensity decreases to $1/e$. Therefore, $L_i = (2k_x'')^{-1}$ according to equation (1-28), which is typically $10\sim100$ μm in the visible range and depends on the metal/dielectric configurations.

1.3.2 Localized Surface Plasmons (LSPs)

After knowing the EM properties at metal-dielectric surfaces, let us have a look at the normal modes of metal spheres at the sub-wavelength scale.

The *quasi-static approximation* provided that the particle is much smaller than the wavelength of light in the surrounding medium is applied to the following calculation. The phase of the harmonically oscillating EM field is nearly invariant over the particle volume in this case.

We consider a metal sphere of a relative permittivity $\epsilon_m(\omega)$ of radius a immersed in a dielectric medium of a relative permittivity ϵ_d with a uniform external electric field $\vec{E} = E_0\hat{z}$. By solving the Laplace equation, the potentials inside the sphere Φ_{in} and outside the sphere Φ_{out} are derived as[35]

$$\Phi_{\text{in}} = -\left(\frac{3\epsilon_d}{\epsilon(\omega) + 2\epsilon_d}\right)E_0 r\cos\theta$$
$$\Phi_{\text{out}} = -E_0 r\cos\theta + \left(\frac{\epsilon(\omega) - \epsilon_d}{\epsilon(\omega) + 2\epsilon_d}\right)E_0\frac{a^3}{r^2}\cos\theta \quad (1\text{-}30)$$

Φ_{out} can be further written as

$$\Phi_{\text{out}} = -E_0 r\cos\theta + \frac{\vec{p}\cdot\vec{r}}{4\pi\epsilon(\omega)\epsilon_d r^3} \tag{1-31}$$

where the dipole moment p

$$\vec{p} = 4\pi\epsilon(\omega)\epsilon_d a^3\left[\frac{\epsilon(\omega)-\epsilon_d}{\epsilon(\omega)+2\epsilon_d}\right]E_0\hat{z} \tag{1-32}$$

Subsequently, polarizability α can be derived from $\vec{p} = \epsilon(\omega)\epsilon_d\alpha\cdot\vec{E}$

$$\alpha = 4\pi a^3\left[\frac{\epsilon(\omega)-\epsilon_d}{\epsilon(\omega)+2\epsilon_d}\right] \tag{1-33}$$

The polarizability undergoes resonance as the denominator $|\epsilon(\omega)+2\epsilon_d|$ approaches 0. In other words, the resonance condition results in $\epsilon'(\omega) = -2\epsilon_d$ where $\epsilon(\omega) = \epsilon'(\omega) + i\epsilon''(\omega)$. This relation is known as the Fröhlich condition. This relation reveals the resonance condition for surface plasmon resonance (SPR)[33]. For larger particles beyond the quasi-static approximation, a more general form is proposed in the textbook[33].

Furthermore, within the electrostatic approximation, higher-order resonances can be obtained by the relation $\epsilon'(\omega) = -\left[\frac{(N+1)}{N}\right]\cdot\epsilon_d$ where N is an integer. For $N = 1$, the relation becomes a dipolar resonance and coincides with the Fröhlich condition. For $N > 1$, the relations represent resonances for the non-radiative higher-order multiples.

The fundamental properties of the EM waves, the SPPs, and the LSPs, unlock the potential of various applications in surface-enhanced Raman spectroscopy (SERS)[36], tip-enhanced Raman spectroscopy (TERS)[37, 38], metal-enhanced fluorescence[39], and TE fluorescence microscopy and spectroscopy [40].

1.4 Surface- and Tip-Enhanced Optical Spectroscopy and Setup

Raman scattering exhibits great chemical specificity and yields chemical or vibrational "fingerprints"[41]. However, the Raman scattering process is weak (with intrinsic differential cross-section $d\sigma/d\Omega$ on the order of $\sim 10^{-2}\ \ cm^2/sr$ [42, 43]) compared with other optical signals. SERS is a phenomenon of greatly enhanced inelastic scattering by several orders, which was discovered by molecules on the roughened surface of Ag or Au[44-47]. Its high sensitivity is applied to single-molecule (SM) detection[48, 49], which becomes SMSERS. SERS substrates are developed during these decades by fabricating Au, Ag nanoparticles (NPs), nanometer shells, nanometer gaps between NPs, and many more[50-53]. Tip-enhanced Raman spectroscopy (TERS) can achieve sub-nanometer resolution with single-molecule chemical sensitivity provided by SERS mechanism[41, 54-59]. SMSERS and TERS both provide deeper insight into the mechanisms of SERS.

1.4.1 Mechanisms of SERS

Chemical and Electromagnetic Enhancement

Mechanisms underlying SERS are revealed as multiplicative contributions of chemical enhancement (CE) and electromagnetic (EM) enhancement. The CE is presumed to emerge from two main processes: (1) enhancement from charge transfer (CT) resonances between the molecule and the SERS substrate[60]. (2) non-resonant changes in the molecular polarizability upon surface binding. The EM enhancement is universally accepted as a local EM field in the proximity of metallic sub-wavelength nanoparticle surfaces by excitation of local surface plasmon resonances (LSPRs) [61, 62].

Enhancement Factor

The most important aspect of the SERS effect is the enhancement factor (EF)[20, 41, 43, 63]. The EF is defined as the ratio as normalized SERS intensity I_{SERS} over the normal Raman intensity I_{NRS} to evaluate how much the Raman intensity is amplified. The SERS EF is expressed as[20, 43, 63, 64] (or *SERS substrate EF*[20])

$$\mathrm{EF_{SERS}} = \frac{I_{SERS}/N_{SERS}}{I_{NRS}/N_{NRS}} \tag{1-34}$$

where N_{SERS} denotes the average number of *adsorbed* molecules in the SERS scattering volume, N_{NRS} represents the average number of molecules in the non-SERS scattering volume.

The SERS effect due to the EM enhancement brings EFs ranging from $10^5 \sim 10^{10}$ in the literature [43, 62, 65, 66], while the SERS effect due to the CE yields much weaker EFs as $10 \sim 100$ [41].

The $|E|^4$-Approximation

The SERS EF from the EM enhancement is separated into two contributions[20]: (1) *local field enhancement* for the incident field and (2) *radiation enhancement* for the re-emitted field of Raman. Though we can distinguish these two EFs, these two steps occur at the same time in the Raman process.

As mentioned in the previous sections, the EM field is strongly modified in the proximity of metallic nanoparticles. The orientation and magnitude of the *local field* $\vec{E}_{loc}$ are both different at the molecule position. The spatial region with a spectacular increase of the local field amplitude $\left|\vec{E}_{loc}\right|$ compared with the incident field amplitude $\left|\vec{E}_{in}\right|$ is called the 'hot spot'[20, 36, 66-69]. This part will be further discussed in Chapter 3.

If a Raman dipole $\vec{p}_R = \alpha_R \cdot \vec{E}_{in}(\omega_0)$ (consider α_R without tensorial nature) is induced by an incident field $\vec{E}_{in}(\omega_0)$ with an angular frequency ω_0, the magnitude of the Raman dipole is enhanced by a factor $\left|\frac{\vec{E}_{loc}(\omega_0)}{\vec{E}_{in}(\omega_0)}\right|$. The corresponding radiated power is $\propto |\vec{p}_{SERS}|^2$ due to the local field, which is enhanced by a factor

$$M_{loc}(\omega_0) = \left|\frac{\vec{E}_{loc}(\omega_0)}{\vec{E}_{in}(\omega_0)}\right|^2 \tag{1-35}$$

This factor $M_{loc}(\omega_0)$ is called the *local field intensity enhancement factor*, which is associated with the excitation of the Raman dipole. Note that this factor neglects the change in polarizations of the fields.

Now we come to the second step of the process, the radiation Raman enhancement. The enhancement factor of the radiated power for the Raman emission is written as

$$M_{Rad}(\omega_R) = \left|\frac{\vec{E}_{Rad}(\omega_R)}{\vec{E}_{in}(\omega_R)}\right|^2 \tag{1-36}$$

Consequently, the overall SERS owing to the EM enhancement is a product of the local field enhancement and the radiation enhancement, which can be expressed as

$$\begin{aligned} EF_{SERS,EM} &= M_{Loc}(\omega_0) \cdot M_{Rad}(\omega_R) \\ &= \left|\frac{\vec{E}_{loc}(\omega_0)}{\vec{E}_{in}(\omega_0)}\right|^2 \cdot \left|\frac{\vec{E}_{Rad}(\omega_R)}{\vec{E}_{in}(\omega_R)}\right|^2 \approx \left|\frac{\vec{E}_{loc}(\omega_0)}{\vec{E}_{in}(\omega_0)}\right|^4 \end{aligned} \tag{1-37}$$

Note that since the Raman-shifted frequencies are close to the excitation frequency $\omega_R \approx \omega_0$, the $|E|^4$-approximation for the SERS EF can be obtained consequently. More rigorous way of the derivation for radiation enhancement had been formulated based on the optical reciprocity theorem (ORT)[70]. The $|E|^4$-approximation provides an order of estimation for EF, which is valid under a few assumptions (e.g. backward scattering configuration, an isotropic Raman tensor, the same polarization for the incoming and outgoing photons[20, 63]), which is prevalent in the calculation of the SERS EF from EM fields[20].

1.4.2 Tip-Enhanced Raman Spectroscopy (TERS)

SERS provides promising applications while it is limited to the optical diffraction limit. TERS enables one to overcome this weakness, which integrates scanning tunneling microscope (STM) into TERS as STM-TERS[56, 71] or atomic-force microscope as AFM-TERS[54-56]. Atomic resolution can be achieved by STM as the probe-sample distance is ≤

0.1 nm. This atomic resolution enables STM-TERS to benefit from the high spatial resolution. The tunneling current takes place only for conducting material while a large bias voltage requires to be supplied for semiconducting materials[72]. Single hot spots using TERS enable high-resolution imaging, such as vibrational normal modes of single porphyrin molecules imaged[73] and other independent TERS images with high spatial resolution[73]. Tip-sample distance is maintained by setting a threshold of force as the tip moves to the proximity of the surface. The advantage of AFM is the versatility of samples, which means insulating material can also be imaged with nanometer resolution. A metal-coated tip can make the tip greatly enhance the optical signals[74], which is also demonstrated to optimize the signals by with variable thickness[75]. Tip-sample distance maintained by shear-force scheme[76-79] is also one of the AFM-TERS techniques. Instead of the tip of the cantilever as a probe, an apertureless probe of Au or Ag is mounted on a quartz tuning fork. The low cost of quartz tuning forks is widely used in our modern life, which also makes the AFM technique by shear-force feedback affordable and extendable[80]. With these benefits in mind, the shear-force method is used to carry out tip-enhanced (TE) optical measurements. This work regarding optical resolution will be continued in Chapter 4.

1.4.3 Experimental Setup for TERS

Confocal Microscope with the Parabolic Mirror

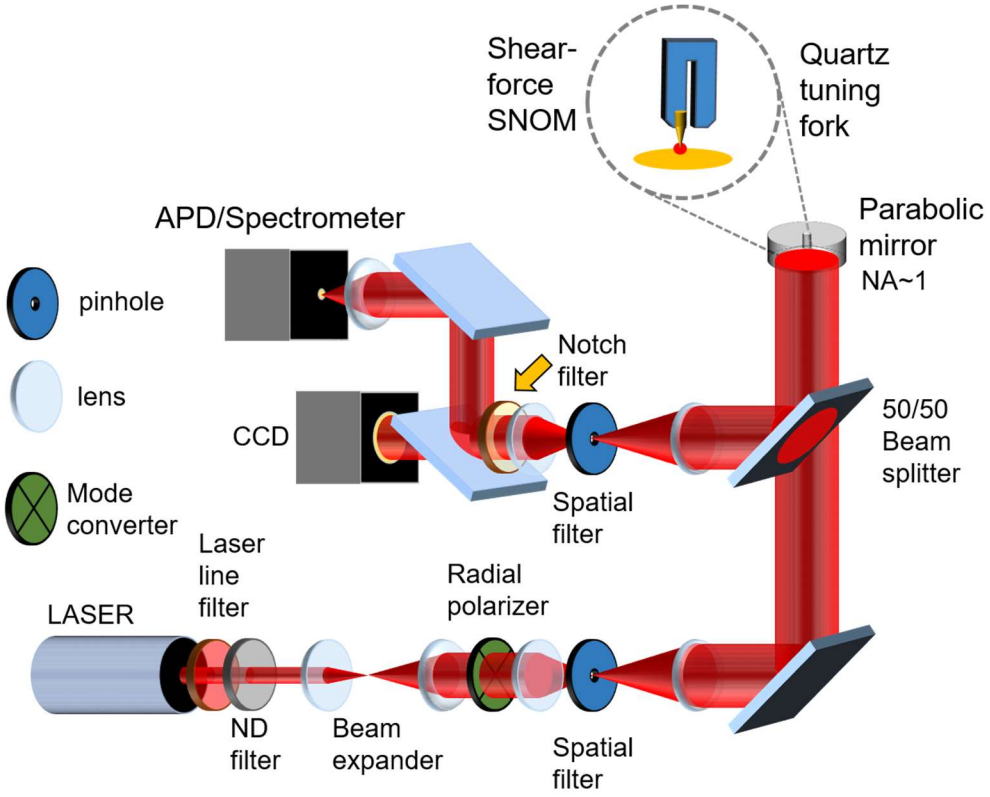

Figure 1.3 Schematic of the optical microscope setup using the parabolic mirror (PM) of a geometrical $NA{\sim}0.998$ in air.

An overview of the home-built optical microscope setup implemented with SPM is employed for the confocal and TE optical measurements as shown in Figures 1.3 and 1.4. For the optical microscope, a CW 532-nm laser (QIOPTIQ, NANO 250-532 max) and a 636-nm diode laser (Picoquant, PDL 800-D) operated in the CW mode are integrated into the microscope and are switchable for excitation in optical spectroscopy. (Only the 636 nm laser is plotted in Figure 1.3) The laser beam filtered by a laser line filter is expanded through two telescopes to overfill the back aperture of a parabolic mirror (PM). The laser beam can be converted from the linearly polarized beam into a radially polarized doughnut mode (RPDM) by a mode converter (MC)[81] or a radial polarizer. A beam splitter plate (BS) is used for separation excitation source and emission.

Illumination using the high numerical aperture ($NA{\sim}0.998$) PM in the ambient provides high optical resolution and lays the ground for ambient tip-enhanced optical measurements.[82-85] Optical emission transmits two optical notch filters (central wavelength 633 nm, StopLine® single-notch filter) and is detected by a charge coupling device (CCD) camera (placed after the telescope). The position of the CCD is set to coincide with the back-focal plane (BFP), which can collect emission or elastic scattering patterns. The BFP imaging technique will be further described in Chapter 5. An avalanche photodiode (APD, Single Photon Counting Module SPCM AQR 14; Perkin Elmer) is used for the detection of all photons except for the laser, which enables one to carry out fast optical imaging. Another CCD is coupled to a spectrometer (Acton Research, SpectraPro 300i), which is used to collect dispersed photons as optical emission spectra. These two CCDs are both cooled by liquid Nitrogen (LN_2) for normal operations with minimal background signals.

Shear-Force Scanning Probe Microscope

Figure 1.4 (a) and (b) show the shear-force SPM setup and the connections of electronic devices. An electrochemically etched[86] Au tip rigidly mounted to a quartz tuning fork (QTF) is used to collect topography synchronously with the optical signal. The Au tip approaches the optical focal field through an opening of the PM from the top. The position of the Au tip is moved in 3D by shear piezoelectric stacks until the tip coincides with the focus with minimal elastic scatterings. Moreover, the corresponding PL patterns of the tip can be obtained as it is scanned through the focus for fine adjustments.

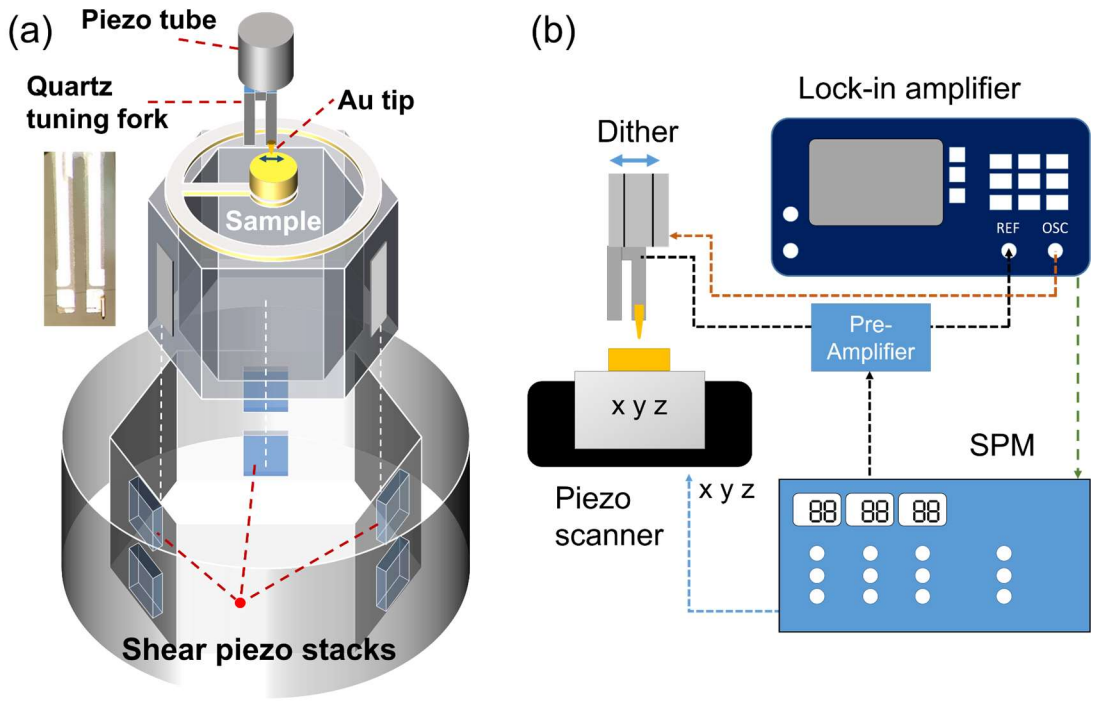

Figure 1.4 (a) A 3D drawing of scanning probe microscope (SPM) in the shear-force scheme. Piezo tube is used for scanning the Au tip in x-, y-direction. The sample holder is integrated with shear piezoelectric stacks for driving the sample to move towards the Au tip parallel to the optical axis. The sample holder stands on a 3-axis piezo scanner for realizing feedback control from the SPM controller. An inset is a bright-field image of a quartz tuning fork with Au tip rigidly mounted. (b) Connections of the shear-force SPM, which consist of an SPM controller, a lock-in amplifier, and a pre-amplifier.

The QTF is dithered in a motion parallel to the surface by the piezo tube and oscillates at its resonance frequency ($\omega_0 = 2^{15}$Hz $\cong$ 32 kHz). As shown in the inset of Figure 1.4 (a), the Au tip is glued rigidly to one prone of the QTF. The quality factor (Q factor) of the QTF is normally on the order of $10^2 \sim 10^3$ while the tip is disengaged. As the sample is moved towards the proximity of the tip, friction force and viscous force[87] are assumed to influence the resonant oscillations of QTF. The amplitude of QTF will drop, the resonance frequency ω_0 will be shifted and the phase will drop (a phase shift occurs)[5, 87-90]. The extremely weak phase shift signals can be pre-amplified and be demodulated by a lock-in amplifier (Ametek 7270 DSP) as feedback signals[89, 91].

The tip-sample distance is regulated by an SPM controller (RHK SPM100) according to the phase shift. The phase shift is related to the tip-sample distance, which can

be tuned by the set point in the SPM controller, where the set point corresponds to a user-defined threshold voltage. The SPM controller will stop increasing voltage to the piezoelectric scanner (P-517.3CL, Physik Instrument) on the z-axis once the feedback signals reach the threshold values.

Simultaneous tip-enhanced optical and topographic images can be obtained by raster scanning the sample. Electronic handshaking of the SPM controller can be set to communicate with the spectrometer, which enables one to carry out 1D or 2D spectral mappings.

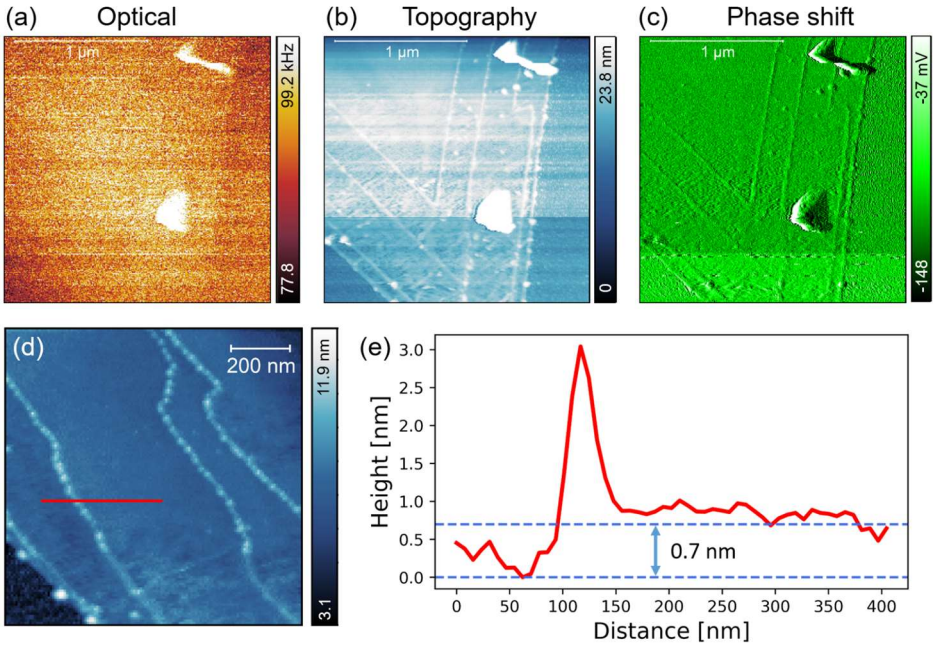

Figure 1.5 Tip-enhanced (TE) optical measurements of WS_2. Simultaneous acquisition of (a) TE optical image (b) topographic image and (c) phase shift can be obtained. (d) A smaller area of the topography of WS_2 (e) A 1D section profile of topography corresponds to the red line in (d), which shows the thickness of single-layer ~0.7 nm.

Figure 1.5 (a) and (b) show an example of tip-enhanced optical measurements using WS_2, which shows results by simultaneous acquisition of tip-enhanced optical image and topographic image in a scan range of 2 µm × 2 µm. Scan movements in x, y are performed by a piezoelectric scanner of 2-secs scan line time for the security of the Au tip. The piezo scanner receives signals from the SPM controller and keeps the tip-sample distance a constant by moving 3-axis piezoelectric scanner in the z-axis. Phase shift signals are

recorded during each scan as well for monitoring feedback during each scan as shown in Figure 1.5 (c). This helps one to avoid artifacts of measurements.

The calibrated z-axis piezoelectric movement in response to the voltages from the SPM controller can be done with well-known samples (e.g. Highly Ordered Pyrolytic Graphite, a grating, 2D materials, etc.). WS_2 serves as a standard sample for z-axis calibration here due to its thickness of $\sim 0.7\ nm$. This value can be measured by a calibrated AFM. The uncalibrated value of the height (nm) per unit Volt h/V is assumed to be $h_0\ (nm/V)$. This provides a measured thickness of $\delta_0 \cdot 0.7\ nm$ with a factor $\delta_0 \neq 1$. This needs to be compared with the measured thickness by well-calibrated AFM. The calibrated value for h/V can be determined as h_0/δ_0. This calibration step is crucial to all the following topographic measurements.

In addition, with proper cable connections and calibration of the SPM controller, approach curves can be obtained by continuous sample movement driven by the piezoelectric scanner in the z-axis with a ~300-nm maximum scan range. The approach curves of distance-dependent optical signals with quantified moving range can be obtained.

1.5 Focal Field Distributions of the Higher-Order Laser Modes

The point spread function (PSF)[5] is the optical response due to a perfect point object, which is also a measure of optical resolution in an optical microscope. Image formation is a convolution of object and excitation PSF. If a pinhole is placed in the detection for blocking out-of-focus light in the confocal microscope, then the total effective PSF is a product of excitation PSF and detection PSF[5]. Therefore, the comprehension of excitation sources is a fundamental element in confocal microscopy. Furthermore, the near-field enhancement of nanoparticles can be further amplified by the higher-order laser modes.

1.5.1 Higher-Order Laser Modes

As described in the previous section, the higher-order laser modes (or cylindrical-vector beams[92]) as radially polarized doughnut mode (RPDM) and azimuthally polarized

doughnut mode (APDM) for excitation sources are important in the determination of molecular dipole orientation[93] in optical microscopy and spectroscopy. Richards and Wolf had completed the basic mechanisms used to analyze focused polarized beams[94]. Expressing the optical fields in cylindrical coordinate (ρ, ϕ, z), the RPDM is formulated as[92]:

$$E_\rho(\rho, z) = A \int_0^\alpha (\cos\theta)^{1/2} f_0(\theta) \sin 2\theta \, J_1(k\rho \sin\theta) \, e^{ikz\cos\theta} d\theta \qquad (1\text{-}38)$$

$$E_z(\rho, z) = 2iA \int_0^\alpha (\cos\theta)^{1/2} f_0(\theta) (\sin\theta)^2 \, J_0(k\rho \sin\theta) e^{ikz\cos\theta} d\theta \qquad (1\text{-}39)$$

where the pre-factor A is the amplitude, α is the maximum incident angle, $J_n(x)$ is the Bessel function of the first kind of nth order, and $f_0(\theta)$ is an *apodization function* and defined as $f_0(\theta) = \exp\left[-\frac{1}{{f_c}^2}\frac{\sin\theta}{\sin\theta_{max}}\right]$ with filling factor $f_c = 1$ in our case since the back aperture of the PM is overfilled in the measurements.

The APDM is expressed as

$$E_\phi(\rho, z) = 2A \int_0^\alpha (\cos\theta)^{1/2} f_0(\theta) \sin\theta \, J_1(k\rho \sin\theta) \, e^{ikz\cos\theta} d\theta \qquad (1\text{-}40)$$

where A denotes amplitude. This formula shows non-zero transverse component E_ϕ and zero longitudinal component E_z for the azimuthal polarization.

Let us consider the parameters in our PM configuration with NA ~ 0.998 and medium at focus is air (refractive index as 1), and calculate the corresponding field distributions as shown in Figure 1.6. The peak field intensity of the longitudinal component $|E_z|^2$ is almost 10 times more intense than that of the transverse component $\left|E_{xy}\right|^2 = |E_x|^2 + \left|E_y\right|^2$ in the RPDM.

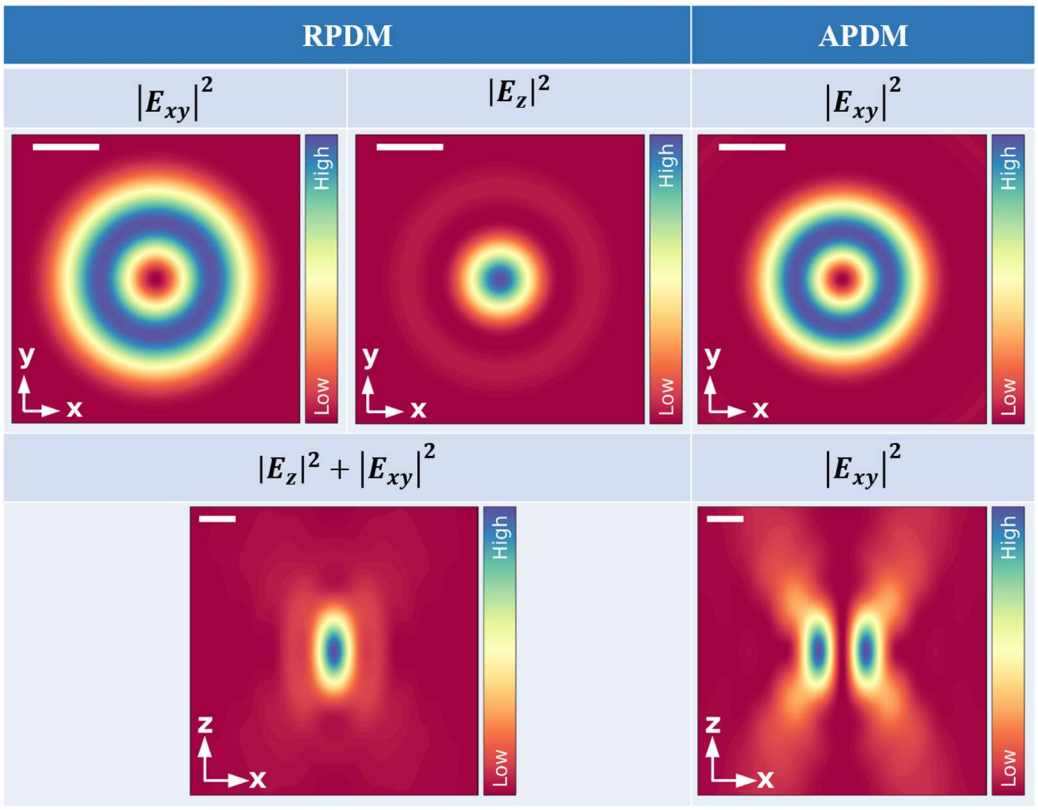

Figure 1.6 Field intensity distributions of the RPDM and the APDM in the air of incident wavelength $\lambda = 633\ nm$ and $NA = 0.998$. The scale bar inserted in each panel is $\lambda/2$. The in-plane or transverse distribution $|E_{xy}|^2 = |E_x|^2 + |E_y|^2$ and the out-of-plane or longitudinal distribution $|E_z|^2$ are calculated in the xy-plane and the xz-plane as indicated in each panel.

1.5.2 Field Enhancement with Higher-Order Laser Modes

The PL intensity of a molecule with an absorption dipole moment $\vec{\mu}$ excited by an electric field $\vec{E}$ is $\propto |\vec{\mu} \cdot \vec{E}|^2$. The direction of the dipole moment can be determined by symmetries of the molecule in the context of the Born-Oppenheimer approximations[95, 96]. If we take field enhancement into account, the excitation enhancement is $\gamma_{ex} = |\vec{\mu} \cdot \vec{E}|^2 / |\vec{\mu} \cdot \vec{E}_0|^2$ with incident electric field $\vec{E}_0$. The overall enhancement[97, 98] of PL is a product of excitation enhancement and emission enhancement, which is $\gamma_{ex}\eta_{PL} = \gamma_{ex}(\gamma_{rad}/\gamma_{tot})$ where η_{PL} denotes the quantum yield of the molecule.

Therefore, we can infer that γ_{ex} will be optimal if $\vec{\mu}$ is parallel to $\vec{E}_0$. For instance, the APDM will make optical signals from 2D materials (e.g. MoS_2, WS_2) optimal. The plasmonic nano-structures with out-of-plane geometries, Au nanocones[99] can be properly excited with the RPDM. Orientations of sub-wavelength single nanoparticles can be imaged by using these higher-order laser modes[100]. It's demonstrated by FDTD calculations that the field enhancement of the tip through excitation of the RPDM is much stronger than p-polarized light excitation[101]. Hence, in our tip-enhanced (TE) optical measurements, the RDPM or the radial polarization is applied to excite the metallic tip[102] and produce better coupling efficiency of the tip-sample configuration. More applications for these modes can be found in the review[93].

1.6 Dipole Radiation

The overall light-matter interaction includes excitation and emission processes. The optical radiation properties of antennas[103-106] are of great interest in nano-optics as well. In electrodynamics, oscillating charges or currents can generate electromagnetic waves. The current source distribution is localized in a small region, whose radiation can travel a long distance from the source. Here, we elaborate on the physics of the Hertz dipole[107-109] for a better understanding of radiation. The crucial physical properties of dipole fields are presented here, and the derivation of the Hertz dipole field can be found in Appendix C. A variety of measures for characterizing antennas will be introduced in this section as well. Many details and various types of antennas are described in the text books[35, 110, 111].

1.6.1 The Hertz Dipole

A Hertz dipole is composed of a pair of opposite charges $\pm q$ separated by an infinitesimally small distance l as shown in Figure 1.6. The dipole moment with time-harmonic dependence can be expressed as $\vec{p}(t) = \hat{z}\, p_0 \cdot \cos \omega t$, which is located along the z-axis with angular frequency ω and strength of dipole moment $p_0 = ql$.

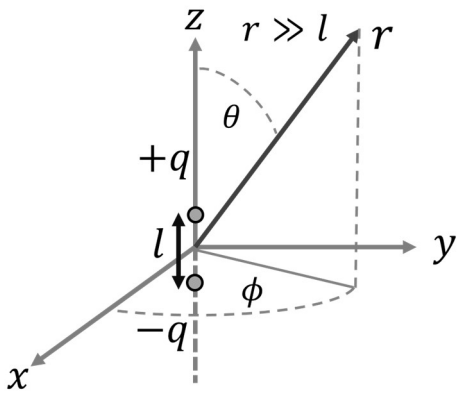

Figure 1.6 Schematic of the Hertz dipole with an infinitesimal separation l observed at r in the spherical coordinates (r, ϕ, θ)

The explicit expressions of non-zero field components without time-harmonic dependence in spherical coordinates at the point $\vec{r}$:

$$\vec{H} = \hat{\phi}\,\frac{p_0 \omega e^{ikr}}{4\pi r}\sin\theta\left(k + \frac{i}{r}\right) \tag{1-43}$$

$$\begin{aligned}\vec{E} = \hat{r}\,\frac{p_0 \cdot e^{ikr}}{4\pi\varepsilon}2\cos\theta\left(\frac{ik}{r^2} - \frac{1}{r^3}\right) \\ + \hat{\theta}\,\frac{p_0 \cdot e^{ikr}}{4\pi\varepsilon}\sin\theta\left(\frac{k^2}{r} + \frac{ik}{r^2} - \frac{1}{r^3}\right)\end{aligned} \tag{1-44}$$

where $\vec{k}$ is the wave-vector and its magnitude k is the wave-number, ε_0 is the permittivity in the vacuum.

From equations (1-43), (1-44), among these field components, it can be observed that only $\vec{E}_{ff}(\vec{r})$ and $\vec{H}_{ff}(\vec{r})$ with r^{-1} dependence exists for the far-field range (or radiation zone[35]) under condition $l \ll \lambda \ll r$ [33, 35]. The subscript ff denotes 'far-field'. These far-field components can be expressed as

$$\vec{E}_{ff}(r) = \hat{\theta}\,\frac{p_0 k^2}{4\pi\varepsilon r}e^{ikr}\sin\theta \tag{1-45}$$

$$\vec{H}_{ff}(r) = \hat{\phi}\,\frac{k\omega p_0}{4\pi r}e^{ikr}\sin\theta \tag{1-46}$$

Other field components are attributed to near-field. They fall faster than $1/r$ and are ignored in the far-field radiation fields. From equations (1-45) and (1-46), electric and magnetic fields are perpendicular to each other. Their amplitudes can be related by $Z_0 = \left(\frac{\mu_0}{\epsilon_0}\right)^{1/2} \cong 377\ \Omega$, which is the impedance of free space.

The energy flows radially from the current source can be quantified by the Poynting vector $\vec{S}$ with the dimension of energy per unit time per unit area. The Poynting vector and electromagnetic fields are related as[35] $\vec{S} = \vec{E} \times \vec{H}$. In the far-field radiation of the Hertz dipole, the electric and magnetic fields are stated in equation (1-44). The corresponding Poynting vector with time-harmonic dependence can be expressed as

$$\vec{S} = \vec{E} \times \vec{H} = \hat{r}Z_0\left(\frac{\omega kp}{4\pi r}\right)^2 \sin^2\theta\cos^2(kr - \omega t) \tag{1-47}$$

from which it can be seen that $\vec{S}$ points in the $\hat{r}$ direction and perpendicular to electric and magnetic fields.

The time-averaged Poynting vector $\langle\vec{S}\rangle_T$ becomes

$$\langle\vec{S}\rangle_T = \frac{1}{2\pi}\int_0^{2\pi} d(\omega t)\vec{E} \times \vec{H} = \hat{r}\,\frac{Z_0}{2}\left(\frac{\omega kp}{4\pi r}\right)^2 \sin^2\theta \tag{1-48}$$

This integral only brings $\cos^2(kr - \omega t)$ into $1/2$ in equation (1-48) and $\langle\vec{S}\rangle_T$ shows $\sin^2\theta$ angular dependence and ϕ-independence. This will be further described with some quantitative parameters in the following section.

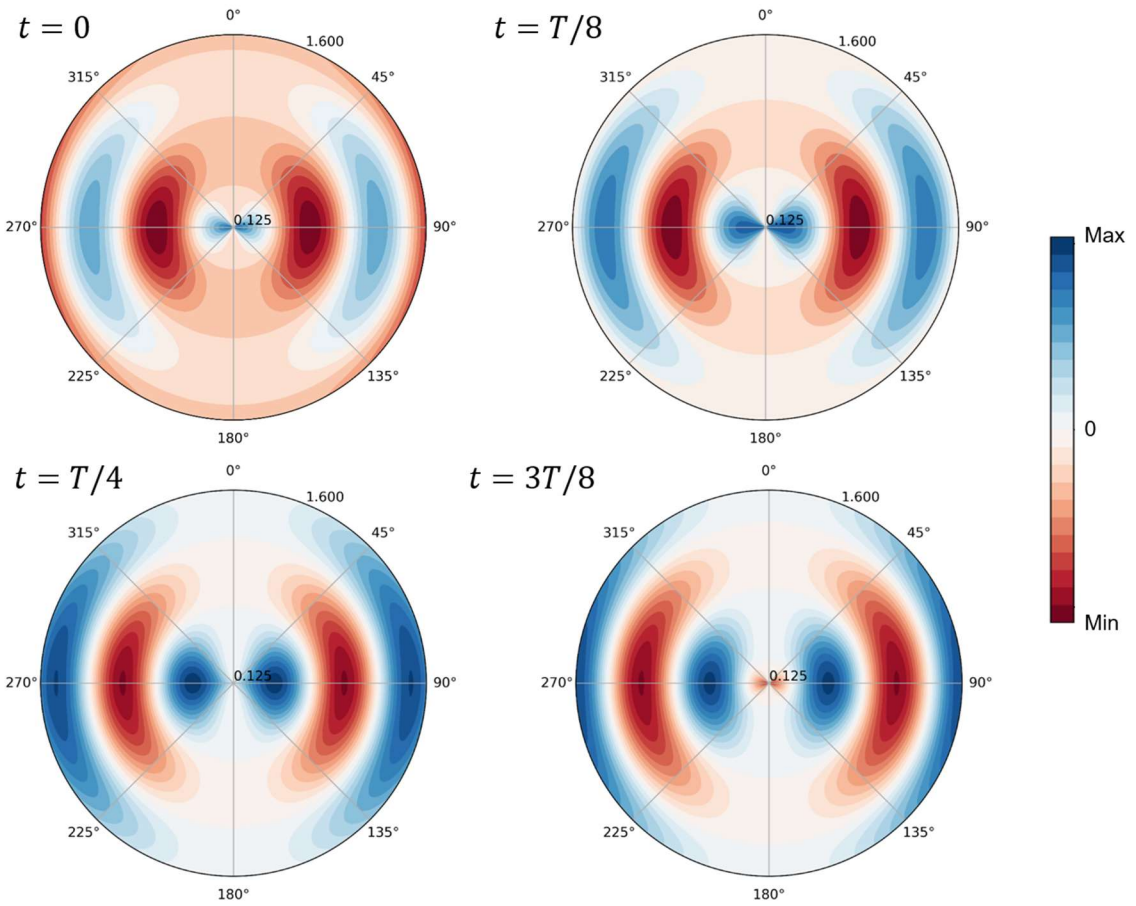

Figure 1.6 Electric field patterns with field lines of an oscillating dipole at successive time instant $t = 0, \frac{T}{8}, \frac{T}{4}, \frac{3T}{8}$.

To visualize the oscillating field patterns of the Hertz dipole, electric fields and field lines are tangential to each other. In other words, a small displacement as $d\vec{r}$ tangent to an electric field $\vec{E}$ such that $d\vec{r} \times \vec{E} = 0$. The electric field lines of the Hertz dipole can be obtained, whose details can be found in the textbook[110].

The corresponding electric field patterns of the oscillating dipole at consecutive time constants from $t = T\ /\ 8$ to $t = 3T/8$ are depicted in Figure 1.6. The parameter T is the period of the wave, which is $T = 2\pi/\omega$. The radial values are the spatial regions in units of wavelength λ. The radiation dynamics of the Hertz dipole in free space as time evolves are visualized.

1.6.2 Directivity, Gain and Beamwidth

Antennas are built for transmitting and receiving electromagnetic waves. To quantify the propagation of the radiated electromagnetic waves by some measures is important.

Let us consider an antenna with radiated power P. A differential power dP intercepting an element area $dA = r^2 d\Omega$ of a differential solid angle $d\Omega$. Then the power per unit area is defined, or the *power density* of the radiation as

$$\frac{dP}{dA} = \frac{dP}{r^2 d\Omega} = P_r \tag{1-49}$$

The *radiation intensity* $U(\theta, \phi)$ is defined as the power per unit solid angle.

$$U(\theta, \phi) = \frac{dP}{d\Omega} = r^2 P_r \tag{1-50}$$

The *total power* radiated over the full solid angle can be expressed as

$$P_{tot} = \int \frac{dP}{d\Omega} d\Omega = \int_0^{\pi} \int_0^{2\pi} U(\theta, \phi) \sin\theta \, d\theta d\phi \tag{1-51}$$

Note that a special case of an isotropic radiator which radiates energy uniformly in all solid angles as the *isotropic radiation intensity* is $U_I = dP/d\Omega = P_{tot}/4\pi$

The *directive gain* of an antenna system towards a certain direction is defined as radiation intensity divided by the isotropic intensity

$$D(\theta, \phi) = \frac{U(\theta, \phi)}{U_I} = \frac{4\pi}{P_{tot}} U(\theta, \phi) = \frac{4\pi}{P_{tot}} \frac{dP}{d\Omega} \tag{1-52}$$

The maximum values of directive gain are defined as directivity, D_{max}. The radiation intensity will be maximum at (θ_0, ϕ_0) such that $D_{max} = \frac{U_{max}}{U_I}$. D_{max} is commonly expressed in decibel (dB) as $D_{dB} = 10\log_{10}\left(\frac{D_{max}}{D_I}\right)$ by comparing with the directivity of an *isotropic radiator*. We can further express $D_{dB} = 10\log_{10}(D_{max})$ with $D_I = 1$.

We can have radiation intensity again by writing

$$\frac{dP}{d\Omega} = \frac{P_{tot}}{4\pi} D(\theta, \phi) \tag{1-53}$$

and power density in the direction of (θ, ϕ)

$$\frac{dP}{dA} = \frac{dP}{r^2 d\Omega} = \frac{P_{tot}}{4\pi r^2} D(\theta, \phi) \tag{1-54}$$

Now we see their relation to directive gain. $P_{tot}D(\theta, \phi)$ is defined accordingly as effective isotropic power. Another concept is *power gain* or *gain* of an antenna, which is defined as

$$G(\theta, \phi) = \frac{U(\theta, \phi)}{P_{\mathrm{T}}/4\pi} = \frac{4\pi}{P_T}\frac{dP}{d\Omega} \tag{1-55}$$

where P_T is the power delivered to the terminals. The efficiency factor ζ of the antenna is defined

$$\zeta = \frac{P_T}{P_{tot}} \rightarrow P_T = \zeta P_{tot} \tag{1-56}$$

with this relation and G and D are related as

$$G(\theta,\phi) = \zeta D(\theta,\phi) \tag{1-57}$$

Eventually, we have the angular distributions $G(\theta,\phi)$, $D(\theta,\phi)$ and $U(\theta,\phi)$, which are proportional to one another. In addition, describing the angular distribution of radiation is easier to define normalized gain by

$$g(\theta,\phi) = G(\theta,\phi)/G_{max} \tag{1-58}$$

1.6.3 Dipole of Various Lengths

After knowing these fundamental parameters for the characterization of antennas, we further step into radiation patterns of dipole antennas of various lengths L.

The normalized gain $g(\theta,\phi)$ of a linear antenna with a separation L with harmonic current distribution, which is expressed as[110, 112]

$$g(\theta,\phi) = c_n \left| \frac{\cos[kL\cos(\theta)/2] - \cos(kL/2)}{\sin(\theta)} \right|^2 \tag{1-57}$$

where c_n denotes a normalization constant such that the maximum of $g(\theta,\phi)$ is equivalent to unity. The 3D radiation patterns of a variety of dipoles of different lengths L according to equation (1-57) are calculated and shown in Figure 1.7 (a)-(f). It can be seen that the radiation patterns of the antennas are different as the L varies. Quantitatively, the corresponding directivities D_{dB} are indicated in each plot. The dipole antenna of $L = 1.25\ \lambda$ shows the highest directivity.

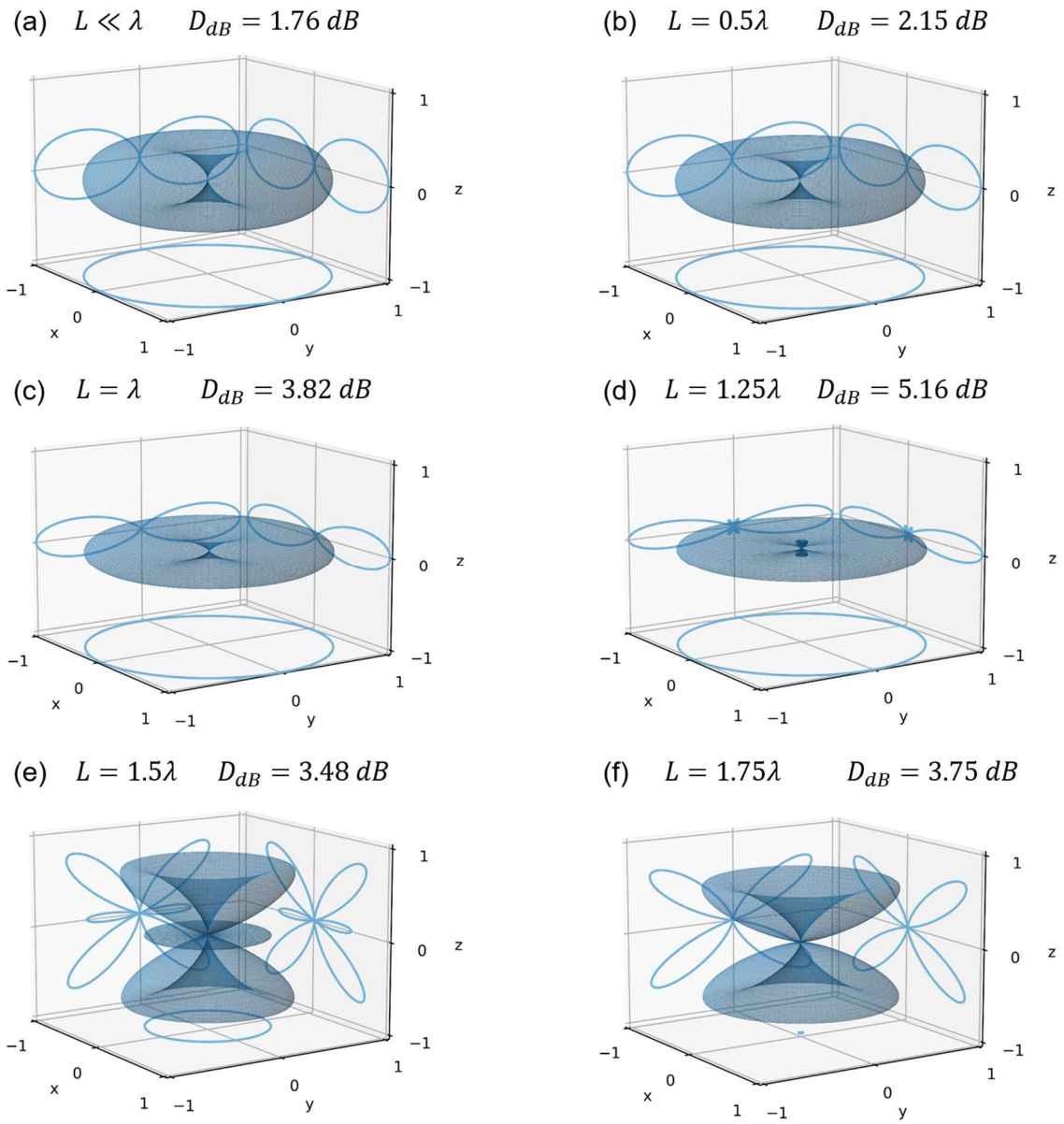

Figure 1.7 3D radiation patterns of the dipole antenna of length L and directivities. (a) $L \ll \lambda$ (b) $L = 0.5\lambda$ (c) $L = \lambda$ (d) $L = 1.25\lambda$ (e) $L = 1.5\lambda$ (f) $L = 1.75\lambda$

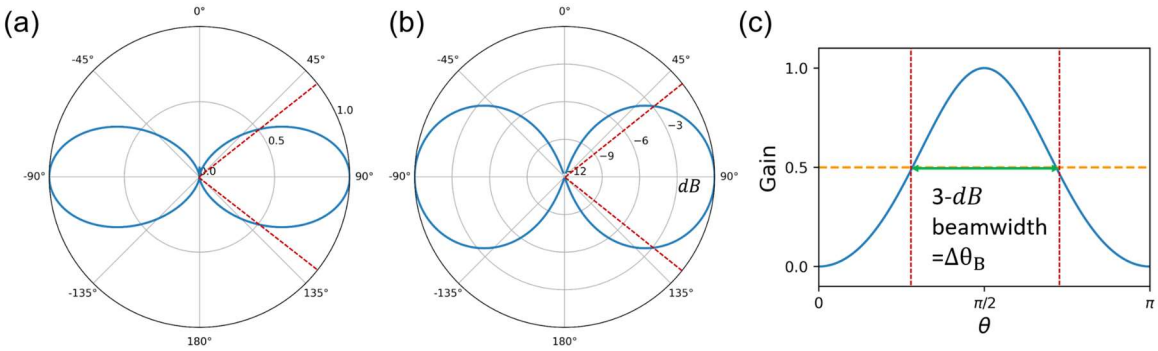

Figure 1.8 The gain of the half-lambda or half-wave antenna ($L = 0.5 \cdot \lambda$), which is plotted in (a) polar coordinates and (c) regular coordinates. The gain in the dB scale is shown in (b).

As an example, let us consider the gain of a half-lambda antenna $g(\theta) = \cos\left(\frac{\pi}{2}\cos\theta\right)^2 / \sin\theta^2$. We can evaluate the *half-power beamwidth* (HPBW) or the *beamwidth* $\Delta\theta_{HPBW}$ as the half of gain as shown in Figure 1.8 (a). The beamwidth $\Delta\theta_{HPBW}$ of the normalized intensity drops to 0.5, which corresponds to $-3\ dB$ (see Figure 1.8 (b)). The half-power circle intersects the gain at an angle of $\Delta\theta_{HPBW} = 78.08°$, which is smaller than the beamwidth of the Hertz dipole. The gain in the regular scale is shown in Figure 1.8 (c) for clear understanding. This parameter helps us evaluate how directional the radiation of an antenna is.

These definitions in radiation properties of antennas are fundamental and crucial to our experimental data analysis.

1.7 Numerical Simulations in Electrodynamics

With electromagnetic theory based upon the Maxwell equations[35], one can solve basic problems of special geometries. Mie theory[113] or Generalized Mie theory[114, 115] demonstrated the analytic solutions of the metallic spheres. The EM problem of two-cylinders of variable diameter or gap sizes can be elegantly solved by transformation optics[116]. Coupling between a metallic single nanosphere (and dimer) and a single emitter had been also formulated analytically [117, 118].

However, the geometries of objects at the nanometer scale are usually too complicated to be solved analytically. Computational physics tools such as *Finite-Difference Time-Domain (FDTD)*[119], *Finite Element Method (FEM)*[120, 121] are widely used for solving EM problems in the nano-optics field. Furthermore, the FDTD simulation can implement a different form of sources, for instance, linearly and radially polarized beam[101]. The electrostatic approximation enables one to reduce the complexity of the EM problems but also neglects the effect of retardation[122]. The effect of retardation will not be neglected in FDTD simulations[123]. The multipolar contribution to excitation enhancement is calculated by FDTD simulations[98]. Here, we perform electrodynamics simulations in the FDTD scheme for the interpretation of experimental results throughout the dissertation.

1.7.1 FDTD simulations using Meep

Let us consider the time-dependent evolution of Maxwell equations, FDTD is a straightforward way of numerically solving partial differential equations (PDE) of electrodynamics problems by discretizing time-dependent Maxwell equations into Yee lattice[124]. In addition, several open-source and commercial softwares implement the method. Meep is a free, open-source FDTD computational solver[125], which fulfills the research purposes with multifarious features such as a variety of boundary conditions, distributed-memory parallelism, flexible output electromagnetic fields as images and movies. Meep is developed in the C++ programming language for efficient calculations. The python interface of Meep is also supported and makes simulations straightforward to use.

In general, a couple of settings are required for an FDTD simulation as follows

(1) A time-dependent source (or sources), e.g. CW or Gaussian, etc. of amplitude distributions, e.g. plane wave or Gaussian envelope, etc.

(2) Simulation cell and the corresponding coordinate system (e.g. Cartesian or cylindrical coordinate systems)

(3) A geometry (or geometries) of materials with the well-known dielectric responses $\epsilon(\omega)$ (user-defined relative permittivity is available)

(4) Boundary conditions (perfectly matched layers, PMLs, or absorber layers)

The simulation environment can be visualized for confirmation before time-stepping routines. Monitors are required for some physical properties, for instance, scattering, absorption, etc. In the end, time-steps with different conditions and output formats need to be defined by a user.

1.7.2 Resonant Modes by FDTD

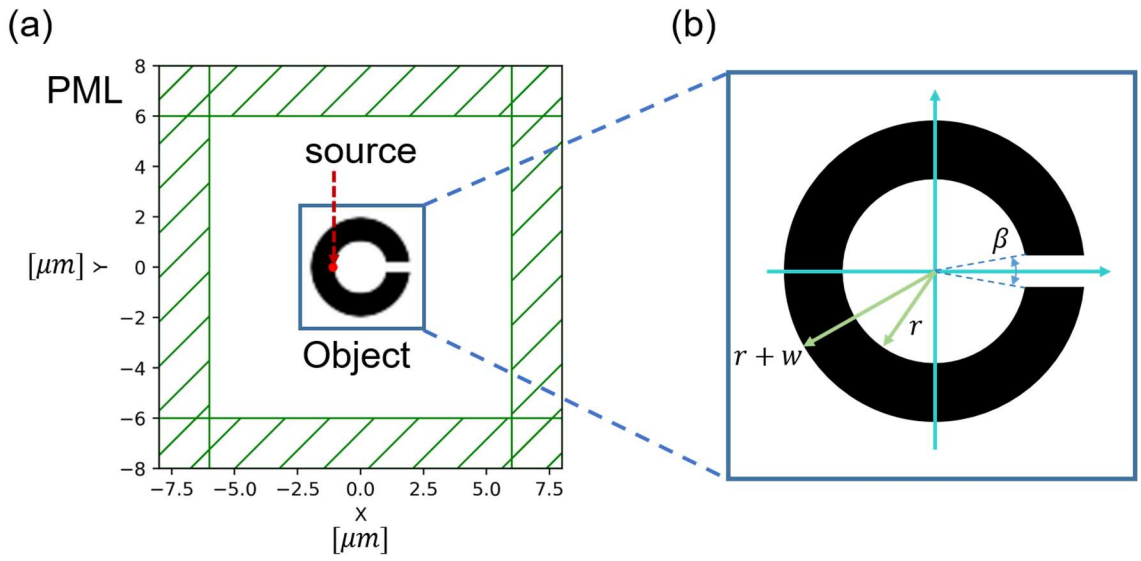

Figure 1.9 Resonant modes calculation by FDTD (a) FDTD simulation environment consists of single source (or sources) objects and PMLs. (b) Detailed schematic of a dielectric split-ring resonator (SRR) with opening angle $\beta = 20°$.

For a clear view of the above settings, a simulation case is shown as an example in Figure 1.9. Here, a point source, PMLs, and an object as the elements of an FDTD simulation are shown in Figure 1.9 (a). The geometry of the dielectric split-ring resonator (SRR) is shown in Figure 1.9 (b), whose resonant modes cannot be solved analytically. The parameters of the SRR are $r = 1\ \mu m$ and $w = 1\ \mu m$, whose refractive index is set to be $n_{SRR} = 3.4$. The thickness of the PMLs is $2\ \mu m$ in x and y directions. The point source is located at $(x, y) = (-(r + 0.1)\ ,0)$. With FDTD simulations, numerical solutions of the structure can be obtained.

Table 1.1 Resonant modes in the dielectric SRR

Mode	Frequency	Decay	Q
	$Re(\omega_n)$	$-Im(\omega_n)$	$-Re(\omega_n)/Im(\omega_n)$
$n = 1$	$1.21 \cdot 10^{-1}$	$-1.00 \cdot 10^{-3}$	$6.08 \cdot 10^{1}$
$n = 2$	$1.51 \cdot 10^{-1}$	$-4.00 \cdot 10^{-4}$	$1.89 \cdot 10^{2}$
$n = 3$	$1.80 \cdot 10^{-1}$	$-2.44 \cdot 10^{-4}$	$3.70 \cdot 10^{2}$

Meep provides resonant modes calculations, which calculates $f_{res}(t) = \sum_n a_n e^{-i\omega_n t}$. Table 1.1 shows the results of calculations for resonant modes, which lists the modes' *frequencies* $Re(\omega_n)$, *decay rates* and Q. These parameters correspond to $Re(\omega_n), -Im(\omega_n)$ and $-Re(\omega_n)/Im(\omega_n)$ respectively. The eigenfrequencies ω_n are given in Meep units[125] of $2\pi c$. Q is a dimensionless parameter and defined by $Q = -Re(\omega_n)/Im(\omega_n)$ where Re indicates the real part and Im indicates the imaginary part. According to the results, one can calculate the field patterns of the resonant modes by implementing the eigenfrequencies ω_n in the FDTD simulations. Meep also provides complex amplitudes a_n and errors of each resonant mode, which are not shown here.

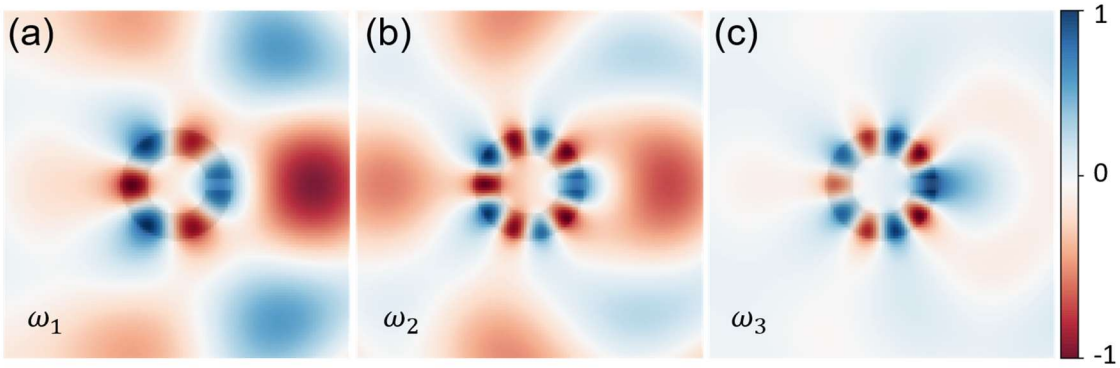

Figure 1.10 Field patterns of the corresponding resonant modes ω_n ($n = 1$~3) are shown in (a)-(c). The absolute values of the field amplitude are normalized to 1.

After time-stepping routines in FDTD simulations, field patterns of ω_n can be calculated and shown in Figure 1.10. The field intensity in the SRR is comparable to free

space in the resonant mode of $n = 1$. In contrast, the field intensity in the SRR is more concentrated in the SRR for the resonant mode of $n = 3$. These results can only be obtained by numerical calculations. The FDTD simulations here provide a clear and quantified solution to the EM problem.

1.7.3 Differential Scattering by FDTD

The far-field radiation patterns can be derived by the dyadic Green function[126] from the near-field distributions. Alternatively, the function of the *near-to-far* transform is implemented in FDTD softwares in numerous publications. Here, far-field scatterings of a Au sphere are demonstrated by the Meep FDTD solver.

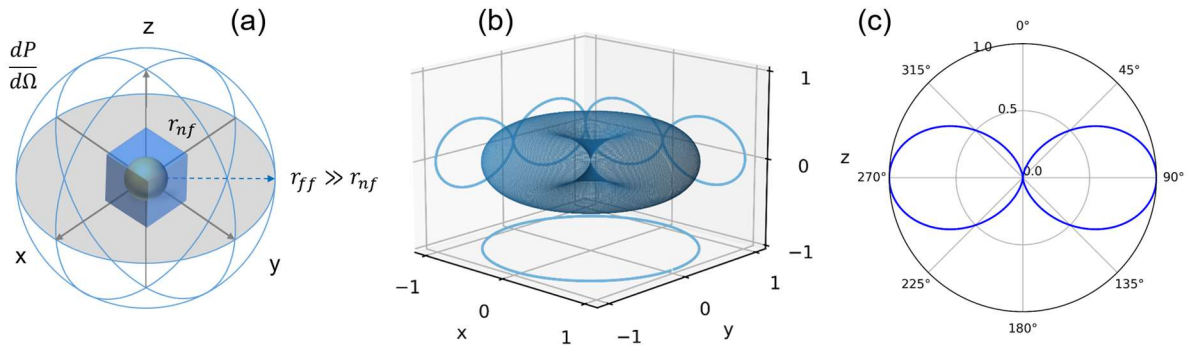

Figure 1.11 (a) FDTD simulation environment. A cube cell represents calculating near field distribution and corresponding far-field at a radius r_{ff}. (b) 3D and (c) 2D radiation patterns of Au sphere of 50 nm diameter by a CW plane wave excitation of 636 nm computed by Meep FDTD solver

Figure 1.11 (a) depicts a 3D FDTD simulation environment. A cube cell represents calculating the near-field distribution (r_{nf}) and corresponding far-field differential power $dP/d\Omega$ at a radius r_{ff}. Here we introduce a Au sphere of 50 nm diameter illuminated by plane wave polarized along the z-axis for an example. Figure 1.11 (b) and (c) shows the corresponding radiation patterns.

There is no need for a large simulation cell to compute the far-field radiation. More efficiently, a near-field box is set to accumulate the reference flux without structure first. Then the flux is computed with structure with sufficient time-stepping. By subtracting the reference flux, Meep allows the user to compute corresponding far fields as $\vec{E}, \vec{H}$ according

to the flux and resulting total outgoing Poynting vector $\vec{S} = \vec{E} \times \vec{H}$ at a large far-field circle with $r_{ff} \gg \lambda$. Radiation patterns in Figure 1.11 (c) show the angular distribution of the magnitude of the time-averaged Poynting vector $|\vec{S}|$ in the xy-, yz- ,and the xy- plane.

From Figure 1.11, we can observe here dipole mode dominates in radiation in all cases. In the radiation patterns in the xy-plane and yz-plane, the beamwidth $\Delta\theta$ of radiation of the 50-nm Au sphere resembles that of the Hertz dipole ~90°.

In conclusion, many different physical properties of EM problems can be obtained and some of them are presented according to all the previous examples calculated by the Meep FDTD solver. This helps one to gain a quantitative understanding of experimental radiation patterns. Electrodynamics in the FDTD scheme will be applied in the following contents.

1.8 Summary

In this chapter, we have demonstrated basic principles about optical microscopy and spectroscopy. With knowledge of surface plasmons (SPs), we can gain better understanding in surface-enhanced (SE) and tip-enhanced (TE) Raman spectroscopy. The experimental instruments of the TE optical microscope and their operation principle are presented. The excitation source plays a pivotal role in optical imaging, and the explicit forms of the higher-order laser modes are fully expressed. Radiation dynamics of the Hertz dipole and the radiation patterns are visualized. Electrodynamics simulations in the FDTD scheme are used for understanding the EM properties of irregular geometries. All the previous contents provide a basic introduction to the following works.

Chapter 2
Electromagnetic and Chemical Enhancements of SERS and TERS using Au Nanodisks[1]

Surface-enhanced Raman scattering (SERS) was discovered by Fleischmann *et al.* in 1974[44] and recognized by Richard P. Van Duyne in 1977[45, 61]. SERS spectroscopy has been developed rapidly and widely applied in sensing[127, 128], spectroelectrochemistry[129-131], single-molecule spectroscopy[49], and many more fields until now. The physical mechanism of SERS has been widely discussed, especially when new SERS substrates are proposed[132, 133].

By providing enormously amplified electromagnetic (EM) fields for the excitation and scattering, the surface plasmon resonance (SPR) is believed to play a significant role in SERS and TERS as the EM enhancement[20, 36]. The EM field enhancement depends on the materials and the geometry of the probe and substrate in TERS. On single nanoantennas[99, 120], EM fields can be concentrated in the vicinity of the apex of the tip. The EM field can be further positioned and enhanced by the gap-mode geometry, in which the sharp tip is located in the vicinity of the metal surface. Sub-molecular optical resolution can be achieved[58] using TERS with a scanning tunneling microscope (STM).

When the probe molecule is chemically adsorbed on the metal surface, another Raman enhanced channel through the charge transfer (CT) process (from metal to molecule

[1] This chapter is based on the published paper, Chen, Yu-Ting, et al. "*Charge transfer and electromagnetic enhancement processes revealed in the SERS and TERS of a CoPc thin film*." Nanophotonics 8.9 (2019): 1533-1546. Part of the images and the text in this chapter are based on or adapted from this publication.

and vice versa) may come into play[134]. When the excitation wavelength matches one of the CT processes, a chemical enhancement of a specific Raman mode can be observed. In recent years, with the application of two-dimensional materials such as graphene or carbon dihalide as SERS substrates, chemical enhancement is usually proposed as the main enhancement mechanism[132, 133]. Sun *et al*. had presented four types of CT that can be identified in the TERS configuration. There is a surge of interest in the field of TERS to sub-molecular imaging, it is necessary to study the mechanisms for enhancing Raman spectroscopy and to weigh their effects separately. In particular, both metal-molecule and molecule-metal CT enhance specific Raman modes, which is useful for manipulating chemical reactions at the single-molecule level in photocatalysis.

Using physical vapor deposition (PVD) with well-defined adsorption geometry and controlled surface coverage, transition metal phthalocyanines (TMPcs) can be deposited on a variety of substrates. This is very useful for understanding the influence of molecular orientation on SERS enhancement. In the case of strong interactions, the electronic structure of both molecules and metals can be changed. As revealed by photo-excited electron spectroscopy, the local CT from the metal substrate to the central metal atom of CoPc affects the CT state of Co ions[135]. These characteristics make TMPcs an ideal sample for discussing the chemical enhancement in SERS and TERS.

Here, we unravel the SPR, CT resonance, and molecular resonance underlying the enhancement by two-color SERS and TERS measurements using 2-nm CoPc thin films deposited on Au surfaces. Radial and azimuthal polarization are used to evaluate the contribution of the polarization-dependent EM enhancement and to determine the averaged orientation of the molecular film. Different colors of excitation lasers, 636 nm, and 532 nm, were used to study the resonance Raman process and determine the CT process between CoPc molecules and Au substrate. The optical contrast observed in the TERS image was analyzed.

2.1 Experimental Results

2.1.1 An Overview of the Sample and Confocal Images

The details of the home-built confocal setup and the SPM are fully described in Chapter 1 (see Figure 1.3 and 1.4), which are not reproduced in this chapter. Here we utilize two colors λ_{ex} =532 nm, 636 nm as the excitation source in the microscope.

For this study, a periodic array of Au nanodisks (NDs) was fabricated on Au substrates by electron beam lithography (EBL), whose overview of the sample is shown in Figure 2.1 (a). Under ultra-high vacuum (UHV) conditions, a nominal 2-nm CoPc film is prepared by organic molecular beam deposition. This sample was prepared by Dr. Diana Davila Pineda, Prof. Dr. Raul D. Rodriguez.

Figure 2.1 (a) schematically shows a Au ND array area (on) and Au film (off). The dimension of each Au ND is characterized by height h =20 nm and the diameter D =80 nm. The edge-to-edge distance P_x, P_y between NDs in x and y directions are both 200 nm. Notably, Au ND is a structure with D/h~4 and shown in Figure 2.1 (c) with a curvature at the center.

Figure 2.1 (b) presents backward scatterings from the Au ND array measured by a dark-field microscope (DFM) using an objective of NA~0.5 with a white light source. The inset is the magnified view of the dimensions of the Au ND array. The SPR from the scattering shows the resonance around 945 nm. Two wavelengths of 636 nm and 532 nm are applied as the excitation source, which is highlighted in Figure 2.1 (b). It can be seen that the scattering by 532 nm excitation is nearly zero, which can be considered as off-resonance, while the scattering with the excitation of 636 nm is more intense and closer to the SPR of the Au ND array.

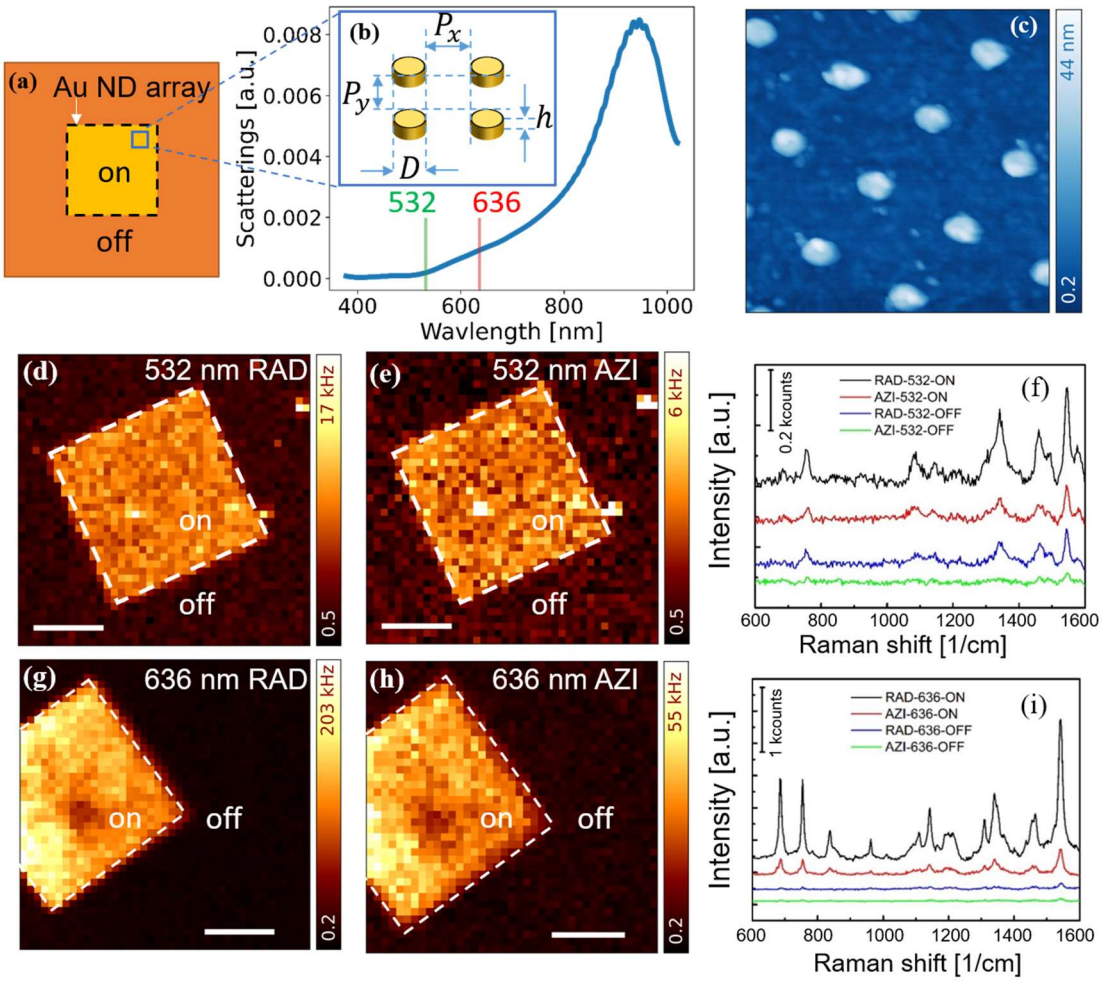

Figure 2.1 Sample and optical measurements (a) Schematic overview of sample, which consists of Au nanodisk (ND) array (on) and Au film (off) with CoPc deposited. (b) Scattering from the Au ND array. The inset is the magnified view of the Au ND array with dimensions. (c) Topography image by AFM with $1\ \mu m \times 1\ \mu m$ scan range (d)-(e) and (g)-(h) Confocal images from the Au ND array using 532 nm excitation (λ_g) and 636 nm excitation (λ_r). The scale bars inside are $10\ \mu m$. The abbreviation "RAD" denotes the radial polarization, and "AZI" denotes the azimuthal polarization. The excitation power of the sample is ~200 μW at $\lambda_{ex} = 636\ nm$, the excitation power of the sample is ~50 μW at $\lambda_{ex} = 532\ nm$. The SE Raman spectra obtained at different excitation wavelengths λ_{ex} = (f) 532 nm and (i) 636 nm.

Figure 2.1 (d)-(e) and (g)-(h) are confocal optical images recorded by a raster scan of the sample through the laser focus. Two excitation wavelengths (532 nm and 636 nm) and two laser polarizations (radial and azimuthal) are used. The abbreviation "RAD" denotes the radial polarization, and "AZI" denotes the azimuthal polarization. The optical image is $40\ \mu m \times\ 40\ \mu m$ large. In each of these panels, one can see a rectangular bright

area, which results from the optical intensity of the Au ND arrays highlighted with a dashed square. The position "on" represents the rectangular bright area, and "off" indicates the area outside the bright area. The Raman intensity in “on” and “off” (or capitalized letters) areas excited by λ_{ex} are defined as $I_{Raman}^{on,off}(\lambda_{ex})$ accordingly.

Due to the diffraction limit of the microscope, individual Au NDs with side-to-side distances P_x, P_y in x and y directions cannot be resolved well. The optical intensity difference can be observed between the λ_{ex} and the two polarizations. With the same λ_{ex} and the same excitation power, the optical contrast excited by the radial polarization is stronger than that by the azimuthal polarization. After normalizing the excitation power of the two lasers to the same value, the optical contrast under $\lambda_{ex} = 636\ nm$ is higher than under $\lambda_{ex} = 532\ nm$. The topographic image by atomic force microscope (MultiMode 8-HR, Bruker AFM) shows more details of the dimensions in Figure 2.1 (c).

The SER spectra of CoPc on nanostructured Au are shown in Figure 2.1 (f) excited by $\lambda_{ex} = 532\ nm$ and excited by $\lambda_{ex} = 636\ nm$ in Figure 2.1 (i). All the spectra were excited with a laser power of 200 μW and an integration time of 60 secs. The most prominent Raman modes ($\upsilon = 1463, 1540\ cm^{-1}$) in the spectrum is the in-plane mode[136]. It can be observed that overall $I_{Raman}^{on}(\lambda_{ex}) \gg I_{Raman}^{off}(\lambda_{ex})$ for $\lambda_{ex} = 532\ nm, 636\ nm$ as shown in Figure 2.2. This is consistent with the optical contrast in the images in Figure 2.1 (d)-(e) and (g)-(h). Fittings are performed by non-linear least-square algorithms[137] with a free Python package in the following contents. After fittings by the Lorentzian model, the ratio of the Raman intensity $I_{1540\ cm^{-1}}^{on}/I_{1540\ cm^{-1}}^{off} \cong 20$ by 636 nm excitation with the radial polarization. All the details for the data analysis can be found in the original work[102].

Based on the results of polarization-dependent X-ray absorption spectroscopy (XAS)[136], for a ~2 nm CoPc film deposited on a rough Au surface, the molecular plane of the interface layer tends to be parallel to the substrate surface ("lying"). As the film thickness increases, they gradually become vertical ("upright"). The SER spectra contain contributions from all of the molecules within the laser probe volume, which gives rise to ensemble-averaged signal. By changing the polarizations from radial to azimuthal

polarizations, the polarization-dependent Raman intensity can be observed. The Raman intensity is optimal using the radial polarization due to the standing molecules.

2.1.2 Tip-Enhanced Optical Images Correlated to Topography

In addition, TE optical images with correlated topographic maps are displayed in Figure 2.2. Signals of TE optical images are composed of Raman scatterings and PL. TE optical images are performed at different excitation wavelengths $\lambda_{ex} = 532\,nm$ and $636\,nm$. In Figure 2.2 (a) and (b), the dimension of images excited by 532 nm is $500\,nm \times 500\,nm$. And Figure 2.2 (c) (d) show the dimension of images excited by 636 nm with $1\,\mu m \times 1\,\mu m$.

The morphology in Figure 2.2 (b) reveals the presence of six adjacent Au NDs. The formation of the topographic image is a convolution of the morphology of the Au tip and that of the object. The topographic image affected by the tip morphology can be clearly observed. The tip morphology is degraded during the scans and the geometry of the tip apex has deviated from a sphere. The position of these NDs in Figure 2.2 (b) correlates well with the optical bright features in Figure 2.2 (a).

One can see the correlation between the TE optical and the topographic images. Figure 2.2 (c) and (f) show the details of this correlation along the dashed lines in Figure 2.2 (a) (b) and (d) (e). Evidently, the optical signals are stronger in the tip-Au ND configuration than that in the tip-Au film configuration.

The TE spectra excited by $\lambda_{ex} = 532\,nm$ and $636\,nm$ are shown in Figure 2.2 (g) (h). The photoluminescence (PL) intensity with $\lambda_{ex} = 532\,nm$ is more significant than that with $636\,nm$ as the excitation. By contrast, the Raman intensity with $\lambda_{ex} = 636\,nm$ is higher with a weaker PL intensity. The optical spectra of Au tip with $\lambda_{ex} = 636\,nm$ shows some Raman peaks, which is attributed to the inevitable contamination during the near-field imaging scans. Overall, the TE optical intensity (Raman and PL) on Au ND is stronger than that at the position between Au NDs (btw 4 NDs).

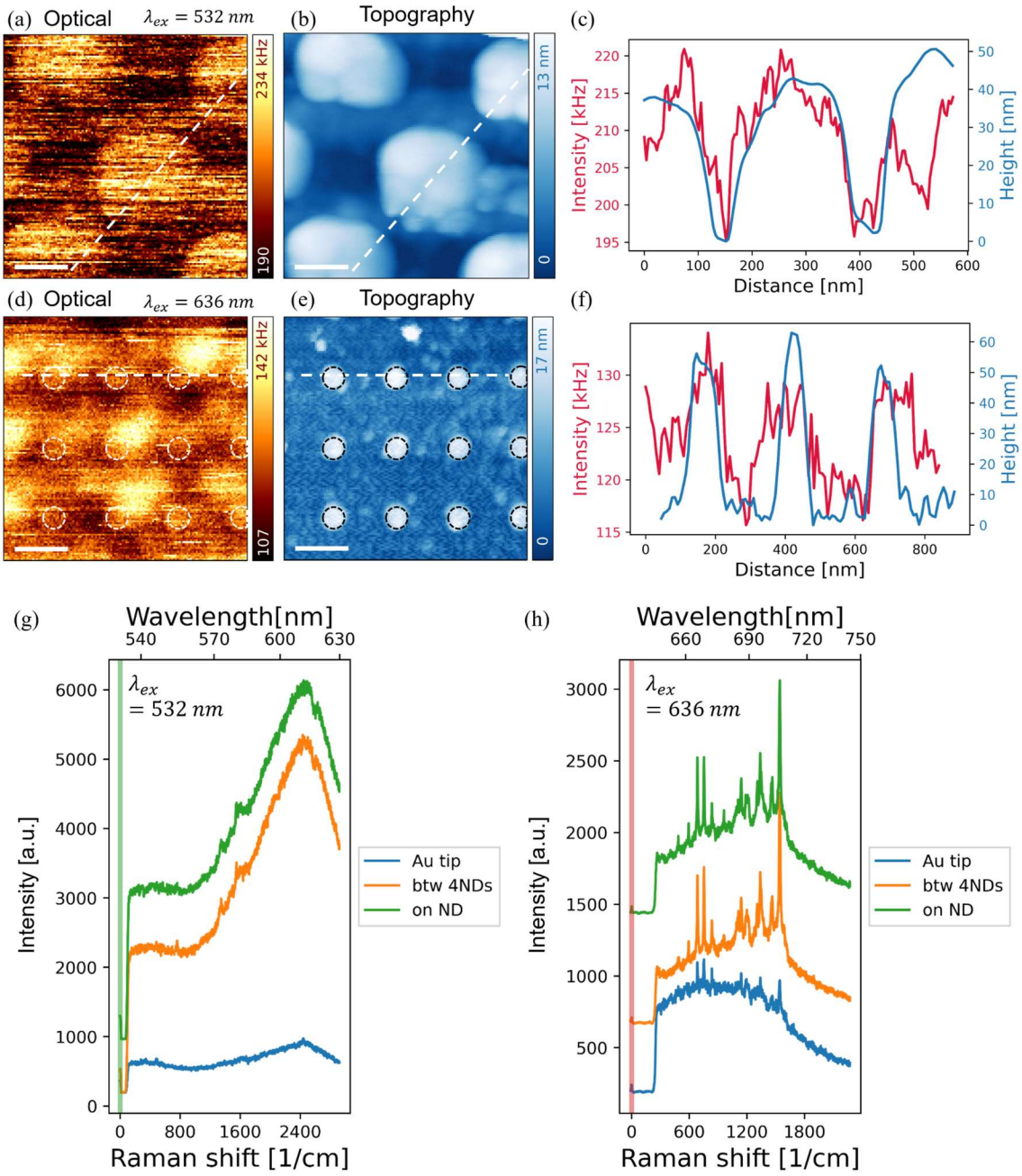

Figure 2.2 Simultaneous scan for optical and topographic images under λ_{ex} = (a) 532 nm and (d) 636 nm. (a) and (d) are TE optical images. (b) and (e) are corresponding topographic images. The inserted scale bars are 100 nm in (a) (b) and 200 nm in (d) (e). For the excitation of 532 nm and 636 nm, the excitation power is ~200 μW. Radial polarization is used for excitation in the tip-enhanced measurements excited by 532 nm and 636 nm. (c) and (f) show a correlation between the optical intensity (λ_{ex} = 532 nm and 636 nm) and its topographic height along the dashed lines. (g) (h) show spectra with different excitation wavelengths (λ_{ex} = 532 nm and 636 nm) The excitation source with radial polarization is applied. The integration time of spectra with $\lambda_{ex} = 532\ nm$ and 636 nm are 60 secs and 10 secs respectively.

2.2 Discussion

Lombardi and Birke proposed a unified expression for SERS[138]. The expression of the polarizability α is composed of three terms under different conditions, which is written as $\alpha = \mathrm{A} + \mathrm{B} + \mathrm{C}$. A is related to Frank-Condon integrals. Herzberg-Teller contributions from metal-molecule or molecule-metal charge transfer (CT) transitions are expressed by B and C.

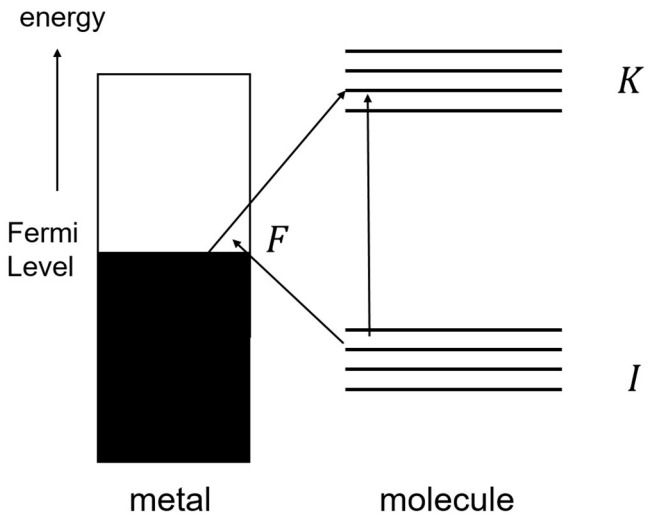

Figure 2.3 Schematic energy diagram of the metal-molecule system[20]. *I, F,* and *K* denote the ground state, the charge transfer state, and the excited state respectively according to the work by Lombardi and Birke[60, 138].

In, Figure 2.3, *I*, *K*, and *F* are the ground state, the excited state, and the charge transfer (CT) state. Furthermore, three entangled resonances for the SERS enhancements[60, 138, 139] are revealed in the terms by Herzberg-Teller coupling. These contributions to the SERS enhancement factor (EF) are (i) the EM enhancement due to the SPR of the nanoparticle, (ii) a CT resonance involving the electrons between the molecule and the conduction band of the metal nanoparticle, and (iii) resonance within the molecule alone.

If the molecule is placed in the vicinity of a metal nanoparticle, the analytic form of $\alpha_{IFK}(\omega)$ related to the three contributions with consideration of the metal-molecule CT can be expressed as[138]

$$\alpha_{IFK}(\omega) \propto \frac{1}{[(\varepsilon_{\mathrm{r}}(\omega)+2\varepsilon_D)^2+\varepsilon_i(\omega)^2](\omega_{FK}^2-\omega^2+\gamma_{FK}^2)(\omega_{IK}^2-\omega^2+\gamma_{IK}^2)} \quad (2\text{-}1)$$

where $\varepsilon_r(\omega)$ and $\varepsilon_i(\omega)$ are the real and imaginary parts of the complex dielectric constant of the metal[140](i.e. $\varepsilon_{\mathrm{metal}}(\omega)=\varepsilon_{\mathrm{r}}(\omega)+i\varepsilon_i(\omega)$), and ε_D is the dielectric constant of the environment. ω is the excitation frequency. ω_{FK} and ω_{IK} are the frequencies of the charge transfer process between states *F* and *K* and between *I* and *K*, respectively. γ_{FK} and γ_{IK} are the damping factors of the transitions between states *F* and *K* and between *I* and *K* respectively. Thus, the Raman intensity is proportional to the square of the Raman polarizability $|\alpha_{IFK}(\omega)|^2$.

The energy diagram at the interface between Au and a CoPc molecule is presented in Figure 2.4 with values of $\Delta, \Phi_{Au}, \Phi_{CoPc}$ etc. according to the work by Petraki *et al.*[141] The three contributions to SERS are included in Figure 2.4 and shown as (1), (2), and (3), which correspond to the three factors in the denominator of equation (2-1). The details will be further discussed factor by factor in the following sections.

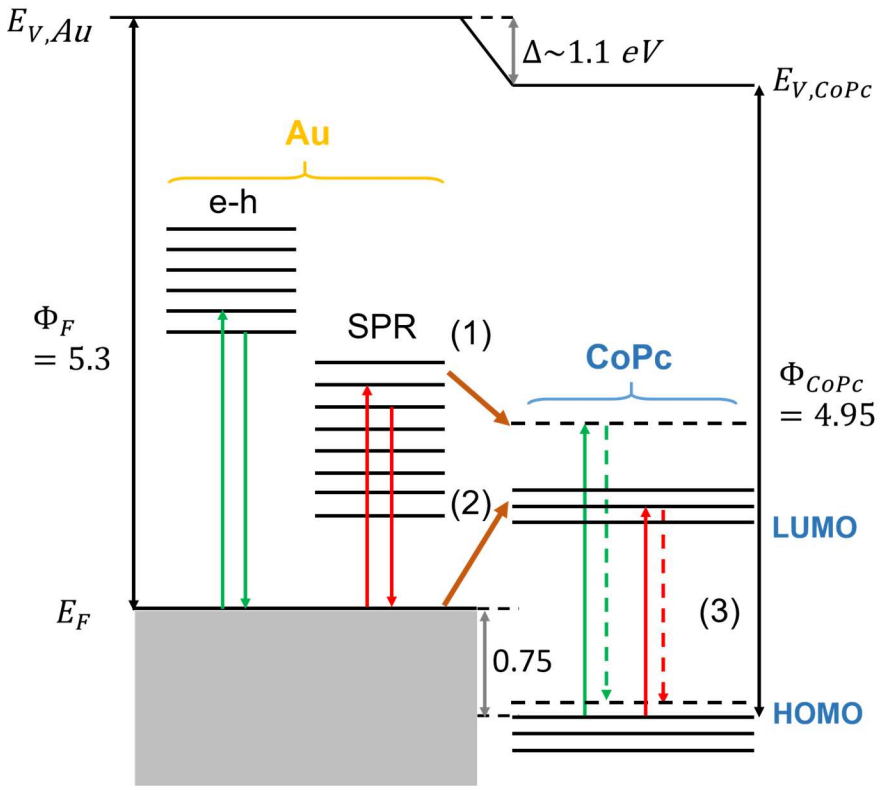

Figure 2.4 Schematic energy diagram at the interface between Au and a CoPc molecule. E_F denotes the Fermi level of Au in units of eV according to the work by Petraki *et al.*[141] Three contributions to the SERS effect are plotted as (1), (2), and (3). The surface plasmon resonance (SPR) states in Au (shown as SPR) can be excited by 636 nm (1.9 eV) In addition, electron-hole (e-h) pair states by interband transitions in Au can be excited by only 532 nm (2.3 eV). The HOMO-LUMO transition in CoPc is resonantly excited by a 636 nm laser while non-resonantly excited by a 532 nm laser. The dark orange arrow in pathway (1) shows the charge transfer (CT) from the SPR states to the LUMO of the CoPc molecule. The other dark orange arrow in pathway (2) denotes the metal-molecule CT process. The downward dashed arrows indicate the Stokes Raman processes. (3) 532 nm laser excites the molecule non-resonantly, thus a black dashed line represents a virtual level as the excited state.

2.2.1 Surface Plasmons Resonance (SPR)

We will now discuss the contribution of the EM enhancement underlying the experiments of SERS and TERS, which is described in the first factor in the denominator in equation (2-1) and corresponds to process (1) in Figure 2.4.

First, we discussed the influence of different excitation wavelengths on the EM enhancement of SERS signals. For Au films, the surface roughness helps break the conservation of momentum, allowing far-field light to be coupled to the surface plasmon polaritons (SPPs) propagating at the interface. Otherwise, this mechanism is forbidden[20]. According to the literature[20], the SERS enhancement factor is an order of $10^3 \sim 10^4$ due to the EM enhancement. For SERS measurements, the SPR of Au NDs needs to be considered. This effect accounts for the intensity difference or optical contrast between the Au ND array and the surrounding Au thin film as shown in Figure 2.1 (d)-(e) and (g)-(h). In the quasi-static approximation, the polarizability of the Au nano-sphere α_{Au} is resonant when $\varepsilon_1(\omega_{ex}) = -2\varepsilon_D$ where $\hbar\omega_{ex}$ is excitation photon energy. The SPR condition depends on $\varepsilon(\omega)$ of the metal itself and the surrounding media $\varepsilon_D(\omega)$. The measured SPR from Au ND array is shown in Figure 2.1 (b) and 636 nm excitation is closer to the resonance condition. A more complicated form of polarizability[142] needs to be introduced for different geometries than a sphere. Applying the model of a spherical particle in the proximity of a flat surface, the effective polarizability of the coupled tip-surface system can be also derived[143]. Here, we only point out the properties of the relative permittivity of Au in the optical range and compare the SE and TE Raman intensities according to the $|E|^4$-approximation[20] (see Chapter 1).

I. The Dielectric Function of Au

The frequency response of noble metals can be described by a complex dielectric function $\varepsilon(\omega) = \varepsilon_{\mathrm{r}}(\omega) + i\varepsilon_i(\omega)$. Qualitatively, two different mechanisms contribute to the dielectric function of Au. The instant response of conducting freely moving electrons according to the external driving EM field, which can be expressed by the Drude model[144, 145] as

$$\varepsilon_{Drude}(\omega) = \varepsilon_{\infty} - \frac{\omega_p^2}{\omega^2 - i\gamma\omega} \tag{2-2}$$

where ω_p is the plasma frequency, γ denotes the damping factor while electrons move in metal and ε_{∞} represents residual polarization due to the positive background of the ion core.

According to the experimental data from Johnson and Christy[140], the dielectric constant of noble metals (Au, Ag, etc.) $\varepsilon_i(\omega)$ is small and $\varepsilon_{\mathrm{r}}(\omega)$ is negative[140]. In particular, $|\varepsilon_{\mathrm{r}}(\omega)| \gg 1$. Therefore, metallic nanostructures are generally used to generate local surface plasmon oscillations in the visible spectral range. The dielectric responses of Ag follow the Drude behaviors well. However, the interband transitions in Au occur in the spectral range. The dielectric responses of Au must be modified, especially the imaginary part. This mechanism is considered as the Lorentz-like form[145, 146], which can be written as

$$\varepsilon_{Lorentz}(\omega) = \frac{\Delta\varepsilon \cdot \Omega_p^2}{\Omega_{\mathrm{p}}^2 - \omega^2 - i\Gamma\omega} \tag{2-3}$$

where Ω_{p}, Γ are the plasma frequency and damping factor for bound electrons, and $\Delta\varepsilon$ is a weighting for interband transitions. Generally, multiple $\varepsilon_{Lorentz}(\omega)$ should be added to the dielectric function of Au[145].

Thus, the overall dielectric function of Au in the optical frequency range can be expressed as

$$\varepsilon_{Au}(\omega) = \varepsilon_{\infty} - \frac{\omega_p^2}{\omega^2 - i\gamma\omega} + \sum_{s=1}^{4} \frac{\Delta\varepsilon_s \cdot \Omega_{p,s}^2}{\Omega_{p,s}^2 - \omega^2 - i\Gamma_s\omega} \tag{2-4}$$

where the Drude parameters $\omega_p = 8.8$ and $\gamma = 0.08$, the Lorentz parameters $\Delta\varepsilon_s$, Ω_s and Γ_s are tabulated as Table 2.1.

Table 2.1 The parameters in the Drude-Lorentz model $\Delta\varepsilon_s$, Ω_s and Γ_s

s	$\Delta\varepsilon_s$	Ω_s	Γ_s
$s = 1$	0.277	2.6	0.23
$s = 2$	0.419	2.8	0.4
$s = 3$	0.984	3.2	1
$s = 4$	1.529	4.5	1.7

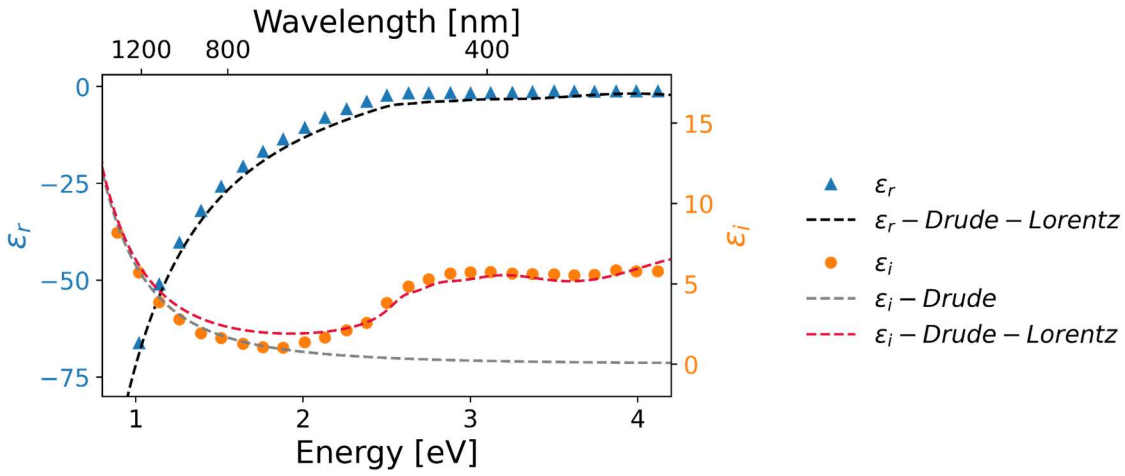

Figure 2.5 Dielectric responses ε_r (triangles) ε_i (circles) according to experimental data from Johnson and Christy[140] compared with the models of Drude (gray dashed line) and Drude-Lorentz (ε_r: black dashed line, ε_i: red dashed line).

The dielectric function of Au is shown in Figure 2.5. The blue triangles and orange circle points denote ε_r and ε_i of the experimental data from Johnson and Christy. The dashed lines represent the Drude model and the Drude-Lorentz model according to

equation (2-4) with parameters in Table 2.1. The dielectric response of Au follows Drude behaviors up to $\sim 2\ eV$ as shown in Figure 2.5. The experimental ε_i follows ε_i by the Drude model (gray dashed line). As the incident photon energy is larger than $2\ eV$, the $\varepsilon_i(\omega)$ of Au will increase due to interband absorption, which attenuates the SPR.

The surface plasmon resonance (SPR) states in Au (shown as SPR) is excited by both lasers of 636 nm ($\cong 1.9\ eV$) and 532 nm ($\cong 2.3\ eV$), which both produce PL accordingly by electron-hole recombination denoted by corresponding colored downward arrows. As we discussed in the previous section by the Drude-Lorentz model, the interband transitions occur with the photon energy higher than $2\ eV$. The e-h pairs states in Au can be excited by only 532 nm ($\cong 2.3\ eV$). Notably, the SPR states are not only SERS effect but also increasingly populated by introducing a Au tip as TERS, and the transition from SRES and TERS will occur.

Thus, the excitation efficiency of surface plasmons in Au at 532 nm is much lower than that at 636 nm due to the interband absorption or equivalent large damping. The corresponding local field enhancement caused by the tip-ND is still greater than that by the tip-film.

II. SE and TE Raman Due to Surface Plasmons

The overall EM field enhancement by $\lambda_{ex} = 636$ nm is expected to be more significant than that by λ_{ex}= 532 nm. The Raman peak intensity of $\lambda_{ex} = 636\ nm$ is 2 ~ 4.6 times stronger than that of λ_{ex}= 532 nm (different from one peak to another). This observation agrees with the theoretical prediction that the field enhancement at the Au tip excited by 636 nm is almost 5 times higher than that is excited by 532 nm excitation[147].

First, we discuss the polarization dependence on the EM enhancement. The presence near the conductive metal surface may cause a frequency shift in the SPR of the nanostructure[148, 149]. The plasmonic mode of two local dipoles can be excited and their intensity is varied by tuning the polarization of excitation (from s-polarized to p-polarized). Two peaks in the dark field scattering spectrum are realized[149]. This stems from the interaction between the dipole modes in the nanoparticle and the image dipole in the film. When the electric field of the polarized light is parallel to the film, the in-plane (parallel to the film) image dipole moment is opposite to that in the nanoparticle. Hence the net

scattering from the Au nanoparticle disappears. Then, the nanoparticle and its image dipole can only be polarized perpendicular to the surface, which yields a greater dipole intensity[149, 150]. Therefore, when the radially polarized laser beam is applied, the Raman intensity is always stronger regardless of both of the excitation wavelengths than for the azimuthally polarized laser beam as shown in Figure 2.1.

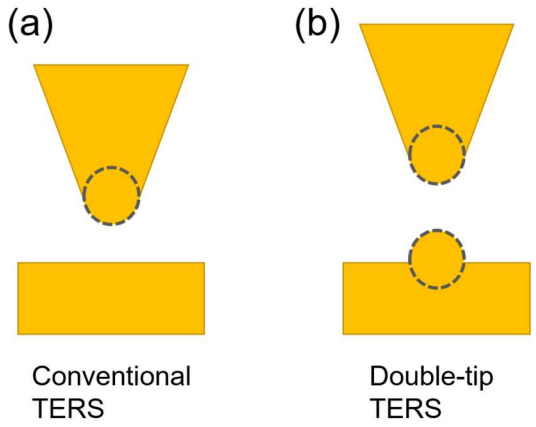

Figure 2.6 Schematics of (a) the conventional TERS and (b) the double-tip TERS configurations

Second, the TERS intensities of the Au tip-Au ND are more intense than those of the Au tip-Au film. According to the topographic images in Figure 2.1 (c), the geometry of Au NDs can be approximated as a hemisphere embedded in the Au film. The EM field enhancement is further increased by the double-tip configuration due to the lightning rod effect[151, 152]. In the double-tip TERS configuration of the Au tip-Au ND, the Au ND acts as the second tip[153, 154] with a higher curvature than the plane surface in the conventional TERS configuration (see Figure 2.6). We follow the definitions in the FDTD calculations[153, 155], the local EM field enhancement is defined as $M = \left|\frac{E_{loc}}{E_{in}}\right|$. The corresponding ratio R of the double-tip TERS and conventional TERS configurations thus becomes

$$R_{\text{doub}\ -\text{tip/conventional}} = M^4_{\text{doubl}\ -\text{tip}} / M^4_{\text{conventional}} \qquad (2\text{-}5)$$

The calculated ratio R of the double-tip TERS configuration and the conventional TERS (tip and flat substrate) configuration is ~2.2. In our TERS measurements under $\lambda_{ex} = 636\,nm$, the ratio of the integrated Raman intensity of the double-tip (tip-Au ND) and the conventional TERS (tip-Au film) configuration is 1.6~2.5 (different from one peak to another). The ratios are tabulated in Table 2.2. These values are comparable to the FDTD simulations[153].

Table 2.2 The ratios R of the double-tip and conventional TERS configurations at different Raman modes according to the experimental data

$v[cm^{-1}]$	684	754	960	1460	1545
$R_{\text{double-tip/conventional}}$	1.62	2.04	2.47	2.51	2.24

2.2.2 Charge transfer (CT) Resonance

Let us turn to the second factor in the denominator, which describes the contribution of the CT process and corresponds to process (2) in Figure 2.4. For $\omega = \omega_{FK}$, the laser can resonantly excite the CT process. The CT process from the Fermi level E_F of Au to the LUMO of the CoPc molecule is proposed in Ref[156].

Relative Raman Intensity Ratios

It is corroborated that for copper phthalocyanine (CuPc) in the spectral region of about 650 nm, the symmetrical Raman mode (such as B_{1g}) "borrows" the intensity from the permissible molecular transition (Q band) through the CT resonance[157]. The Raman intensity ratio between the metal center-related vibration mode and the benzene ring vibration mode had been used to evaluate the strength of the CT process between CuPc and Au foil or MoS_2[157].

For the CuPc molecule, the vibration mode of ν =749 cm^{-1} is assigned to the in-plane N-Cu stretching. The vibration mode of ν =1530 cm^{-1} is the in-plane symmetrical non-metallic N-C stretching[157]. The intensity ratios $I_{749\,cm^{-1}}/I_{1530cm^{-1}}$ are calculated according to the data, which are shown in Table 2.4.

Table 2.3 The intensity ratios of Raman modes of $\nu = 749\ \mathrm{cm}^{-1}, 1530\ \mathrm{cm}^{-1}$

	Position [ON/OFF]	λ_{ex} [nm]	$\frac{I_{749\ cm^{-1}}}{I_{1530 cm^{-1}}}$
SERS	OFF	636 nm	0.236
TERS	ON		0.187
	OFF		0.206
SERS	ON	532 nm	0.412
TERS	ON		0.41
	OFF		0.452

Here, we follow the same considerations to evaluate the contribution of the CT process between CoPc and Au substrates in our experiments. For CoPc molecules, the vibration mode involving the central metal appears at ν =749 cm^{-1}, and the non-metallic bond N-C stretch is located at $\nu = 1530$ cm^{-1}. According to Table 2.3, For SERS-OFF and TERS-ON and -OFF excited at 636 nm, the intensity ratios $I_{749\ cm^{-1}}/I_{1530 cm^{-1}}$ are ~0.2. While using 532 nm excitation light, the ratios of the geometry increase to ~0.4. This implies that the CT process between the CoPc and Au substrates by 636 nm is higher than that by 532 nm, which matches the resonance excitation of the Q band. It is worth noting that the ratios are comparable in the SERS and TERS experiments, exhibiting the strengths of the CT process are similar in both cases.

Considering our experimental conditions, the distance between the tip Au substrate is ~3 nm [158-160]. It is unlikely to have additional CT paths, such as the tip-molecule CT process[153].

Analysis of the Background Emission with the 532-nm Excitation

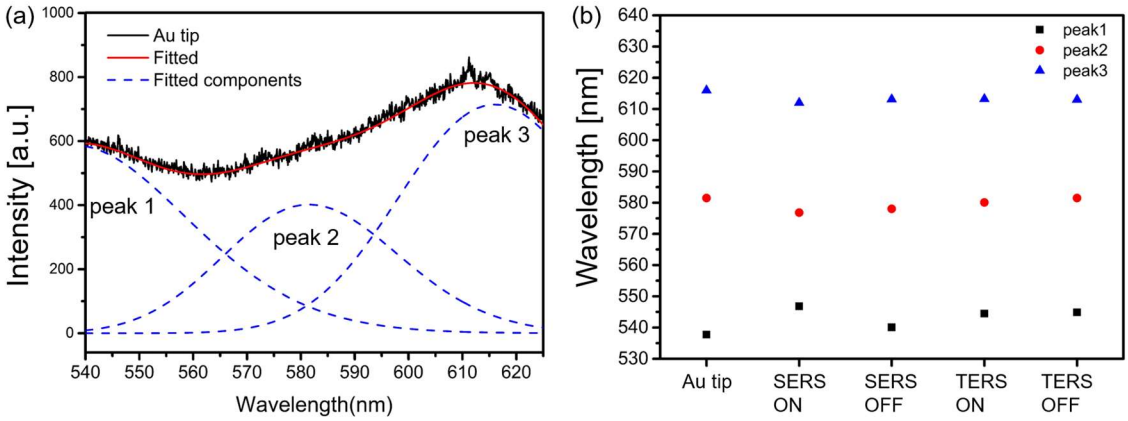

Figure 2.7 (a) Fittings of the spectral background from the Au tip. The black curve is the original spectrum. Three Gaussians (blue dashed curves) are used for fittings. The red curve is the sum of the Gaussian fittings. (b) Comparisons of the peak positions of peaks 1, 2, and 3, which are extracted from the spectra of the Au tip, SERS ON/OFF, and TERS ON/OFF.

The spectral background is prominent with the excitation of 532 nm. We begin with the analysis of the Au tip spectrum obtained excited by 532 nm, as shown in Figure 2.7 (a). Similarly, fittings are performed with other conditions as SERS ON/OFF and TERS ON/OFF. The overall spectral shape agrees with the literature[161]. Its spectral shape appears to be similar to the extinction or scattering spectrum[162-164]. The Au tip shows a strong spectral background, with a maximum of about 615 nm under the excitation of 532 nm. Since the PL from the Au tip is emitted after the interband absorption process. When the tip is close to the Au film or Au NPs, the PL intensity increases rapidly, and the maximum peaks remain at almost the same positions (Figure 2.7 (b)). This might result from the large apex of the Au tip. The mechanism of the Au PL and the local field enhancement in the gap-mode configuration will be discussed more in detail in Chapter 3.

Here, a molecule-metal CT process from the LUMO of CoPc to the electron-hole states of Au may occur. From there, the electron can release further energy, for example by emitting photons. Therefore, the PL intensity with 532-nm excitation is even stronger.

2.2.3 Molecular Resonance

We now turn to discuss the contribution of the molecular resonance process, which is the third term in the denominator and corresponds to process (3) in Figure 2.4. For resonance condition $\omega = \omega_{IK}$, the resonance Raman process[28, 165, 166] occurs between the ground state of the electron and the excited state of the molecule.

The molecular structure of CoPc contains delocalized 18 π electrons surrounding the central metal atom, forming a two-dimensional π electron conjugate system. The light absorption spectrum of CoPc shows two main absorption regions: the Soret band of about $300\sim400\ nm$ and the Q band of 600~900 nm, which are all due to the π-π* electronic transition. In particular, two peaks appear in the Q band. The high-energy peak at about 620~635 nm originates from the first π-π* transition on the phthalocyanine macrocycle[167]. The photon energy of the 636 nm laser coincides with the HOMO-LUMO separation of CoPc (1.96 eV [168]) as shown in Figure 2.4. Therefore, the molecular resonance process is one of the reasons why the Raman intensity is stronger under $\lambda_{ex} = 636$ nm than $\lambda_{ex} =$ 532 nm, as shown in Figure 2.1 (f) and (i).

On the other hand, the excitation photon energy of 532 nm excites the ground states to a virtual energy level shown as a dashed black line. The dashed arrows indicate the Stokes Raman processes. Thus, the excitation wavelength of 636 nm excites Raman processes resonantly while 532 nm excites non-resonantly.

2.2.4 Interpretation of the TE Optical Images

Let us turn back to the TE optical images shown in Figure 2.2 (a) and (d) at different excitation wavelengths λ_{ex} =532 nm, 636 nm. Based upon the former discussion, we can understand the optical contrast of the TE optical images better. From the optical spectra, we can conclude that the predominant signals in the TE optical images originate from PL. And now we discuss them in detail in the following sections.

The TE PL signals and topographic height profiles are shown in Figure 2.2 (c) (f), whose correlation along the cross section line can still be observed. In the optical and the topographic images in Figure 2.2 (d) (e), the contour of NDs is highlighted with white and

black dashed circles. The TE optical features can be observed and correlated to the topography of NDs.

532-nm Excitation Wavelength

For the TE optical image in Figure 2.2 (a) with the excitation wavelength of 532 nm, the light signal is mainly PL signal formed by the light-induced CT process from molecules to the metal. Due to the double-tip geometry, this process can be enhanced by the stronger EM enhancement. The PL intensity due to interband transitions in Au can be seen according to the spectra. The mechanism underlying the correlated optical and topographic images may stem from the molecule-metal CT process to the electron-hole pair state of Au and decay to the ground state. Hence the bright optical features in the TE optical image can be directly correlated to the position and size of each Au ND.

636-nm Excitation Wavelength

On the other hand, the optical contrast of the TE optical image with excitation wavelength 636 nm excitation is shown in Figure 2.2 (d). The correlation between the optical and topographic images cannot be clearly seen, which is assumed to arise from the superimposed SE and TE optical signals.

The optical contrast of the SE signal can be observed between four adjacent Au NDs (marked with four large white dashed circles). The full-width at half maximum (fwhm) of the central lobe of radial polarized fields is calculated as ~300 nm [83] with an excitation of 636 nm by the PM (see Section 1.4.3). The SE optical signals are superimposed when the laser focus is at the center of four adjacent Au NDs. Consequently, this gives rise to strong background optical signals in the images.

2.3 Conclusion

In this study, the entangled resonances of the SPR, the CT, and the molecular resonance are unraveled by two-color SE and TE optical spectroscopy and microscopy. The molecules with averaged molecular orientations in the 2-nm CoPc film off/on Au NDs probed by radial and azimuthal polarizations. We found that the SE Raman intensity

excited by 636 nm is greater than that excited by 532 nm due to the better overlap with the SPR. The radial polarization as excitation results in greater SE Raman intensity, which is attributed to dipole-image dipole interactions. The correlated topographic image helps us to disentangle the array structures with specific spectral measurements. Through the double-tip TERS configuration, the TE Raman intensity of Au tip-Au ND is stronger than Au tip-Au film due to the lightning rod effect. The CT resonance is also excited more intense by 632 nm than 532 nm according to relative Raman intensities. The molecular resonance in the CoPc molecule is also discussed. The insights obtained in this work help one to understand the mechanisms of SERS and TERS and the optical contrast in TE optical imaging.

Chapter 3
Evolution of the TERS Hot Spot by Varying the Gap Size[2]

Surface-enhanced Raman scattering (SERS) is a significantly amplified inelastic scattering predominantly due to the surface plasmon resonance (SPR). The physics of SPs is briefly demonstrated in Chapter 1 (see Appendix B for more details). The SP waves are concentrated at a metal surface and its corresponding field amplitude decreases exponentially as the distance from the surface increases. Furthermore, it has been found that spatially highly concentrated EM fields occur at sharp corners of various nanoparticles, e.g. nanocubes[169], nanostars[170, 171], nanotriangles[172], triangular nanoprisms[173]. The local field in the vicinity of the nanostructures is not uniform and this results in different SERS activities. More importantly, the local field enhancement in the proximity of the metallic nanoparticles depends on the curvature of the surface. In particular, one can find the highest field enhancement in the vicinity of the region with the highest curvature[61]. These spatial regions with the enormously high field enhancement are called 'hot spot'[20, 36, 66, 68, 69, 174-176], which manifest strong SERS activity.

In addition to nanoparticle monomers, nanoparticle dimers with a nanometer-gap can create intense field enhancements. This effect can be observed in inter-particle nano-gap, and particle-slab nano-gap[50, 51, 68]. The SERS enhancement factors (EF) of Au nanosphere dimers can increase from 10^5 to 10^9 by decreasing the gap size from 10 nm to

[2] This part of work is in the process of submission. Majority of the text and figures are used in the manuscript.

2 nm[20, 68, 177]. The distance-dependence of the SPR had been experimentally demonstrated with variable isolation layer thickness[178]. Similarly, the molecule-substrate distance dependence of the SERS EFs is revealed[179]. It has been established that Raman enhancing efficiency scales as r^{-10} [180, 181]; however, measuring SERS signals from nanoparticles separated by a few nanometers from each other (or one another) is difficult. Tian and co-workers had developed the technique of shell-isolated nanoparticle-enhanced Raman spectroscopy (SHINERS)[182]. The nanoparticles are constituted of Au quasi-spherical cores encapsulated in thin alumina or silica. In the core-shell nanoparticles, their SERS intensity decays as the thickness of the shell increases[183, 184].

Though the SHINERS technique offers promising analytical and sensing applications, precise control over the location of the hot spot is still difficult to perform. Tip-enhanced Raman spectroscopy (TERS)[54, 56, 57] with highly concentrated fields between the tip and the substrate becomes an invaluable tool to control the hot spot and achieve high sensitivity[41]. The distance dependence between a single emitter and nano-antennas is presented and quenching of molecular PL intensity is attributed to multipolar contributions[97]. De-quenching of a single emitter in the nano-sized gap is also elaborated theoretically and realized experimentally[98]. The gap dependence reveals the coupling process, which can be performed by the tip-surface configuration[80, 185].

In this work, we aim to provide clear insight into the hot spot in the vicinity of the tip-surface configuration by comparing the tip-enhanced optical measurements with corresponding hot spots from simulations. Gap-dependent TE optical measurements using CoPc on Au film and CuPc on single-crystal Au are performed. Different increasing tendencies of the intensity of Raman signals and background emission are observed. Moreover, as the gap size decreases, the TE Raman intensity increases more dramatically than that of the background emission. The local field enhancement can be quantified by computational methods, which can visualize the hot spots of the plasmonic structures and even lead to better designs with different functions. We study the field enhancement as a function of gap sizes quantitatively by comparing the experimental results with electrodynamics simulations in the FDTD scheme.

3.1 Experimental Methods

3.1.1 Samples and Preparations

Two samples are prepared for tip-enhanced optical measurements by different approaches. The first sample (Sample 1) is monolayer CuPc (Copper Phthalocyanine) prepared by thermal evaporation on single-crystal Au (Au(111)) under ultrahigh vacuum (UHV) conditions. Its thickness is estimated as 0.3 nm. Sample 1 is provided by Katharina Greulich. The other sample (Sample 2) is a 2-nm CoPc (Cobalt Phthalocyanine) deposited on a Au substrate. A 50-nm-thick Au film was evaporated onto a silicon wafer coated with a chromium film (2 nm thick). A CoPc film with a 2-nm thickness was deposited on the sample by organic molecular beam deposition under UHV conditions as well. Sample 2 is prepared by Dr. Diana Davila Pineda, Prof. Dr. Raul D. Rodriguez.

3.1.2 Sample Approaching Methods and Experimental Conditions

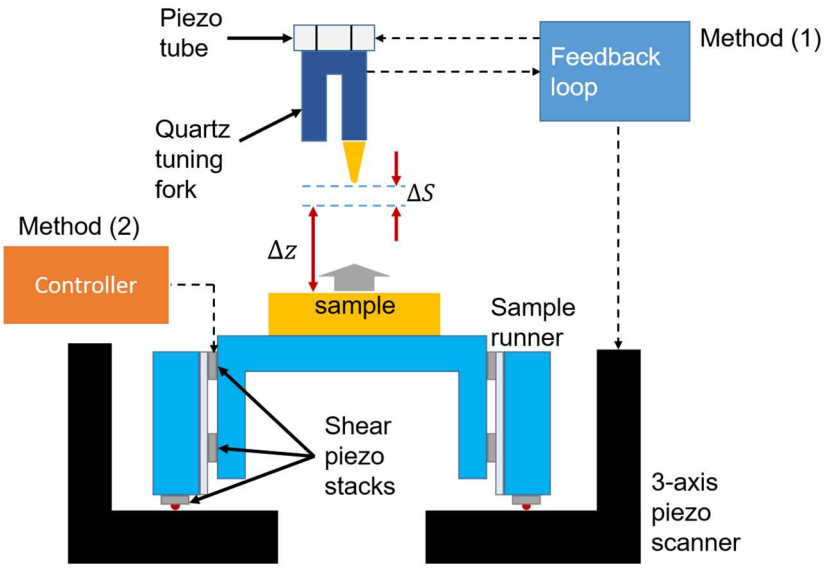

Figure 3.1 Schematic of the SPM setup with two samples using two approaching methods: Method (1) and (2). Δz denotes the sample moving range. ΔS denotes the initial gap size as the sample starts to move.

The details of the optical layout and the connections of the SPM setup can be found in Chapter 1 (see Figures 1.3 and 1.4). A simplified overview of the SPM setup is shown

in Figure 3.1. The Au tip of 35-nm apex diameter is made by electrochemical etching. The sample is mounted on a sample holder, which can be moved by the shear-piezoelectric stacks in 3-axis directions. This sample runner stands on the 3-axis piezoelectric scanner. After the Au tip is positioned in the optical focus, the sample is driven to approach the Au tip. Two sample approaching methods with different experimental conditions are utilized in the following TE optical measurements.

Method (1): Sample 1 is moved by shear piezoelectric stacks until the SPM controller receives the feedback signals. The SPM controller can drive Sample 1 to perform continuous movements with successive voltages. In the meanwhile, optical signals are recorded by an APD and a spectrometer with a grating of 150 grooves/mm for better collecting efficiency. The acquisition time for each spectrum is 1 sec. The excitation wavelength is 632.8 nm (HeNe laser) with power of ~200 μW. This part of the experimental results shows overall plasmonic behaviors and will be presented in Section 3.2.

Method (2): After every single z-axis step of the sample runner, the corresponding optical signals from Sample 2 are recorded by the spectrometer with the 600 grooves/mm-grating. Each spectrum is measured with a 10-secs exposure time for a proper signal-to-noise ratio. The excitation wavelength is 636 nm (diode laser) with the same power as the HeNe laser. This part of the experimental results aims to observe the evolution of the TE Raman enhancements and will be presented in Section 3.4.

3.2 Optical Spectra with Varied Gap Sizes

Figure 3.2 (a) shows the evolution of optical spectra as a function of the total gap size Δz_{tot}. Sample 1 is used for the following section. The tip-sample distance (or the gap size) is initially maintained as a constant ΔS, which is estimated as ~3 nm. 1-nm z-position accuracy of the 3-axis piezoelectric scanner is provided by the shear-force feedback loop.

Δz_{tot} is therefore assigned as $\Delta S + \Delta z$, where Δz denotes the sample moving range. $\Delta z = 0$ occurs at the initial position $z = z_0$ as shown in Figure 3.2 (a), which yields $\Delta z_{tot} = \Delta S + \Delta z \cong \Delta S$. In reality, Δz is not always zero in each z scan (or z movement)

due to the reproducibility issue of the piezoelectric scanner in the z-direction. This will harm the reproducibility of optical measurements. The 3-axis piezoelectric scanner is used to drive the sample towards the Au tip at a speed of ~ 0.6 nm/s (Figure 3.1). The z-position control will be inaccurate if the moving speed is slower than this speed.

In addition, the sample is firstly driven to $\Delta z = 30$ nm ($z = \Delta z_0 - 30$) followed by a movement back to $\Delta z = 0$ ($z = \Delta z_0$). This movement is shown as an inset in Figure 3.2 (a). The shear-force feedback control is deactivated during each z scan of the sample. Optical emission spectra are taken from bottom position Δz =30 nm until original position Δz =0 nm simultaneously. Optical signals collected by APD and demodulated phase shift of the quartz tuning fork are obtained simultaneously as well. These two quantities are abbreviated as "APD" and "Phase" in the remainder of the section and the figure. Figure 3.2 (f) shows approach curves of optical signals collected by APD indicated as APD-forward (backward) while the sample moves forward (backward) to the Au tip. The forward and backward approach curves do not overlap within the range $\Delta z = 4 \sim 7$ nm. This may result from hysteresis of the piezoelectric scanner. The phase shift in Figure 3.2 (g) drops from $-4°$ to $\sim -36°$, which indicates the probe-sample induced shear-force. Nicely overlapped forward and backward approach curves implies that the sample has not yet crashed Au tip.

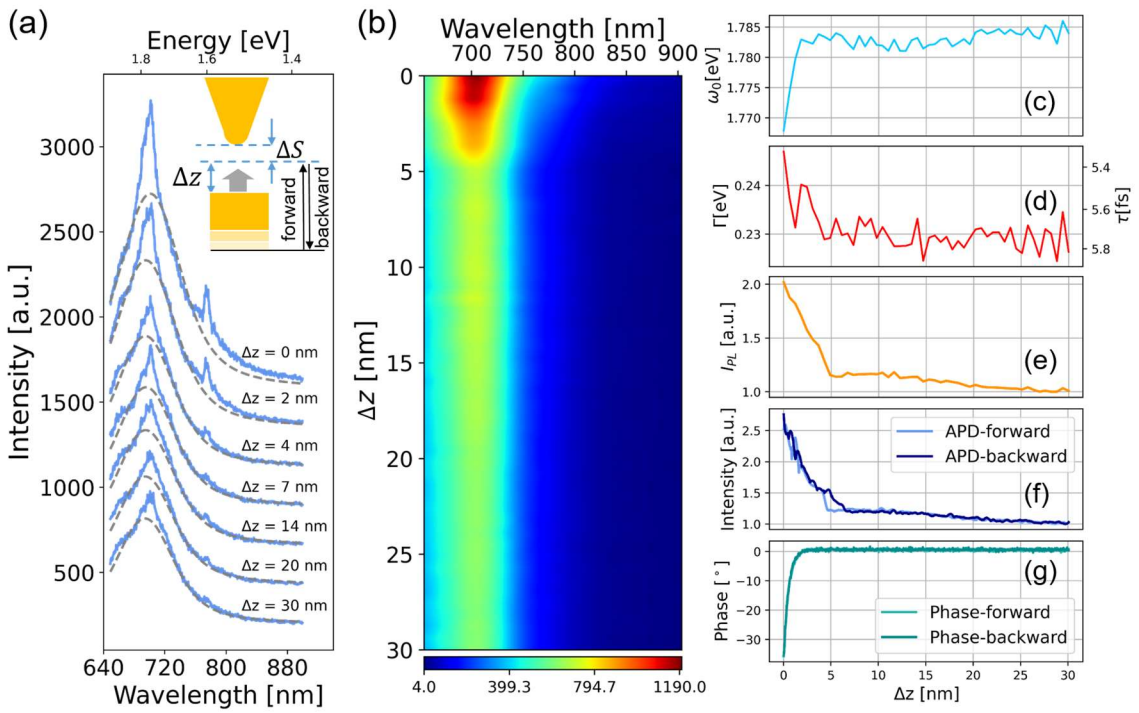

Figure 3.2 (a) PL spectral evolution from Au tip-Sample 1 as a function of the sample moving distance Δz. The inset shows the initial gap ΔS with $\Delta z \leq 30\ nm$. Au PL is separated and plotted in (b). Analysis of spectrum with parameters (c) peak ω_0, (d) fwhm Γ and (e) intensity I_{PL} derived from the Voigt model shown in the gray dashed lines in (a). (f) The optical intensity collected by APD and (g) the phase signals are recorded during sample approaching (forward) and retracting (backward).

Photoluminescence (PL) from bulk Au was presented with the band structure of the metal by Mooradian in 1969 [186]. This process has a very low efficiency since metals do not have a band gap. In solids, PL is a three-step process, which is comprised of photoexcitation of electron-hole pair, the relaxation of the excited electrons and holes, and eventually emission from the electron-hole recombination. In metals, the non-radiative process will predominantly proceed through electron-hole pair recombination to the ground state, which renders radiative decay from Au considerably weak. The quantum yield (QY) of PL from bulk Au is on the order of 10^{-10} [186]. Interband transitions preferably occur near X and L symmetry points of the first Brillouin zone[187, 188] since the density of states is high in the regions close to X and L symmetry points[161, 162, 189, 190]. Intraband transitions in Au bulk crystal require large momentum and this restuls in weak Au PL yield[162, 191].

Local surface plasmons (LSPs) are widely acknowledged to improve the emission process[161, 162, 192-194]. LSPs make intraband transitions probable since they couple near fields with large momentum to far-field radiation[162]. Boyd *et al.* had demonstrated that Au PL from rough Au surfaces is due to the local field enhancement of Au nanoparticles by a phenomenological model and the experiments[195]. PL yield from nanocrystals is greatly enhanced by LSPs by several orders of magnitude[191, 196]. And the PL process is also plasmon-modulated[163, 197] by nanoparticles. Probable pathways for yielding Au PL from Au nanorods are also discussed by Wackenhut *et al.*[198] These works help us to see the mechanism of the Au PL process with deeper insights.

It can be observed that broad PL signals predominate the overall optical signals in Figure 3.2. Those with sharper peaks are not considered here. The broad continuum spectra are attributed as PL from the Au tip. The tip-surface plasmonic resonance can also be obtained due to the close correlation between PL and the surface plasmon resonance (SPR)[163, 194].

Let us turn to the spectral analysis as demonstrated in Figure 3.2. Inevitable cosmic spikes and dips due to the dead pixels of the CCD are commonly observed in the measurements and these fictitious data points are removed by the Whitaker-Hayes algorithm[199]. The broad PL signals and the residual sharper signals from gap mode are separated by the asymmetric least-square algorithm[200]. PL spectra is fitted by the Voigt model (gray dashed lines in Figure 3.2 (a)) by using a Python package[137] of non-linear least square minimization. The PL signals are plotted in Figure 3.2 (b), showing an observable red-shift in the peak of PL. Voigt-model fittings in spectra are shown in Figure 3.1 (a). Parameters of the Voigt model for fittings are peak ω_0, the full width at half maximum (fwhm) Γ and intensity I_{PL} (normalized to minimum at $\Delta z = 30$), which are presented in Figure 3.2 (c)-(e). ω_0 is ~1.785 eV with Γ of ~0.23 eV, which generally agrees with the previous experimental results[80, 201, 202].

The linewidths of the broad peaks in plasmonic resonances are accepted to arise from photon emission (radiative damping) and dephasing or non-radiative damping[203, 204]. The match in peaks and linewidths between PL and the SPR according to scattering[163] implies that the PL process is associated with the same damping mechanism. The plasmon

linewidth[33, 80, 204, 205] at $\Delta z = 30$ nm is $\Gamma_{\Delta z=30\,nm} = 0.23$ eV (corresponding to $\tau = 2\hbar/\Gamma = 5.7$ fs shown on the right-hand scale of Figure 3.2 (d)), which is comparable to the linewidths of Au nanorods[203].

The PL intensity $I_{PL}(\Delta z)$ is increased ~2 times as the sample moves from $\Delta z = 30$ nm to the proximity to Au tip ($\Delta z = 0$ nm) in Figure 3.2 (e). In other words, the PL intensity increase ratio is $\frac{I_{PL}(\Delta z=0)}{I_{PL}\,(\Delta z=30)} \cong 2$. Compared with different sets of approach curves, the average value of $I_{PL}(\Delta z)$ increase ratio $\langle\frac{I_{PL}(\Delta z=0)}{I_{PL}\,(\Delta z=30)}\rangle \cong 1.8$ where the angle brackets denote average over different sets of spectra. When Δz turns ~5 nm, the PL intensity starts to increase significantly for $\Delta z \leq 5$ nm. The extent of the PL peak redshift can be observed as 3 to 6 nm. This redshift is not significant since the tip-surface coupling has not yet entered quantum coupling via the STM feedback[80].

The red-shifted PL peaks in the spectra reveal the coupling of a dimer[206], and the shift of SP energy varied with gap size in TERS had also been discussed[185]. Therefore, the spectral evolution of PL indicates that the Au tip increases the coupling strength with Au substrate as the gap width decreases. This phenomenon leads us to discuss the resonant behaviors of the Au tip and tip-substrate configurations.

3.3 Local Field Enhancements by FDTD Simulations

FDTD simulations can provide quantitative insights into EM responses for complicated geometry of various materials and surrounding environments, and the basic principles and details are described in Chapter 1. Here, we perform FDTD numerical simulations by free Python package Meep[125] for revealing the field enhancements in our configurations.

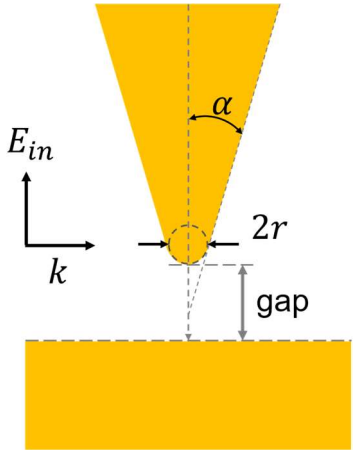

Figure 3.3 Schematic of simulation geometry with the incident wave E_{in} parallel to the long-axis of the Au tip. $2r$ denotes the diameter of the Au tip apex, and 2α represents the opening angle of the Au tip. The gap indicates the tip-sample distance.

The geometry of the Au tip with the Au substrate is presented in Figure 3.3. The coaxial incident wave E_{in} propagates from the left side of the overall geometry indicated by $\vec{k}$. $2r$ denotes the diameter of the Au tip apex, and 2α represents the opening angle of the Au tip. Two different Au tip apex diameters of 35 nm, and 110 nm are used in the experiments. Modeling of the Au tip geometry in the simulations is based upon these conditions. The relative permittivity $\epsilon(\omega)$ of Au is derived from the Drude-Lorentz model in Meep. The following simulations will show field intensity enhancement $|E_{loc}/E_{in}|^2$ with variable diameter $D = 2r$ with two different parameters D_1 =35 nm and D_2 =110 nm. The thickness of the molecular film here is neglected for simplifying the calculation. Two different sets of simulations according to the two diamters are organized in the following two sections. All the following simulations exclude the effects of nonlocal optical response[207-210].

3.3.1 Small Au Tip Apex

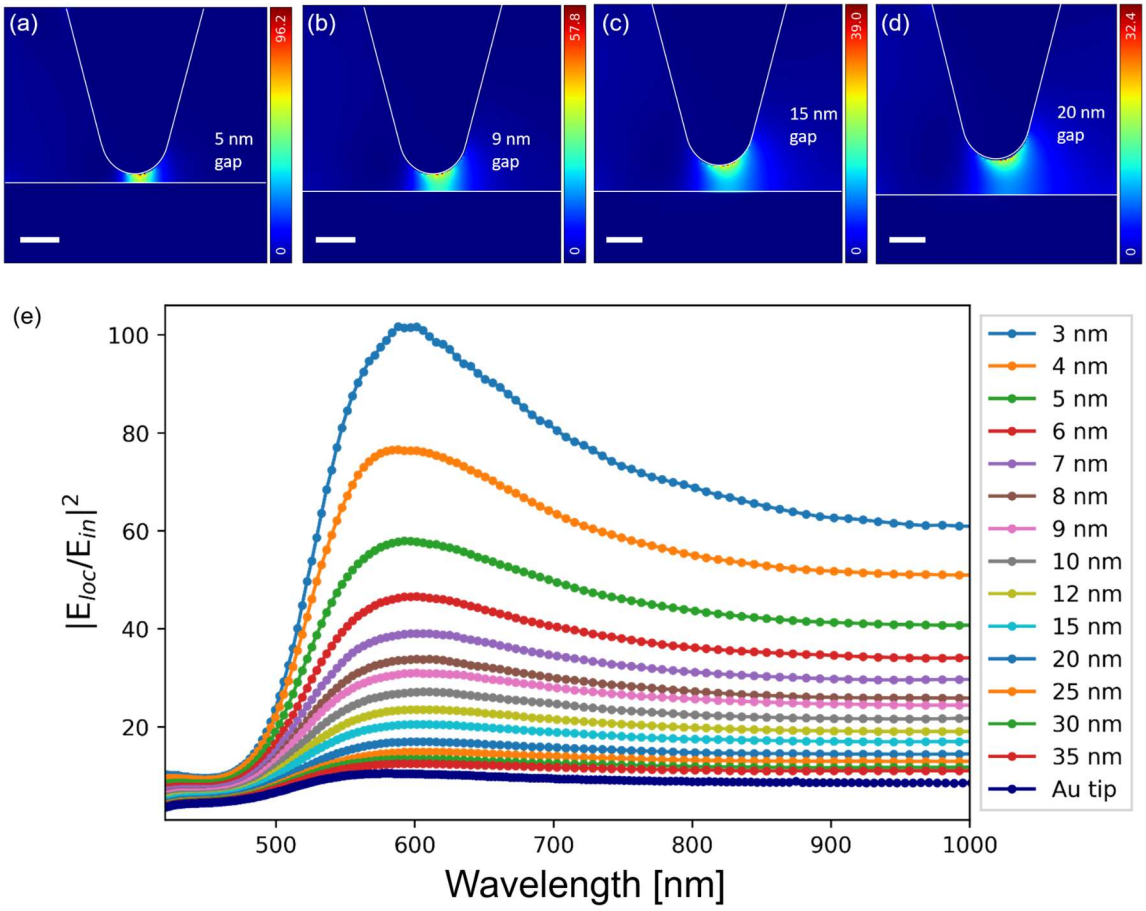

Figure 3.4 Field intensity enhancements $|E_{loc}/E_{in}|^2$ by FDTD of Au tip (small)-Au substrate with gap sizes of (a) 5 nm (b) 9 nm (a) 15 nm and (a) 20 nm with $\lambda = 636$ nm. The scale bar inside each panel is 20 nm. (e) Sequential wavelength-dependent field enhancements as a function of different gap sizes from 3 nm to 35 nm and Au tip alone

Figure 3.4 (a)-(d) depict spatial distributions of the calculated field intensity enhancement $|E_{loc}/E_{in}|^2$ of 3-nm 9-nm, 15-nm, and 20-nm gap sizes in the 35-nm Au tip-Au substrate configuration. The geometry of the Au tip is modeled according to our Au tip of a diameter of about 35 nm. The field enhancement is defined as the absolute value of the ratio of the steady-state local field E_{loc} divided by incoming field E_{in}. After sufficient time-stepping routines in the FDTD simulations, the field intensity enhancements $|E_{loc}/E_{in}|^2$ for a specified frequency is obtained. Furthermore, sweeping through a broad frequency range can yield a wavelength-dependent $|E_{loc}/E_{in}|^2{}_{max}$ as shown in Figure 3.4

(e). For clear understanding the SPR, the pixel with strongest intensity is removed in the wavelength-dependent $|E_{loc}/E_{in}|^2{}_{max}$. Only 99.9 % of the pixels in the calculated results are evaluated in $|E_{loc}/E_{in}|^2{}_{max}$. The gap enhancements in the 35-nm Au tip-Au substrate configuration are resonant at ~ 600 nm for all gap sizes, while the highest field enhancement of the Au tip is at ~570 nm with an ultrabroad bandwidth. The bandwidth of the field enhancement is getting narrower as the gap sizes decrease. Our excitation wavelength (636 nm) is close to the simulated SPR.

The highly confined fields and the hot spots of varied gap sizes are visualized in the sequence of the simulations. The field distribution becomes more concentrated and the field intensity is amplified as the gap size decreases. These results resemble the simulation results[211] and are consistent with the work in the early stage of SERS[45]. The molecule in the hot spot will exhibit the highest SERS activity[66]. If molecules are evenly adsorbed on the surface, only a tiny number of molecules can experience the hot spot and exhibit strong TERS activity. Furthermore, we can predict the maximum of $|E_{loc}/E_{in}|^4$ for the TERS enhancement factor (EF) according to the $|E|^4$-approximation[20] (see Chapter 1) is ~ $3.4 \cdot 10^4$ at the 3-nm gap size.

3.3.2 Large Au Tip Apex

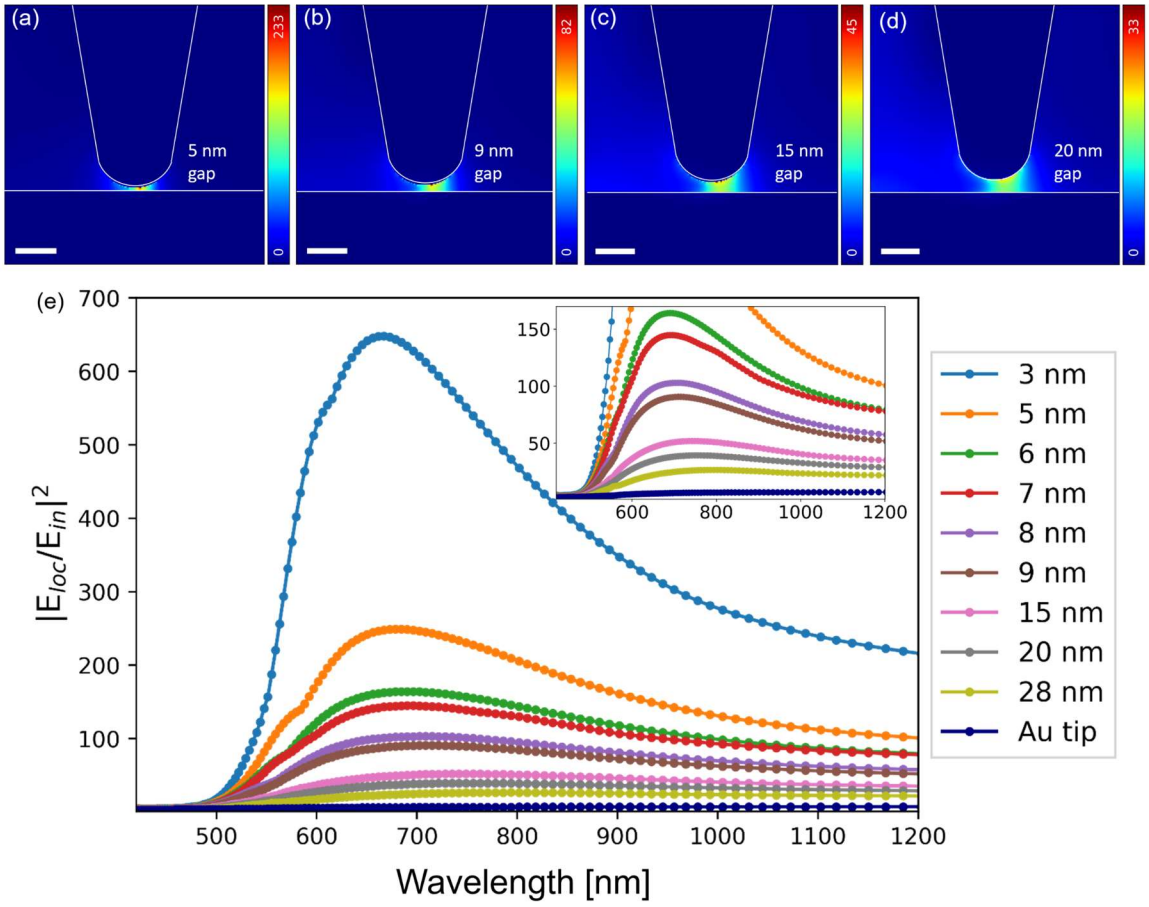

Figure 3.5 Field intensity enhancements $|E_{loc}/E_{in}|^2$ of Au tip (large)-Au substrate with (a) 5-nm (b) 9-nm (c) 15-nm and (d) 20-nm gap sizes by FDTD at $\lambda = 633$ nm. The scale bar inside each panel is 50 nm. (e) Sequential wavelength-dependent field enhancements as a function of gap sizes from 3 nm to 28 nm and Au tip alone. The inset is a magnified view of small enhancements.

Figure 3.5 (a)-(d) depict spatial distributions of the calculated field intensity enhancement $|E_{loc}/E_{in}|^2$ of 3-nm 9-nm, 15-nm, and 20-nm gap sizes in the 110-nm Au tip-Au substrate configuration. The wavelength-dependent field intensity enhancement $|E_{loc}/E_{in}|^2$ is shown in Figure 3.5 (e). The overall $|E_{loc}/E_{in}|^2$ are much stronger than that of small Au tip apex. Notably, the resonances of $|E_{loc}/E_{in}|^2$ only can be observable at a gap size of $\lesssim 15$ nm and the bandwidths of $|E_{loc}/E_{in}|^2$ become narrower. The gap-dependent local field enhancement distributions and the corresponding bandwidths behave similarly to the previous case. It should be emphasized that the size of the hot spot in this

simulation case is greater than the previous one (Section 3.3.1). The corresponding EF with the 3-nm gap is estimated as ~ $4.5 \cdot 10^5$ according to the $|E|^4$-approximation. This EF is larger than the previous one of the small tip apex by an order of magnitude. We can infer that the diameter of the tip apex plays a main role in the field enhancements in the tip-surface configuration.

3.4 Evolution of Tip-Enhanced Raman Scattering

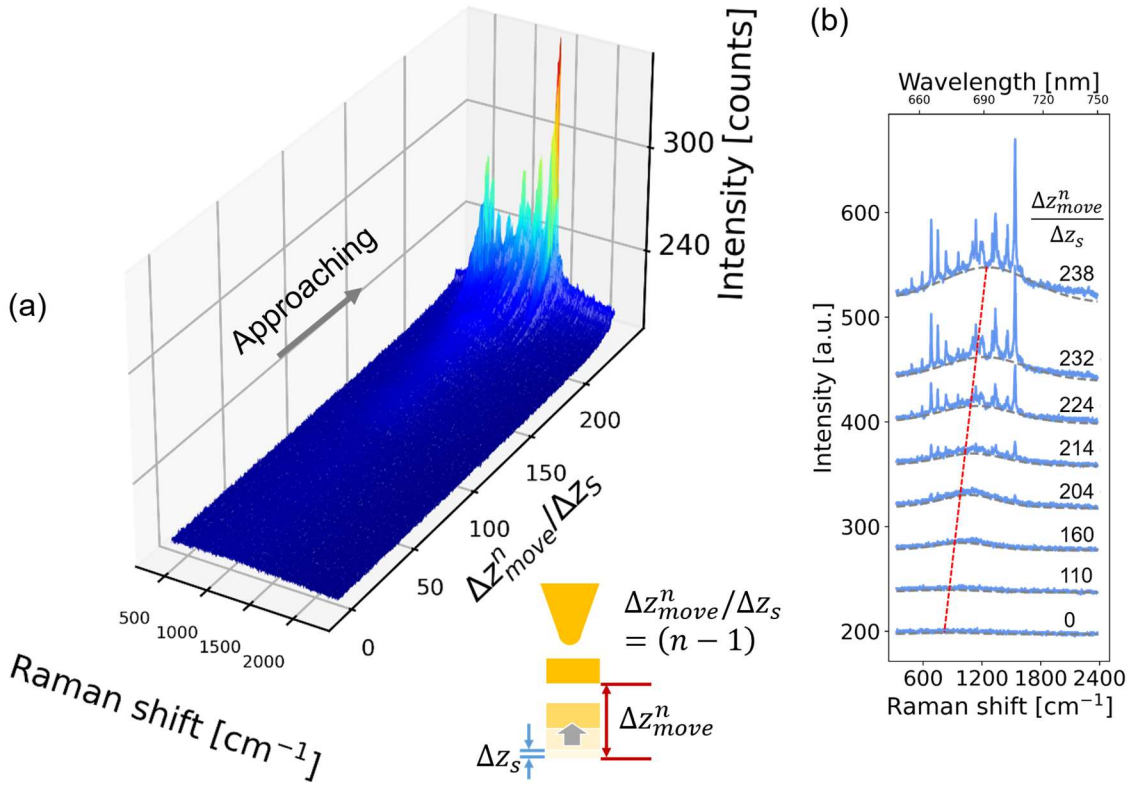

Figure 3.6 (a) Optical emission spectra as a function of sample movement $\Delta z^n_{move}/\Delta z_S$. The gap size is relatively smaller with larger $\Delta z^n_{move}/\Delta z_S$. The inset is a schematic of Au tip with moving Au substrate with the definition of $\Delta z^n_{move}/\Delta z_S$ (As the sample approaches, the $\Delta z^n_{move}/\Delta z_S$ increases) (b) Representative spectra with Voigt-model fittings (gray dashed lines) of different $\Delta z^n_{move}/\Delta z_S$. The red dashed line indicates the red-shifted PL peaks.

The sample approaching method for the following measurements is described in Section 3.1.2. Spectral evolution of PL signals as a function of $\Delta z_{move}^{n}/\Delta z_S$ is shown in Figure 3.6 (a). The intensity unit of each spectrum is counts with 10-secs integration time as shown in Figure 3.6 (a). The spectrum number n can be related to a step size Δz_s of each z-direction shear-piezoelectric stack for the sample movements. A dimensionless parameter $\Delta z_{move}^{n}/\Delta z_S$ with $n = 1, 2 \ldots 239$ can be defined to represent the total movement Δz_{mov}^{n} of the sample divided by the single-step Δz_S as shown in the inset of Figure 3.6 (a). The total movement after n steps Δz_{move}^{n} is a product of Δz_s and $(n-1)$. For instance, the total z-movement for spectrum $n = 1$ is $\Delta z_{move}^{n=1} = 0$. The total z-movement for the *n*th spectrum is $\Delta z_{move}^{n} = (n-1) \cdot \Delta z_s$. Overall, the total gap size Δz_{tot} is smaller with larger spectra number n and Δz_{move}^{n}.

After separation of the Raman and the PL signals, Voigt model fitting is performed for each PL spectrum again. Clear red-shifted PL peaks with narrowing gap sizes are highlighted by a red dashed line in Figure 3.6 (b). The results are consistent with the previous ones in Section 3.2.

What we can observe in Figure 3.6 is that each optical spectrum always contains a broad continuum. Before discussing the details in the Raman spectra, we need to discuss the origin of the SERS continuum (or background). The origin of the SERS continuum is still under debate. But evidence from the following works is provided to contribute to the SERS background. It had been discussed in detail that non-radiative decay occurs in thin-film structures[212]. The surface-enhanced (or metal-enhanced) PL of molecules on flat metallic surfaces has long been assumed to be impossible due to fast non-radiative decay into the metal[63]. In particular, the quantum yield (QY) of intrinsic PL in metal-Phthalocyanine (MPc) film (e.g. CuPc, CoPc, etc.) is too weak to be measured by emission spectroscopy without heating treatment[213]. Since our measurements are done in the ambient without thermal treatment as shown in Figure 3.6, here, the optical signals of the broad background are attributed to PL signal from the Au tip. All the other residual signals with sharper bandwidths are attributed to Raman signals from molecules in the spectra.

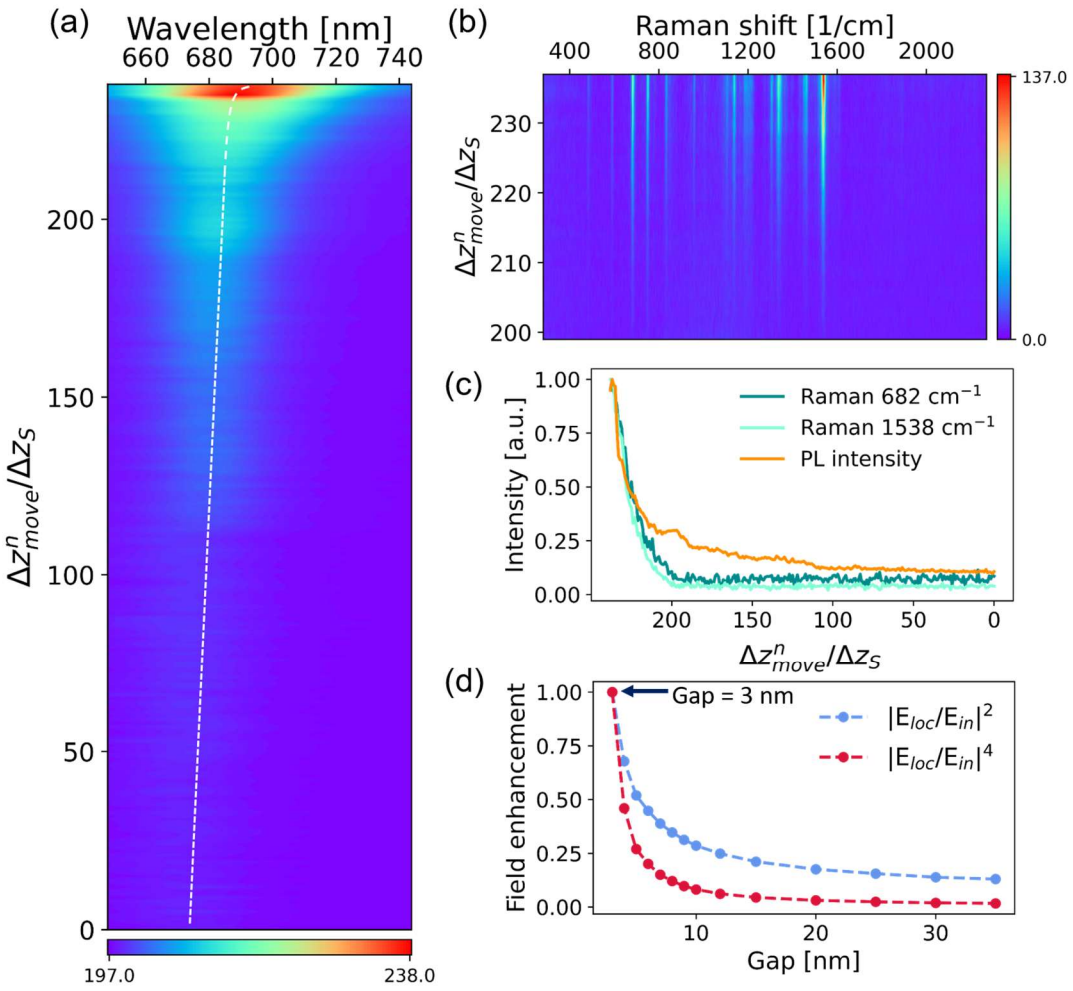

Figure 3.7 (a) Spectral evolution of PL as a function of $\Delta z^n_{move}/\Delta z_S$ (b) Spectral evolution of Raman scattering with varied $\Delta z^n_{move}/\Delta z_S$. (c) Normalized intensity of Raman modes ($\nu = 682, 1538\ cm^{-1}$) and PL vary with $\Delta z^n_{move}/\Delta z_S$. The Raman and PL intensity increases with the relatively smaller gap denoted by a larger $\Delta z^n_{move}/\Delta z_S$. (d) Field enhancements as a function of the gap size, which decreases from 35 nm to 3 nm. $|E_{loc}/E_{in}|^2$ indicate the surface plasmon behaviors and $|E_{loc}/E_{in}|^4$ represent the TE Raman behaviors.

Figure 3.7 (a) shows an observable red-shift of the PL peak (white dashed line) and the growing intensity I_{PL} with variable $\Delta z^n_{move}/\Delta z_S$ from $n = 1{\sim}239$. Spectral evolution of observable Raman signals as a function of $\Delta z^n_{move}/\Delta z_S$ of $n = 199{\sim}239$ is shown in Figure 3.7 (b). The Raman and PL intensities both increase as the sample approaches the Au tip. The PL intensity increases in a moderate manner while Raman intensity is still not yet observable. The Raman intensities of the total movement $\Delta z^{1\leq n<201}_{move}$ are immersed in

the noise level. The Raman intensity becomes observable after the sample movement turns $\Delta z_{move}^{n=201}$. It can be seen that the Raman intensity shows a rapid increase than the PL intensity increasing trend as the sample approaches.

The Raman enhancement factor (EF) due to localized EM waves can be evaluated by the $|E|^4$-approximation[20, 36, 70]. The Raman enhancement is stronger with spatially concentrated fields in closer proximity to the surface than the enhancement of surface plasmons (SPs). The distance dependence of SERS intensity is revealed[179] as inversely proportional distance to the power of 10. When it comes to the gap-mode TERS configuration, the distance dependence of TERS via the STM feedback shows a similar tendency[185]. The tip-surface dependence Raman and PL intensity are related[80]. Though our gap-dependent TERS measurements are carried out with no quantified moving range, predictions of this range by FDTD simulations are shown in Figure 3.7 (d). The $|\mathrm{E_{loc}}/\mathrm{E_{in}}|^2$ indicates of SPs and the $|\mathrm{E_{loc}}/\mathrm{E_{in}}|^4$ represents TE Raman enhancements. The field enhancements calculated by FDTD simulations could be scaled to resemble the experimental data. The sequence of simulations predicts the gap size ranging from 3 to 35 nm. The z-direction step size Δz_s by shear piezoelectric stack is estimated as ~ 0.15 nm accordingly.

If the gap sizes are much smaller than the minimum gap size that the shear-force control can achieve, plasmon behaviors will enter the quantum regime[214-218]. Nonlocality of the dielectric response of metal is proposed to be a possible mechanism[207, 219, 220]. In our experiments, we do not apply the STM feedback and the corresponding simulations show good agreement. The simulations without considering quantum tunneling and nonlocal effect are valid due to the gap size being greater than 2 nm via the shear-force feedback control.

3.5 Conclusion

The distance dependence of PL and TE Raman scattering cannot be obtained without proper calibration of the SPM controller (see Chapter 1). This part of work is crucial for a home-built setup to determine the sample moving range as well as the

topographic heights in images. The approach curves provide a clear picture of shear-force mechanisms. This SPM setup can be further extended to the STM feedback and enable measuring the electronic density of molecules and its density of states.

We have carried out tip-enhanced (TE) optical measurements with varied gap sizes. The corresponding FDTD simulations provide details in field enhancements both in wavelength-dependent responses and spatial distributions of the Au tip and the tip-surface configurations. It is observed that the redshift of the Au PL peak provides evidence of coupling between the Au tip and the Au substrate. The SP resonant behaviors of the different tip apex sizes are calculated and the spatial distribution of local field enhancements are visualized by the FDTD simulations. Different optical intensity increasing tendencies of optical enhancements (Raman and PL) are observed and analyzed. The enhanced Raman intensity rapidly growing tendency results mainly from the concentrated near fields in the nanogap of decreasing volumes. The FDTD simulations exhibit good agreement with the experimental data of Raman scattering based on the $|E|^4$-approximation. In addition, the sequence of simulations visualizes the hot spot in the tip-surface configuration and quantifies the moving range of the sample. This work provides quantitative analysis in the tip-surface configuration. The strong local field created with different geometries may be ultilized in more SERS or TERS systems and may advance the sensing technique.

Chapter 4
Tip-Enhanced Optical Imaging with Anticorrelated Topography

Optical imaging techniques considerably facilitate the elaborate study of biological and chemical systems. In particular, Raman imaging techniques have been greatly improved and widely applied[221-226], which created opportunities for noninvasive imaging of biological samples. Applying a Raman tag as a narrow-band spectroscopic fingerprint helps identification of different molecules[227 228] in microscopy. However, these techniques are subjected to the diffraction limit[2] in the optical microscope. Tip-enhanced Raman scattering (TERS) with a single hot spot in the proximity of a metallic scanning probe enhances the sensitivity and optical spatial resolution of the microscope to unprecedented levels.

An early demonstration of spatial resolution is done by Hartschuh *et al.* with the use of single-wall carbon nanotubes (SWCNTs). They reported ~25 nm in the tip-enhanced Raman scattering (TERS) image[229]. Steidtner *et al.* established the first home-built TERS in ultra-high vacuum (UHV) conditions[230] and claimed a lateral resolution of 15 nm[231]. More recently, many improvements as sub-nanometer resolution[58] using STM in ultra-high vacuum (UHV) condition and sub-2 nm in the ambient[232] step further into nanoscale chemical imaging. The state-of-the-art technique under the same condition had successfully achieved Ångstrom-scale lateral resolution[73, 233]. The high optical resolution can offer more insights into fundamental interactions between molecules and substrate[233, 234].

The enhancement mechanisms underlying TERS images with fabulous resolution in these works have not yet been well-established. The SPM using the shear-force control regulates the tip-sample distance of a few nanometers. Its corresponding tip-enhanced (TE) optical imaging with an optical spatial resolution of ~15 nm or sub-15 nm [77, 158, 235-239] still requires optimization. To discuss the underlying mechanisms of the spatial TE optical enhancements is fundamental to optical microscopy. Here, we use the home-built confocal setup combined with the shear-force feedback[77, 235-237, 240] to explore optical signals from the plasmonic gap using a monolayered CuPc film. Electrodynamics simulations in the FDTD scheme according to our experimental conditions are performed. The local field enhancement plays the main role in TE optical imaging. The spatial variation in the TE optical images is compared with FDTD simulations.

4.1 Optical Spectra at Positions of Varied Film Thickness

Combining scanning probe microscope and optical microscope (see Figure 1.3), we can perform simultaneous scan of the tip-enhanced (TE) optical and the topographic images as previously detailed described in Chapter 1. The tip-sample distance is maintained as a few nanometers by shear-force feedback control. The feedback signals are realized in sample movement by the 3-axis piezoelectric scanner (see Figure 1.4).

In Figure 4.2, a simultaneous image scan of $2\ \mu m \times 2\ \mu$m is performed, which produces a tip-enhanced (TE) optical image as Figure 4.2 (a) and a topographic image as Figure 4.2 (b). Evidently, the images of Figure 4.2 (a) and (b) present a correlation between each other. The optical contrast is observable with 'bright' and 'dark' areas circled and semi-circled with white dashed lines in Figure 4.2 (a), which are correlated to the height of the 'low' and the 'high' areas in Figure 4.2 (b). Eight point spectra are taken in the optical and the topographic images. P1 denotes the position at '1', and P2 denotes the position at '2' in the images and so on. For the 'high' area, the height differences of the molecule film at point 5 (P5) to point 7 (P7) are about 27 nm. The height at P8 is about 5 nm with respect to other smooth areas. For the 'low' area, the height differences at P1-4 are less than 5 nm. Due to the topographically 'high' area, corresponding optical signals are weakened ('dark'),

while in the ‘low’ area, the overall optical signals are enhanced. Figure 4.2 (d) shows inverse correlated optical and topographic height with the definitions of ‘bright’ (‘low’), ‘dark’ (‘high’).

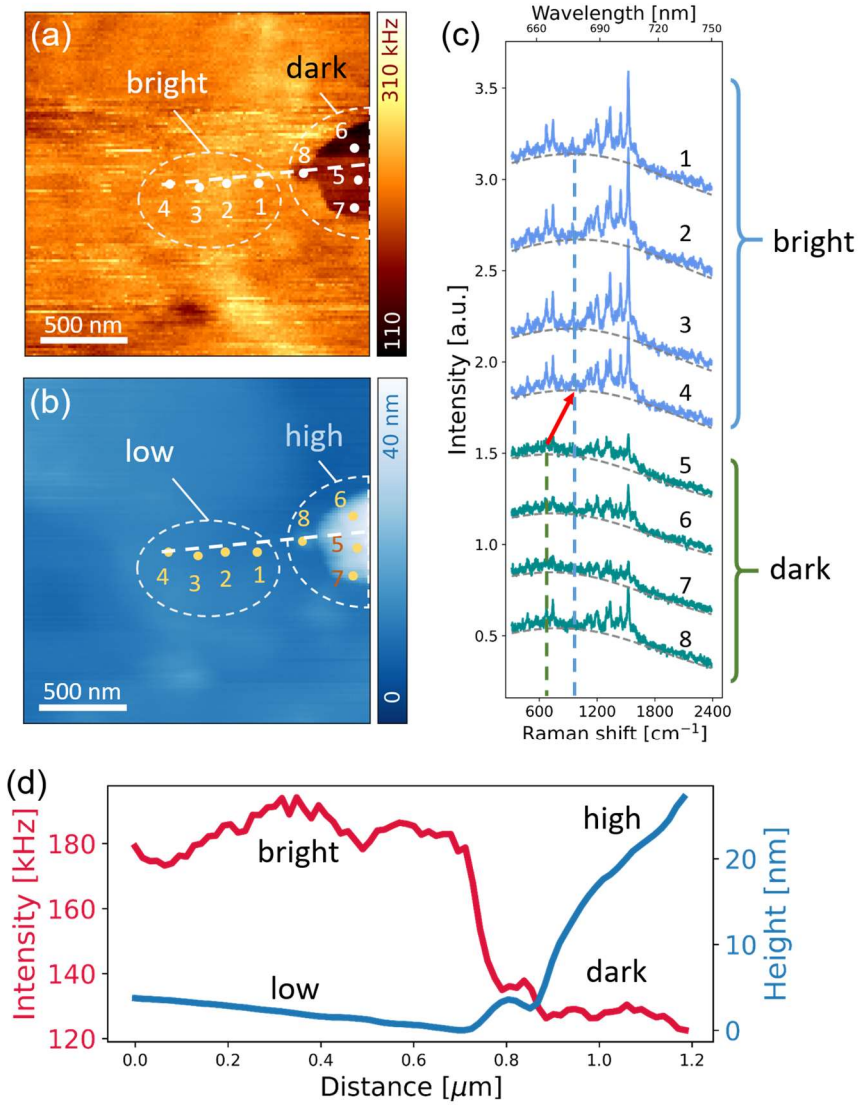

Figure 4.1 Simultaneous image scans of (a) tip-enhanced optical image (b) topographic image (c) Optical spectra of ‘dark’ (‘high’ in (b)) positions (P5-8) and ‘bright’ (‘low’ in (b)) positions (P1-4) according to (a) and (b). Voigt model fitting is performed for each spectrum, which is shown as gray dashed lines. The PL peak of the ‘dark’ (’bright’) spectra is highlighted by a green (blue) dashed line. The red arrow shows the redshift of the PL peak. (d) 1D profiles of optical and topographic height, which corresponds to the white dashed line in (a) (b)

The corresponding optical spectra of 'bright' and 'dark' are presented respectively in Figure 4.1 (c). There are a few points we can observe. First, it's observed that peaks of Au PL of spectra at P1-4 shift from 664.7 nm (dark) to 677.5 nm at P5-8 (bright). Second, the intensities of both the PL and Raman signals of 'bright' positions (P1-4) are greater than that of 'dark' positions (P5-8).

It is known that Au PL predominates the overall optical signals[77], so we can infer that the coupling between Au tip and Au substrate plays a crucial role in the overall optical signals. The optical and topographic images are obtained by a raster scan of the sample pixel by pixel. The sample will retract instantly as the molecular film is thicker according to the shear-force feedback control. The coupling strength is stronger as the Au is closer to the Au substrate, and the corresponding PL intensity is stronger and redshifted as well. Meanwhile, the Raman intensity is also influenced by the coupling between Au tip-Au substrate. All these clues show that the larger the tip-substrate distance is, the weaker the optical intensities (Au PL and Raman) are.

4.2 Tip-Enhanced Optical Images with Spectral Mapping

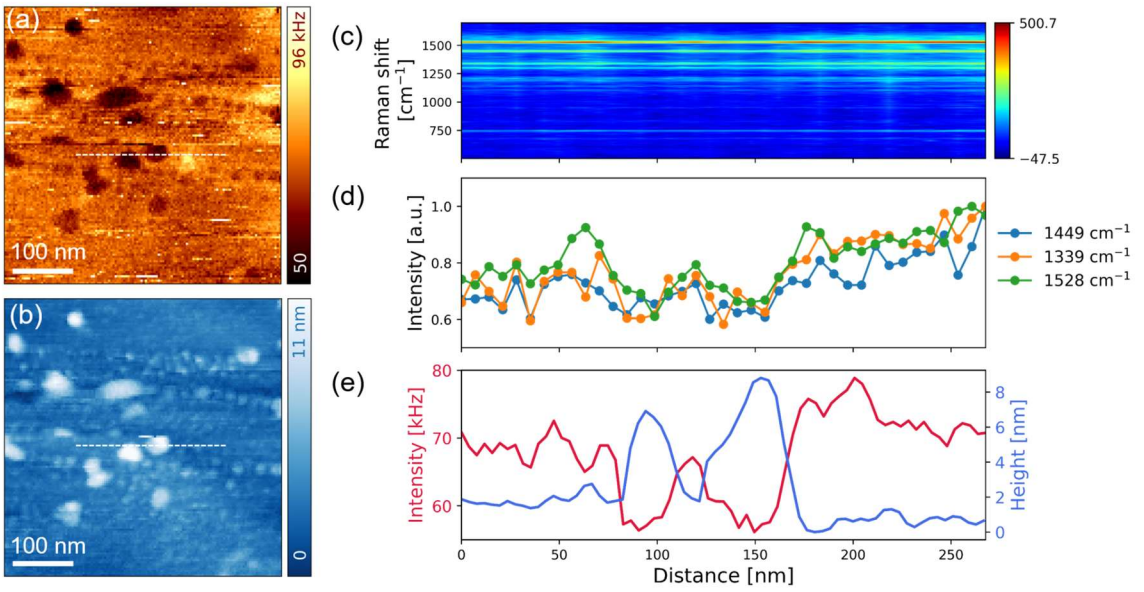

Figure 4.2 Simultaneous image scans of (a) tip-enhanced optical image (b) topographic image with optical spectra. (c) Raman spectra are collected along the white dashed line in (a) and (b). (d) Selected Raman modes as a function of distance. (e) Optical intensity $I_{opt}(x)$ and topographic height profiles $H(x)$ from (a) and (b) images

We further investigate the spatial variation of the tip-enhanced (TE) optical signals by image scans shown in Figure 4.2. The TE optical $I_{Opt}(x, y)$ and topographic $H(x, y)$ images of $500\ nm \times 500\ nm$ are performed. The correlated spectral mapping along a line of 265 nm is carried out along the white dashed lines in Figure 4.2 (a) (b). The optical intensity results from the intensities of Raman scattering and PL, and their relation can be written as $I_{Opt}(x, y) = I_{Raman}(x, y) + I_{PL}(x, y)$. Their corresponding spatial variation of the Raman and three selected Raman modes along the line are plotted in Figure 4.2 (c) and (d). Two film islands are clearly resolved shown as dips along the line for in Raman and PL signals. The 1D cross-section line shows one object feature of ~22 nm and ~42 nm in width.

It can be observed that the features in the optical image (Figure 4.2 (a)) are inversely correlated to the topographic image (Figure 4.2 (b)). The 1D-section lines in Figure 4.2 (a)

and (b) are plotted in Figure 4.2 (e). In Figure 4.2 (e), the optical signals $I_{Opt}(x)$ show a similar variation as Raman $I_{Raman}(x)$ along the section line.

Interestingly, the optical signals $I_{Opt}(x,y)$ drop while their topographic heights $H(x,y)$ increase. The left object is ~5.1 nm high and the right one is ~8.1 nm with respect to the smooth surface of the left-hand and the right-hand side. The optical intensity at the position of the left object drops ~16.7% of the intensity at the left smooth side while at the right object drops ~22.4% of the intensity at the right-hand smooth side. The results are consistent with our hypothesis in the preceding section.

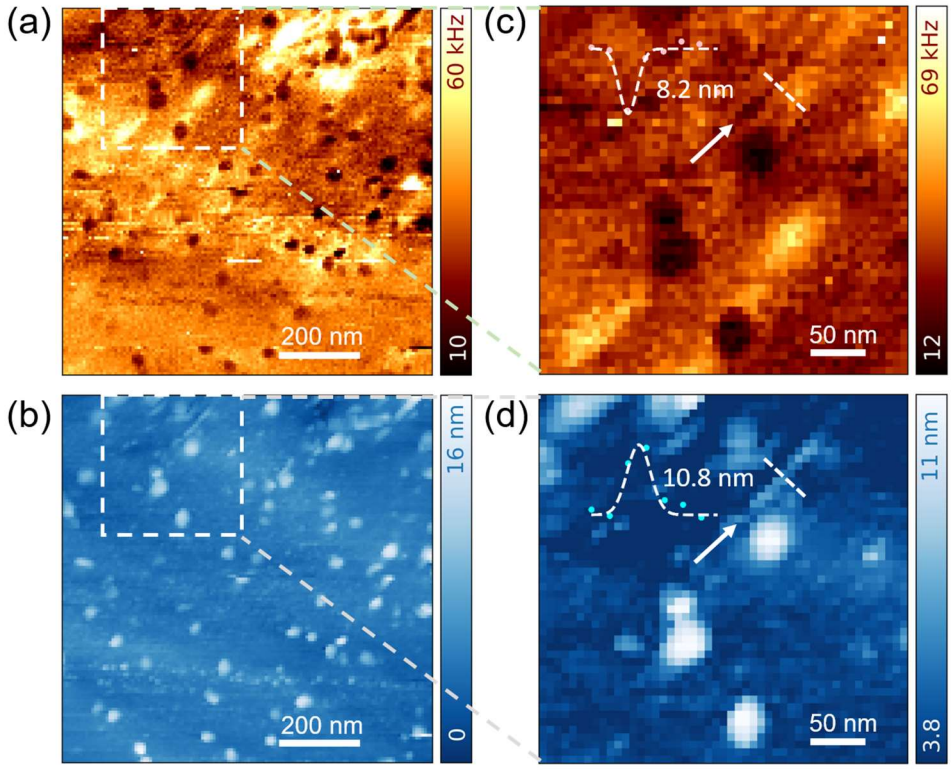

Figure 4.3 Simultaneous image scan of (a) tip-enhanced optical image (b) topographic image. (c) and (d) are the selected small area corresponds to the white dashed boxes in (a) and (b). The white arrows point towards the 1D features in optical and topographic images. The oblique white dashed lines in (c) and (d) are shown as an inset in (c) and (d) fitted by Gaussians.

Similarly, another image scan of a larger area of 1 μm × 1 μm is performed and shown in Figure 4.3 (a)-(d). It can be clearly seen that $I_{Opt}(x,y)$ and $H(x,y)$ show an inverse correlation to each other in Figure 4.3 (c)-(d).

The intensity $I_{Raman}(x)$ is correlated to $I_{PL}(x)$ in the spatial domain, while the difference emerges between this intensity variation ($I_{Raman}(x)$ and $I_{PL}(x)$) and overall optical signals $I_{Opt}(x)$ along the line in the image. This implies that either the sample- or the tip-drifting issue might occur during the line scan. Another possible reason is the handshaking delay between the scanning probe microscope (SPM) controller and the spectrometer.

Figure 4.3 (c) and (d) are the tip-enhanced optical and the topographic image of selected small areas dashed squared in Figure 4.3 (a) and (b). The anticorrelation is clear observable even in the smaller area of $330\ nm \times\ 330\ nm$. The Gaussian approximative point spread function (PSF)[241, 242] is applied to determine the width of the optical response from an object. The finest optical feature of the film in the small area is ~8.2 nm in width (dip) along the oblique dashed line in Figure 4.3 (c) with topographic feature ~ 10.8 nm in width (peak) along the same oblique dashed line in Figure 4.3 (d) by Gaussian fitting. The insets in Figure 4.3 (c) and (d) are data with fitting curves shown as white dashed lines.

4.3 Discussion

The correlation between TE optical image and topography is presented in the double-tip configuration (Au tip-Au ND), which has been presented in Chapter 2. In contrary to this correlation, here we observe that the TE optical signal drops as the film thickness (topographic height) increases with inverse nice correlation. TE optical signals with gap-dependence are discussed in Chapter 3.

The working principle of the shear-force feedback is a loop using the phase shift as feedback signals from the quartz tuning fork. In an attempt to keep this phase shift a constant during each 1D or 2D raster scan, the SPM controller regulates the tip-sample distance as a constant. However, the medium between Au-tip and Au substrate is not uniform in this case. Now we turn to discuss the field enhancement as a function of film

thickness.

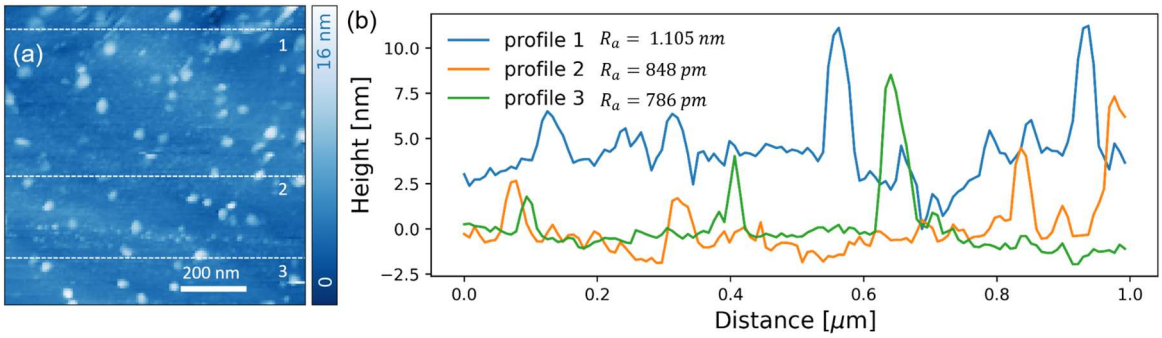

Figure 4.4 (a) Topography image replotted from Figure 4.4 (b) with 3 profiles as white dashed lines. (b) 3 profiles in white dashed lines in (a)

Topography images provide us with the morphology of the film surface. It can be seen that the morphology is non-uniform evidently according to images from Figure 4.2-4.3. Reconsidering the topographic image of Figure 4.3 (b), the surface roughness R_a (arithmetic average value[243]) along three different lines of 1 μm in Figure 4.4 (b) are calculated as $R_a^{profile\ 1,2,3} = 1.105\ nm\ , 848\ pm, 786\ pm$ respectively. Hence, it's observed that the overall molecular film does not possess too many small protrusions of large curvature. The small curvature of the film along the wide scan range can be viewed as a relatively flat film of varied thickness, which is considered in the following simulation.

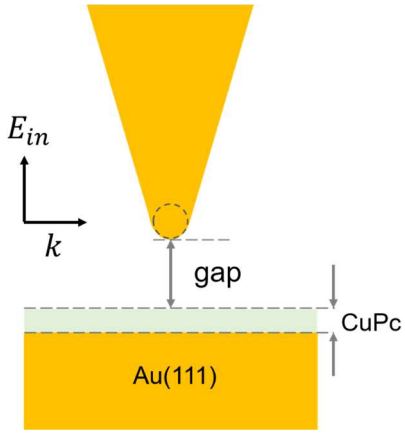

Figure 4.5 Schematic diagram of the tip-enhanced configuration in FDTD simulations. The 'gap' is defined as the tip-sample distance, which is a constant in the scan by shear-force feedback control. CuPc film of thickness d, which is a variable in our experiments. Au(111) is the substrate.

Numerical FDTD simulations are performed using Meep[125] to understand the inverse correlation of optical and topographic images. The FDTD simulation environments according to our experimental conditions are schematically plotted as Figure 4.5. The 'gap' is defined as the tip-sample distance, which is set to be a constant in each simulation case. The CuPc film of variable thickness d, which depends on the lateral distance x. And this is assumed to influence the TE optical signals from Au. The relative permittivity of Au is derived from the Drude-Lorentz model in Meep[125]. The relative permittivity of CuPc film[244] is reported as $\epsilon = 2.2$. This parameter of the CuPc object is considered a constant for all wavelengths in the following simulations. The source is a p-polarized plane wave, which propagates from the left side of the simulation cell. The incoming field E_{in} can be obtained by time-stepping without introducing the geometry. The local field E_{loc} are obtained with sufficiently long time-stepping. After sweeping a wide range of frequency (wavelengths), the frequency- (wavelength-) dependent field enhancements $|E_{loc}/E_{in}|$ can be thus derived.

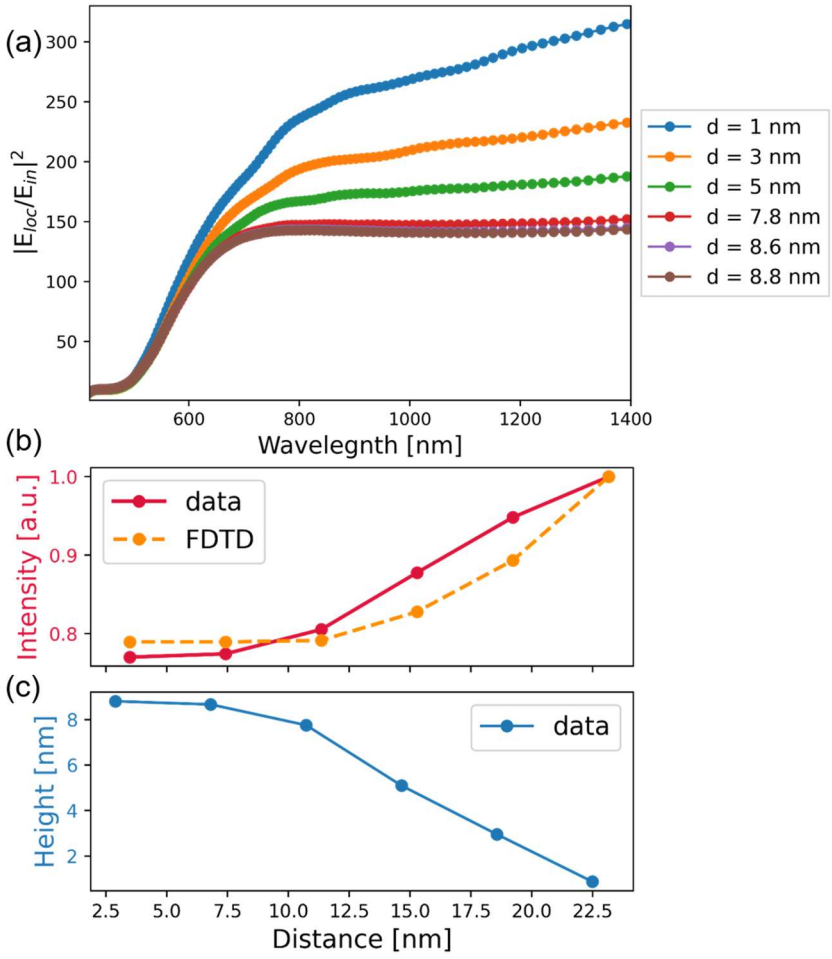

Figure 4.6 (a) Calculated field enhancement $|E_{loc}/E_{in}|^2$ varied as a function of film thickness d (b) Comparision of experimental data with FDTD simulations.

According to the simulation results in Figure 4.6 (a), as the film thickness d increases, the overall responses of wavelength-dependent field intensity enhancement $|E_{loc}/E_{in}|^2$ decreases. This agrees with our assumptions in the previous section. Notably, there is no observable resonance in the visible range for smaller d, and $|E_{loc}/E_{in}|^2$ at longer wavelengths exhibits a more dramatic increase. A very broad resonance can be observed at 800 nm with d = 8.8 nm. This wide plateau in the field enhancements resemble the calculations of simulations of tip-enhanced Raman excitation spectroscopy (TERES)[245], and this work explains that the feature of wide plateau stems from higher-order plasmonic modes sustained in the tip-substrate configuration. It can be observed that these overall increasing trends are moderate compared with the gap-dependent $|E_{loc}/E_{in}|^2$ obtained in

Chapter 3. Figure 4.6 (b) (c) reproduces the data from Figure 4.2 (e), whose optical intensity is compared with the FDTD results. $|E_{loc}/E_{in}|^2$ as a function of d according to different topographic heights shows the increasing optical response as the film height decreases. After normalizing the maximal optical intensity to unity, the optical intensity drops $\sim 23\%$ and $|E_{loc}/E_{in}|^2$ drops $\sim 21.1\%$. The CuPc film acts as a spacer to increase or decrease the influence from the gap mode of Au tip-Au substrate. Now it is clear that the optical intensity variation stems mainly from the gap mode induced in the Au tip-Au(111). The inverse correlation between the optical intensity and the topographic height is quantitatively compared with the FDTD simulations. Our previous claim of the inverse correlation is now validated through the experiments and the corresponding numerical simulations.

As we have learned from the simulations in Chapter 3, the geometries of the Au tips tune the surface plasmon resonances (SPRs). The FDTD simulations can be further extended with variable parameters of the Au tip in the future, which can help design TE optical images for a molecular film with better optical contrast.

4.4 Conclusion

We carry out measurements of TE optical and topographic images of the molecular thin film from $2\ \mu m \times 2\ \mu m$ scan range to $500\ nm \times 500\ nm$. The optical spectra show a redshift in PL peaks in the area of thinner film and higher Raman and PL intensities than the area of thicker film, since the tip-sample distance (or gap size) is assumed to be a constant over all the image scans in the shear-force scheme. The varied film thickness over the surface is assumed to affect the optical intensity, which results in an inverse correlation between TE optical (Raman and PL) and topographic images. It is observed that the finest optical dip feature of ~8.2 nm in width corresponds the topographic height ~10 nm in width in the small scan range. We also systematically compared the experimental data with FDTD simulations. The optical intensity increase is more moderate compared with the gap-dependent measurements for gap < 10 nm. The simulations show a similar trend as the optical intensity. This study improves the understanding of the correlation between TE

optical and topographic images. This may help the design of TERS imaging of molecular thin films by the shear-force feedback in the ambient to achieve better optical resolution.

Chapter 5
Radiation of the Plasmonic Gap

Antennas can transmit and receive electromagnetic waves for communications in modern life especially in radio wave and microwave frequency range. Fabricating noble-metal antennas at the nanometer scale can convert free propagating optical radiation into localized energy and vice versa, which can significantly enhance nanoscale light-matter interactions and serve as optical antennas[246, 247]. This character brings in multitudinous applications such as nanoscale microscopy[248-250], vibrational spectroscopy[251], single-molecule imaging with antennas[252, 253], optical nanocircuitry[254-256], plasmonic sensors[257, 258], visualization of the density of states (DOSs)[259] and even optical nonlinearities[260]. The design and optimization of an optical antenna are still ongoing and the potential of optical antennas is still not fully discovered yet. In recent years, there has been a surge of interest in back-focal-plane (BFP) imaging[103, 104, 211, 261-272] (also called k-space imaging[268], emission pattern imaging[273] or Fourier-plane imaging[264, 274]), which has been widely applied for imaging directionality of optical signals. This technique enables one to discover fundamental emission properties of optical antennas.

Noble-metal probes as optical antennas can perform high spatial resolution and sensitivity by the tip-enhanced near-field optical microscope. The fundamentals have been already mentioned in the preceding chapters. While different research groups take advantage of different configurations of scanning probe microscopes from one another. The most commonly used configurations for illumination of the probe are shown in the

reviews[38, 275], which are on-axis bottom illumination through objectives, side-illumination and on- and off-axis parabolic mirrors (PMs). We now limit the samples to the opaque ones, which can be observed only by side-illumination and on- or off-axis parabolic mirror configurations. The geometry by side-illumination requires a long working range as objectives of $NA{\sim}0.6$ to collect limited emission as well as the off-axis PM. The on-axis PM configuration applies the PM of high $NA{\sim}0.998$ to collect more emission photons than common objectives and free from chromatic aberration. Collection efficiency is crucial to tip-enhanced optical spectroscopy. Moreover, the directionality of emission from the gap mode is changed as the gap size varies, which makes the on-axis PM configuration powerful to image directionality.

Though the techniques of the tip-enhanced optical measurements are widely applied as discussed in the preceding chapters. The mechanisms in the radiation of the Au tip remain unclear. To unravel the radiation mechanisms, here we perform BFP imaging of emission from Au tip and Au tip in the proximity of Au (111) substrate by the PM. Time-dependent FDTD simulations are calculated for understanding antenna properties and their mechanisms of radiation for the tip-enhanced (TE) optical enhancement. With these results and understandings from the simulations, better configurations or designs of the probe for the tip-enhanced optical measurements for high collecting efficiency can be further developed.

5.1 Back-Focal-Plane Imaging with the Parabolic Mirror

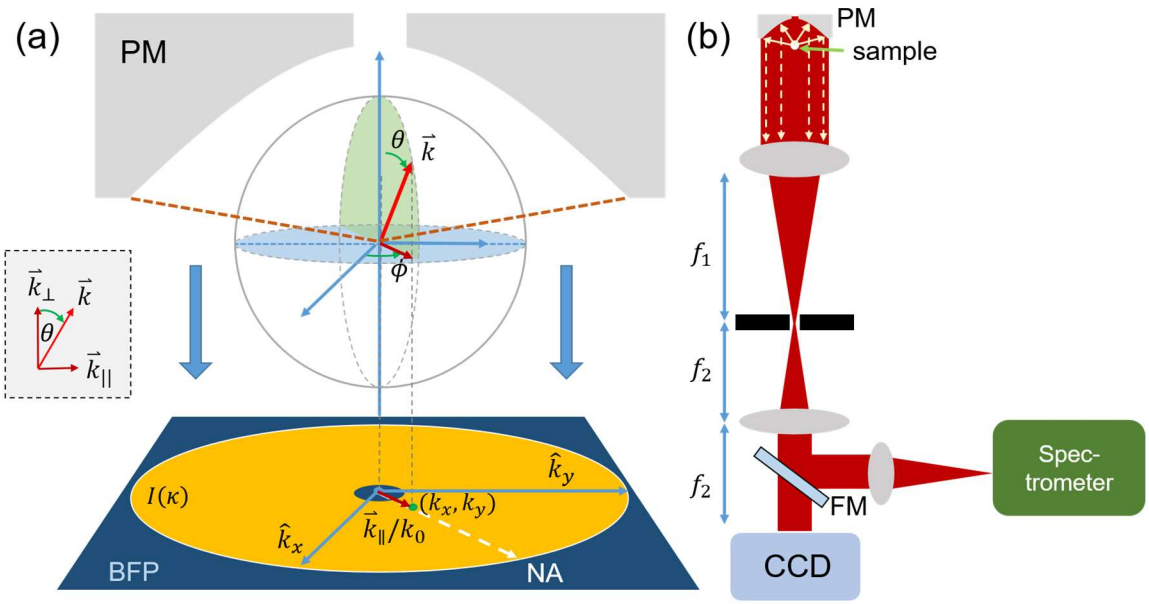

Figure 5.1 (a) Schematic of the geometry of emission waves. The wave vector of each emission wave is denoted as $\vec{k}$ with azimuthal angle ϕ and polar angle θ. The inset is the vector projection for the wave-vector $\vec{k}$. (b) Schematic of the experimental setup of back-focal-plane (BFP) imaging and confocal measurements for emission detection. The emission signals are collected by the PM and further directed into a telescope with two lenses (focal lengths of f_1 and f_2). A flipping mirror (FM) can direct into a spectrometer for confocal measurements.

5.1.1 Back-Focal-Plane Principle

The Fraunhofer and the Fresnel approximations are used for calculating diffracted fields in different spatial regions[2]. Normally, Fraunhofer diffraction requires a large distance between the source and the observation plane[2, 276]. Born and Wolf had provided the derivation[2] in detail, which is not reproduced here. If a positive lens (or Fourier lens[264]) is placed adequately between the observer and the aperture, the Fraunhofer diffraction can be realized[276]. The mathematical form of the Fraunhofer diffraction field coincides with that of the Fourier transform[276]. Fourier-plane imaging is also known as back-focal-plane (BFP) imaging[262, 264, 276].

Here, we use the on-axis parabolic mirror (PM) for excitation and collection. The corresponding back-focal plane is illustrated in Figure 5.1 (a). Let us consider an emission

wave propagating in a direction of a wave-vector $\vec{k}$ (red arrow) with a polar angle θ and an azimuthal angle ϕ as shown in Figure 5.1 (a). The total power collected by the parabolic mirror is radiated at a solid angle (steradians or sr)

$$\Delta\Omega_{PM} = \int d\Omega = \int_0^{2\pi} \int_0^{\theta_{max}} \sin\theta d\theta d\phi \cong 1.894\pi \qquad (5\text{-}1)$$

where $\theta_{max} = \sin^{-1} NA$. Note that $\Delta\Omega_{PM}$ approaches almost half of the entire solid angle of a unit sphere, which collects almost all back-scattered photons.

The thick blue arrows pointing downward represent the propagation direction of emission, which are parallel to the optical axis. The inset of Figure 5.1 (a) shows the vector projection of the $\vec{k}$ onto the BFP and perpendicular to the BPF, which are denoted as $\vec{k}_{||}$ and $\vec{k}_{\perp}$. The BFP (navy) with an effective collecting area (yellow) for emission is shown in Figure 5.1 (a). The effective collecting area for emission is limited by the maximal solid angle of the PM as $k_0^2\Delta\Omega_{PM}$ such that $\left(\frac{k_x}{k_0}\right)^2 + \left(\frac{k_y}{k_0}\right)^2 = \left(\frac{k_{\parallel}}{k_0}\right)^2 \leq NA^2$ where $k_0 = |\vec{k}|$. The polar angle θ is determined by $\tan\theta = k_{\parallel}/k_{\perp}$ or $\sin\theta = k_{\parallel}/k_0$. The value range of θ is $0 < |\theta| < \theta_{max}$ with $\theta_{max} = \sin^{-1} NA$. The azimuthal angle is $\phi = \tan^{-1}(k_y/k_x)$. The value range of ϕ from 0 to $\pm\pi$ radians (or $\pm 180°$). The directions of $\hat{k}_x$ and $\hat{k}_y$ are represented by $\phi = 0$ and $\phi = \pi/2$ radians (or 90°) respectively. Consequently, $I(\theta)$, and $I(\phi)$ can be derived from the BFP images $I\left(\frac{k_x}{k_0}, \frac{k_y}{k_0}\right)$. For simplicity, $I\left(\frac{k_x}{k_0}, \frac{k_y}{k_0}\right)$ is denoted as $I(\kappa)$ in the remainder of the chapter.

5.1.3 The Experimental Setup for Back-Focal-Plane Imaging

The laser of 636 nm is applied as the excitation wavelength with radial polarization. Here, we only illustrate the experimental setup for the detection. Figure 5.1 (b) shows BFP imaging of emission detection, which is composed of a telescope of two lenses. The focal lengths of the first and the second lenses in the telescope are denoted as f_1 and f_2 respectively. The liquid N_2 cooled CCD is placed at the position of f_2 after the second lens

of f_2 in the telescope. A flip mirror (FM) is used to turn emission to APD and spectrometer for confocal measurements. Optical signals of elastic scatterings can be collected without any filters. PL signals can be collected by placing two notch filters (NFs) in front of the CCD.

The Au tip can be brought in the proximity of the Au substrate with shear-force feedback control. The shear-force feedback is realized by the 3-axis piezoelectric scanner. The details of the scanning probe microscope (SPM) are stated in Section 1.4.3 (Figure 1.4).

5.2 Radiation Patterns of a Au Tip

5.2.1 Elastic Scattering and PL

The experimental radiation patterns $I(\kappa)$ are directly obtained by BFP imaging. Based upon the principle and the experimental setup, the corresponding $I(\phi)$ and $I(\theta)$ can be derived respectively. I_L and I_{PL} denote the intensity of elastic scattering and PL. The radiation patterns $I_L(\kappa)$ and $I_{PL}(\kappa)$ show similar directionalities. The BFP images (Figure 5.2 (a) and (b)) show dark areas in the middle since the scattered or emitted photons are blocked by the sample and single-arm of the sample holder. This can be observed in the next figure with an illustration.

$I_L(\phi)$ and $I_{PL}(\phi)$ both show a preferential directionality in the range $\Delta\phi = 0{\sim}135°$ as shown in Figure 5.2 (c) (d). Their directionalities are closely correlated for $\Delta\Omega_{\mathrm{PM}}(\theta,\phi)$. The anisotropic radiation patterns are commonly observed. This phenomenon will be discussed in Section 5.4.

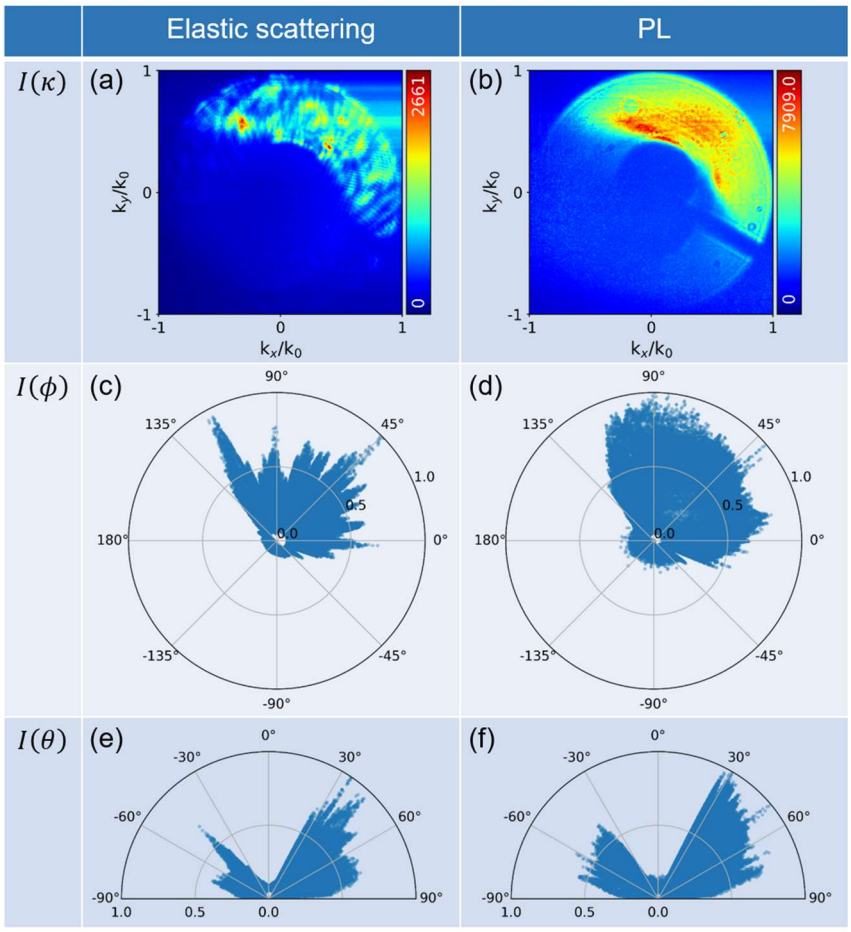

Figure 5.2 BFP patterns $I(\kappa)$ of (a) elastic scattering intensity and (b) PL intensity from the Au tip. (c), (d) are $I(\phi)$ and (e), (f) are $I(\theta)$, which are derived from the radiation patterns $I(\kappa)$ of (a), (b). The integration time for elastic scattering is 1 sec and for PL is 10 secs. The excitation power for BFP images for elastic scattering is $\sim 2\ nW$ and for PL is $\sim 200\ \mu W$. (These experimental conditions remain the same for all the following measurements)

5.2.2 Position of the Au Tip

A confocal image of the Au tip helps one to determine the position of the tip. Once a diffraction-limited pattern is observed provided that the tip apex is smaller than the diffraction limit, the optimal position of the Au tip is defined accordingly. The confocal image of the Au tip is shown in Figure 5.3 (a), which shows the highest intensity at the central lobe and decreases to the first dark fringe and the side lobes appear with weaker intensity.

The sample with the sample holder and the quartz tuning fork restrict the overall detection area in the back-focal plane as shown in Figure 5.3 (b). (see Figure 1.4 for more details about the SPM setup) These elements limit the solid angle of the PM for collection. Part of the emission will be blocked by the sample holder, which causes a limited detection range of ϕ and partial range of θ. The sample and the quartz tuning fork limit the emission with $\sin^{-1} NA > |\theta| > \theta_0 \neq 0$. The calculation for $\Delta\Omega_{PM}$ in the preceding section will need further modifications with these considerations for higher accuracy.

The radiation patterns $I(\kappa)$ of elastic scattering at three positions of the "central lobe", the "right side lobe", the "left side lobe" are collected and shown in Figure 5.3 (c)-(e). The corresponding $I(\phi)$ and $I(\theta)$ are derived and shown in Figure 5.3 (f)-(h) and (i)-(k) respectively. The anisotropic radiation patterns show an effect from the geometry of the Au tip according to the confocal image. The diffraction-limited image of the Au tip is slightly distorted in Figure 5.3 (a), which is assumed to result from the shape of the Au tip apex being elongated in the y-direction or some irregular protrusions on top of the Au tip. Here, we can infer that the positioning of the Au tip in the optical field is critical in experiments. The position of the Au tip influences not only its intensity but also its emission directionality.

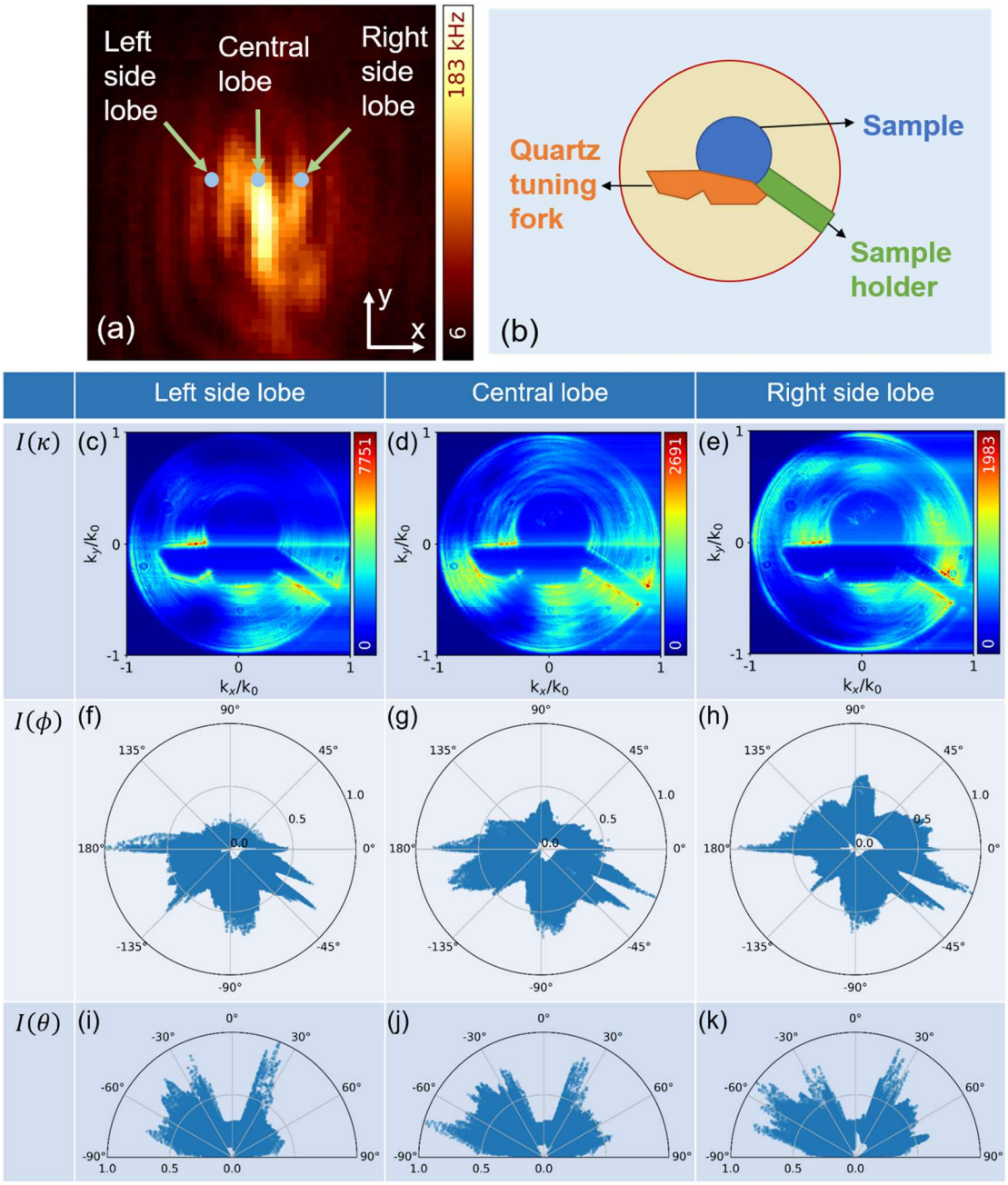

Figure 5.3 (a) Confocal image of the Au tip, which shows the central main lobe and the side lobes (left and right). (b) Schematic of the BFP images with the effective collection area (yellow). Sample holder (green) sample (blue) and quartz tuning fork (orange) block part of BFP detection and produce dark areas in the BFP images. (c)-(e) are radiation patterns of different positions at the 'left side lobe', the 'central lobe' and the 'right side lobe' shown as $I(\kappa)$. (f)-(h) are the corresponding $I(\phi)$ and (i)-(k) are the corresponding $I(\theta)$, which are derived from the radiation patterns (c)-(e).

5.3 Radiation Patterns of Au Tips in the Proximity of Au Substrate

5.3.1 Morphology of Au Tips Characterized by SEM

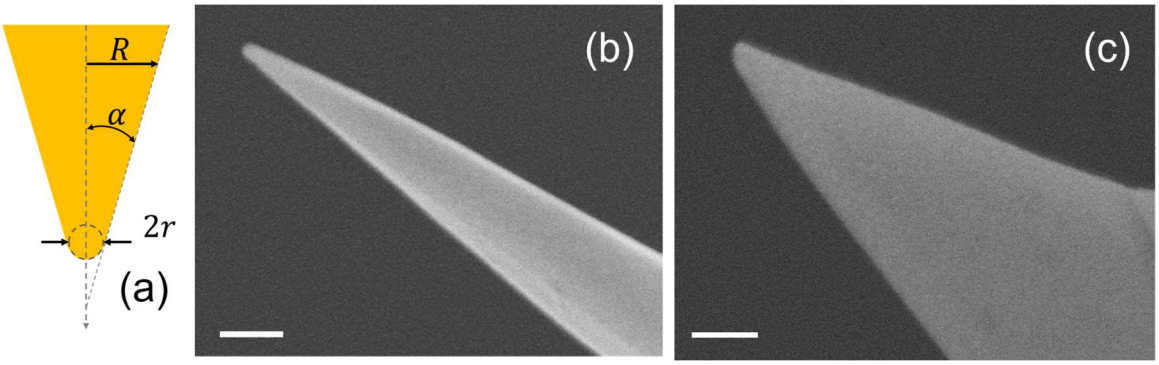

Figure 5.4 (a) Schematic of a Au tip with taper half-angle α and apex diameter $2r$. The conical taper geometry is a cylindrical waveguide of a varied local radius R. SEM images of Au tips (b) with apex diameter $2r = 25$ nm and taper angle $\alpha = 6.25°$ (c) with apex diameter of $2r = 36$ nm and taper angle $\alpha = 16°$. The scale bars inside images of (b) (c) are both 100 nm.

The Au tips are made by electrochemical etching from bulk Au wires, whose morphology is shown in SEM images Figure 5.4 (b), (c). The geometry of each Au tip is viewed as a conical taper with a radius of curvature (ROC) r (diameter $2r$) of the apex and taper half-angle α according to the schematic in Figure 5.4 (a). The conical taper geometry is a cylindrical waveguide of a varied local radius R. The dimensions of the Au tips are estimated as apex diameter $2r = 25$ nm and $\alpha = 6.25°$ and the other one with $2r = 36$ nm and $\alpha = 16°$ according to the SEM images, which are named as Au tip 1 and Au tip 2 respectively in the following paragraphs.

5.3.2 Radiation Patterns with Optical Spectra

Optical spectra of Au tip 1 and Au tip 1 in the proximity of Au substrate (Au tip 1-Au) are acquired and shown in Figure 5.5 (a) (b). Figure 5.5 (c) and (d) show optical spectra of Au tip 2 and Au tip 2-Au. Voigt model fittings are performed in the spectra shown as navy dashed curves in Figure 5.5 (a)-(d). The peak of the Au tip spectrum is 648 nm and is red-shifted to 652 nm in Au-Au. The feedback signal (phase shift) drops from $0°$ to $-4°$ as the Au tip is placed in the proximity of the Au substrate. The gap size is estimated as 3 nm with a phase shift of $-4°$. The PL intensity of Au-Au increases by comparison with the Au tip alone. The optical spectra of Au tip 2 and Au tip 2-Au are similar in the red-shifted peaks and the overall spectral shapes to those of Au tip 1 and Au tip 1-Au. These behaviors of optical spectra are consistent with the results shown in Chapter 3.

The emission patterns $I(\kappa)$ are obtained directly in the experiments and shown in Figure 5.5 (e)-(h), which correspond to the spectra in Figure 5.5 (a)-(d). The intensities $I(\theta)$ and $I(\phi)$ are derived according to $I(\kappa)$ and shown in Figure 5.5 (i)-(l) and (m)-(p) respectively. For clear definitions, $I_{Au(1,2)}(\kappa)$ represent the emission patterns of Au tip 1 or Au tip 2, and $I_{Au(1,2)-Au}(\kappa)$ denote the emission patterns of Au tip 1-Au substrate or Au tip 2-Au substrate. The notation is also applied to the angular distributions $I(\theta)$ and θ. Two different ranges of θ are defined as $\Delta\theta_{\pm} = 0°\sim \pm 90°$, and the corresponding $I(\Delta\theta_{\pm})$ denote the intensities radiated in $\Delta\theta_{\pm}$. This notation is also applied in the remainder of the chapter.

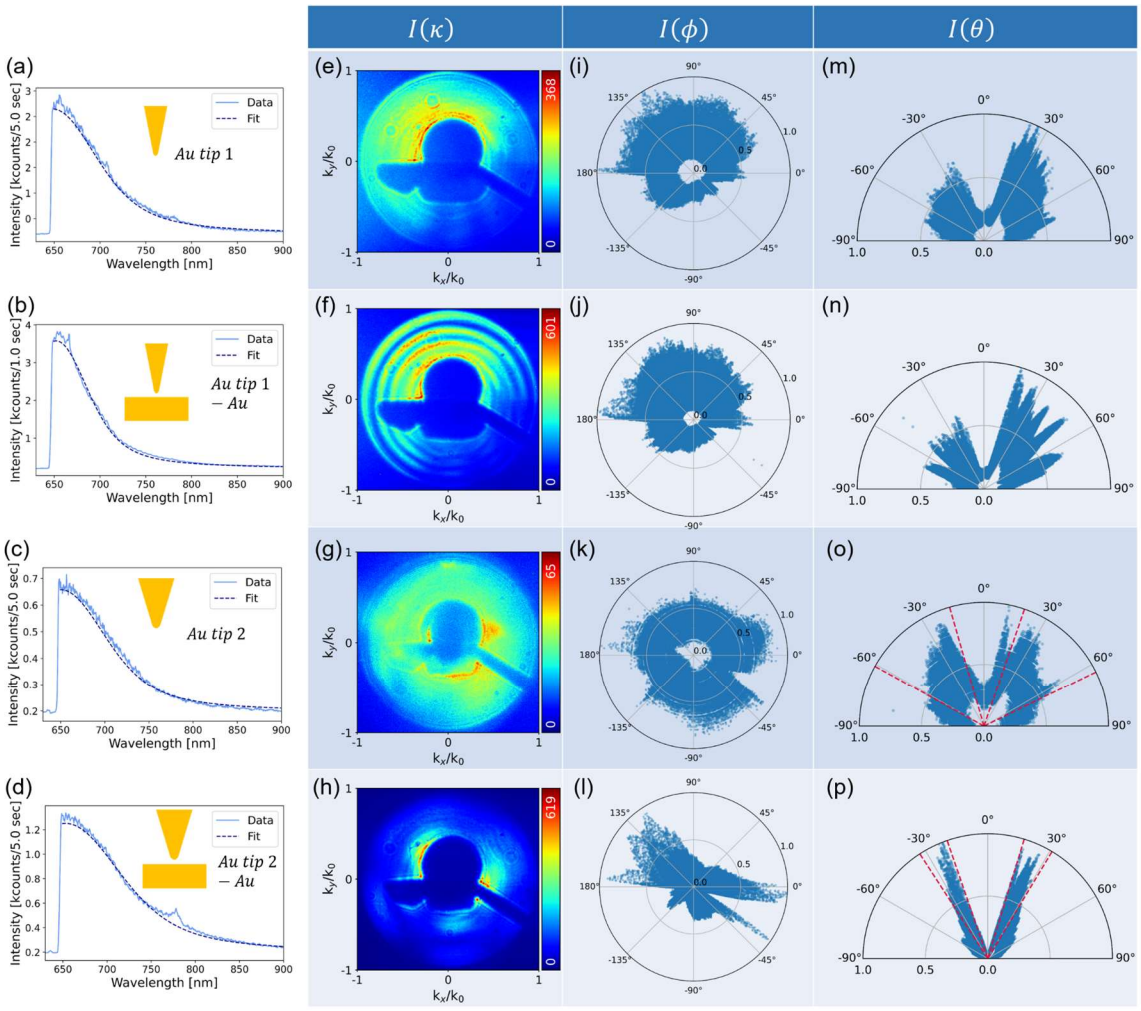

Figure 5.5 (a) (b) Optical spectra of Au tip 1 and Au tip 1-Au substrate; (c) (d) optical spectra of Au tip 2 and Au tip 2-Au substrate. Emission patterns $I(\kappa)$ of (e) Au tip 1 (f) Au tip 1-Au substrate (g) Au tip 2 and (h) Au tip 2-Au substrate. The corresponding $I(\phi)$ are (i)-(l) and the $I(\theta)$ are (m)-(p). The beamwidth $\Delta\theta_{BW}$ (intercepted by red lines) is estimated by the half intensity $\sim 0.5 \cdot I_{max}$

Let us compare the emission patterns $I(\kappa)$ of Au tip 1 and Au tip 1-Au substrate first. Multiple fringes can be observed in Figure 5.5 (f) and the corresponding $I(\theta)$ exhibits ten noticeable lobes in $|\theta| \leq 90°$ (see Figure 5.5 (n)). The anisotropic radiation intensity distribution in $\Delta\theta_+$ and $\Delta\theta_-$ can also be observed. Overall, the radiation intensity of Au tip 1 and Au tip 1-Au substrate resemble each other according to both $I(\phi)$ and $I(\theta)$.

Let us turn to the emission patterns $I(\kappa)$ of Au tip 2 and Au tip 2-Au. $I_{Au(2)}(\kappa)$ and $I_{Au(2)-A}(\kappa)$ are shown in Figure 5.5 (g) and (h), which show different directional

behaviors than that of Au tip 1. $I_{Au(2)}(\phi)$ (Figure 5.5 (k)) shows nearly isotropic emission over all angles of ϕ, while $I_{Au(2)-Au}(\phi)$ (Figure 5.5 (l)) shows anisotropic. This is not similar to $I_{Au(2)}(\phi)$ as $I_{Au(1)}(\phi)$ is similar to $I_{Au(1)-Au}(\phi)$. It seems that $I_{Au(2)-Au}(\phi)$ is more directive in ϕ. From another aspect $I(\theta)$ in $\Delta\theta_+$ and $\Delta\theta_-$, it can be evaluated that $I^{max}_{Au(2)}(\Delta\theta_+)/I^{max}_{Au(2)}(\Delta\theta_-)\sim 1/0.85$ and $I^{max}_{Au(2)-Au}(\Delta\theta_+)/I^{max}_{Au(2)-Au}(\Delta\theta_-)\sim 0.9$. We observe more symmetric angular distributions in $I(\theta)$. Let us have a look at Figure 5.5 (h) again. The emission patterns are blocked by some elements that are previously discussed. These elements limit part of the radiation and result in anisotropic $I_{Au(2)-Au}(\phi)$. It is likely that $I_{Au(2)-Au}(\phi)$ turns isotropic as the PM can collect emission from the solid angle $\Delta\Omega_{PM}$ of $0 \leq |\theta| < \sin^{-1} NA$ and $0 \leq \phi < 2\pi$.

Thus, provided that the radiation intensity is ϕ-independent, the directionality of the radiation patterns can be characterized by the half-power beamwidth or the beamwidth $\Delta\theta_{BW}$. The red dashed lines in Figure 5.5 (o) (p) represent guiding lines for estimating beamwidths $\Delta\theta_{Au(2)}$ and $\Delta\theta_{Au(2)-Au}$. $I_{Au(2)}(\theta)$ shows lobes at $\theta = \pm 25°$ with beamwidth $\Delta\theta_{Au(2)} = 41°$. A side lobe of $\theta \cong 15°$can be observed in $I_{Au(2)}(\theta)$ (Figure 5.5 (o)), which is attributed to out-of-focus emission since the overall intensity of emission is weak. The other one, $I_{Au(2)-Au}(\theta)$ shows lobes estimated at $\theta \sim \pm 24°$ (Figure 5.5 (p)) with beamwidth $\Delta\theta_{Au(2)-Au} = 14°$, which is smaller than half of the beamwidth $\Delta\theta_{Au(2)}$. The radiation of Au tip 2-Au shows stronger directionality than Au tip 2 alone. In other words, the gap formed by Au tip 2-Au modifies the radiation.

Notably, $I_{Au(1)-Au}(\kappa)$ and $I_{Au(2)-Au}(\kappa)$ and the corresponding derived $I(\theta)$ and $I(\phi)$ exhibit different directional behaviors once the Au substrate approaches in the vicinity of the Au tip. The geometry and precise alignment of the Au taper could play a role in emission. Though the Au tip is assumed to be aligned perfectly parallel to the optical axis and perpendicular to the Au substrate surface, the Au tip is inevitably tilted with respect to the optical axis in the experiments, whose anisotropic far-field intensities can be found in the FDTD simulations[277]. The more isotropic radiation of $I_{Au(2)}(\kappa)$ is assumed to result from Au tip 2 with a negligible tilted angle with respect to the optical axis and the geometry of Au tip 2 is more close to a perfect taper. The symmetric distribution of

$I_{Au(2)-Au}(\kappa)$ may result from the surface of the Au substrate in the vicinity of the Au tip apex is assumed to be perpendicular to the optical axis. This phenomenon will be discussed in Section 5.4.

5.3.3 Emission Patterns with Variable Gap Sizes

The PL emission patterns with varied gap sizes are systematically listed in Figure 5.6. From this set of measurements, we can observe the gradual change in emission patterns. The initial gap size Δl is maintained by shear-force feedback with a $-4°$ phase shift, which is estimated as 3 nm as previously described. The displacement Δz of sample moving away from Au tip, which results in a total gap size as $\Delta l + \Delta z$. The PL emission patterns are recorded after each step movement of shear piezoelectric stacks, which makes the overall process more stable and accurate than continuous movements.

Notably, the number of lobes in $I(\theta)$ increases as the gap size enlarges. The number of lobes are observable and increases from 2 (Figure 5.6 (f)) to 10 (Figure 5.6 (s)) as Δz increases in $I_{Au-Au}(\Delta\theta_+)$. The emission pattern $I_{Au}(\kappa)$ in Figure 5.6 (o) with a very large Δz is considered 'Au tip alone' and its $I_{Au}(\Delta\theta_+)$ possesses a large number of lobes or a rather isotropic emission distribution.

Figure 5.6 (a)-(e) and (k)-(o) show $I_{Au-Au}(\kappa)$ of varied gap sizes Δz, and Figure 5.6 (f)-(j) and (p)-(t) are corresponding angular distributions $I_{Au-A}\ (\theta)$. It can be observed that the maximum intensity ratio $I^{max}(\Delta\theta_+)/I^{max}(\Delta\theta_-)$ is varied as the gap size increases. In particular, $I^{max}_{Au-Au}(\Delta\theta_+)/I^{max}_{Au-Au}(\Delta\theta_-)\sim$ 1/0.55 from Figure 5.6 (f). However, no significant intensity differences emerge between $I^{max}_{Au}(\Delta\theta_-)$ and $I^{max}_{Au}(\Delta\theta_+)$ in Figure 5.6 (t). More quantitatively, $I^{max}_{Au-Au}(\Delta\theta_+)/I^{max}_{Au-Au}(\Delta\theta_-)\sim$1/0.9.

According to what we have observed in Figure 5.6, we compare them with the numerical simulations by the Finite Element Method (FEM)[211]. We can infer that the Au tip is aligned parallel to the optical axis, and this configuration gives rise to an isotropic distribution. The surface of the Au substrate in the vicinity of the Au tip apex is assumed not perpendicular to the optical axis. This will direct the emission more in the direction

range $\Delta\theta_+$ than the direction range $\Delta\theta_-$, which gives rise to anisotropic radiation.

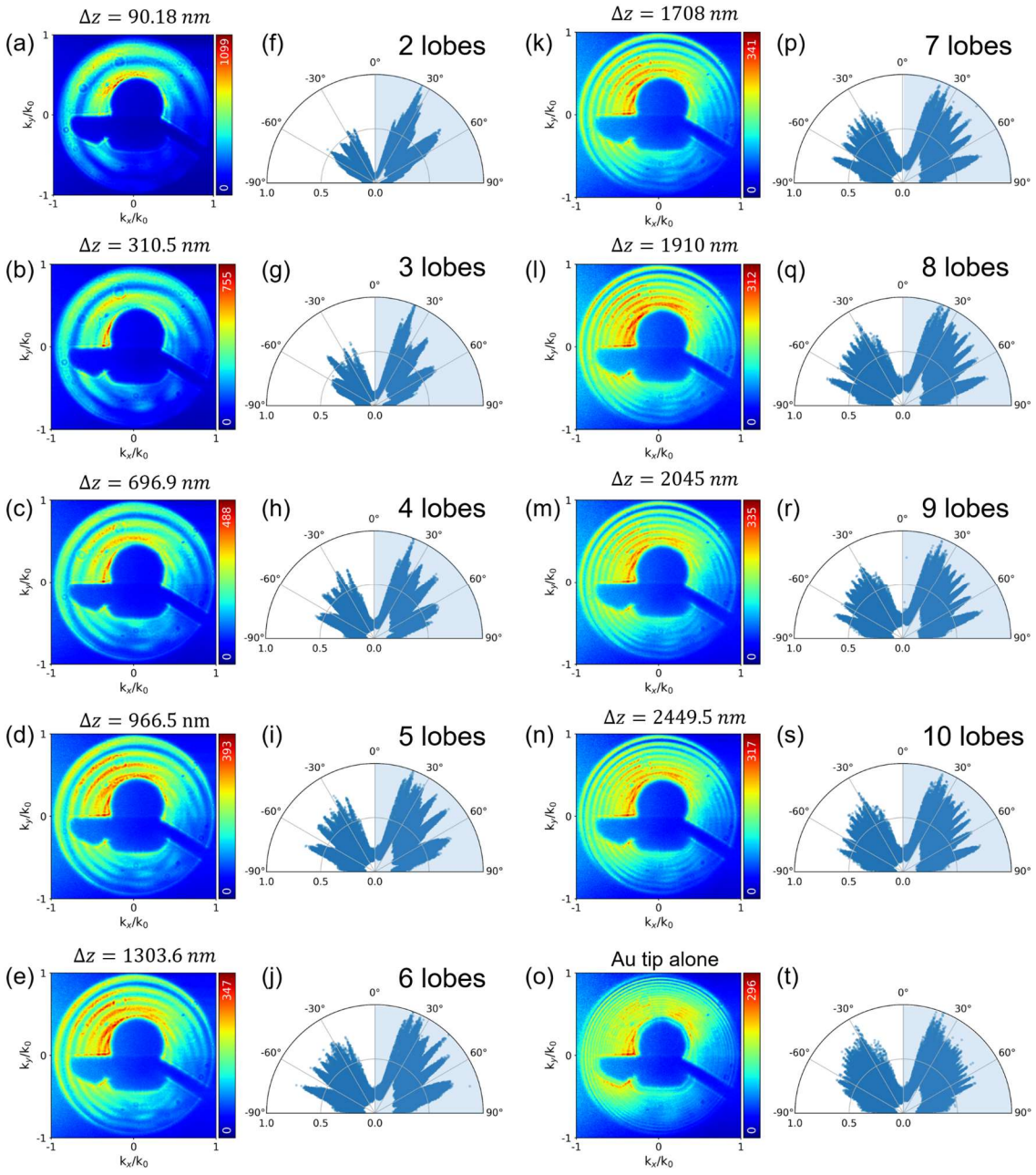

Figure 5.6 (a)-(e) and (k)-(o) are emission patterns $I(\kappa)$ of Au-Au of varied gap sizes indicated by Δz. (f)-(j) and (p)-(t) are angular distributions $I(\theta)$ of corresponding emission patterns of (a)-(e) and (k)-(o), and the distributions in $\Delta\theta_+ = 0°\sim90°$ are highlighted with light sky blue shadow. (f)-(j) and (p)-(s) show the total lobe number increases from two lobes to ten lobes in direction range $\Delta\theta_+$

5.4 Discussion

The numerical simulations by FDTD using a p-polarized plane wave[277] as a source in different geometries of conical tapers have shown that far-field scatterings will be directed in the region of $|\theta| < 30°$ and we see similar directional behaviors in our BFP images of the Au-Au configuration. However, the mechanism of the radiation process from the Au taper remains unclear.

Thus, we will discuss the plasmonic modes of a Au taper with electrodynamics simulations illuminated by a radial polarized light in the FDTD scheme in the following sections.

5.4.1 General Behaviors of Plasmonic Modes of the Au Taper

Transformation of propagating surface plasmon polaritons (SPPs) to localized surface plasmons (LSPs) is treated adiabatically[278] and non-adiabatically[279]. In the concept of adiabatic nanofocusing, the surface plasmon (SP) wave packets can propagate along a conical tapered waveguide of the slow-varying local radius with sufficiently small loss to the apex of the taper. For a given SP wave of wave number $q = Q_1 + iQ_2$, its dissipation is presumed to be weak, i.e. $Q_2 \ll Q_1$. If the taper axis is along z, the geometric parameter $\delta = |dQ_{1z}/dz| \ll 1$ holds for adiabatic compression[280]. The geometry of the Au taper matters in adiabatic nanofocusing. A cone with tapered angle $\alpha = 0.05$~0.01 radians and small taper apex is assumed to be ideal for SP waves to transport from the base to the apex of the taper. Moreover, the reciprocal picture proposed by Gau *et al.*[281] states that excitation of the LSP can also enable SPPs propagating along the taper shaft if the adiabatic compression holds.

It is worth noting that modes of different symmetries in the nanometer-sized gap induce different far-field angular distributions[282, 283]. Therefore, understanding plasmonic modes on the gold conical taper is crucial. Plasmonic eigenmodes of gold tapers have been studied[268, 281], whose wave functions in cylindrical coordinates are expressed as

$$\Psi^{(1,2)}(\rho,\phi,z)=\sum_{m=0}^{\infty}\alpha_m B_m\left(k_\rho^{(1,2)}\rho\right)e^{im\phi}e^{ik_z z} \tag{5-2}$$

where α_m is the amplitude of the mth order, $B_m = J_m$ is the Bessel function of the first kind of mth order for fields inside the taper, and $B_m = H_m^{(1)}$ is the Hankel function for fields outside the taper. The wavenumber k and the relative permittivity ϵ in domain 1 and 2 are denoted as $\left(k_\rho^{(1,2)}\right)^2 + k_z^2 = \epsilon_r^{(1,2)}k_0^2$ where $\epsilon_r^{(1)} = \epsilon_r$, $\epsilon_r^{(2)} = 1$ and k_0 is the wavenumber in free space. The ϕ-dependence of the modes enters by $e^{im\phi}$, where $m = 0,\ 1,\ 2,$ etc. are mode number m. The symmetric mode of $m = 0$ shows ϕ-independence, while other higher-order modes exhibit angular dependence in ϕ.

By viewing a conical taper as a cylinder with a gradual variation of local radius R, the dispersion can be calculated numerically according to electromagnetic (EM) theory[24, 284, 285]. The dispersion relation provides us with a clear picture of how SPPs behave on metallic cylinders. It was shown that the fundamental mode $m = 0$ does not possess radiative branch, and this mode can be bound and propagate to the taper apex. The $m = 1$ mode can be bound until local radius $R \approx 100$ nm. Higher-order modes of $|m| > 1$ cannot be bound, which are ruled out and do not contribute to near fields[268, 286]. The large opening angle of a taper will cause the high-order modes to no longer sustain on the taper shafts[286]. By the illumination of the radial polarization in our experimental conditions, the far-field radiation stems from, besides the antenna mode[287] in the vicinity of the taper apex only the fundamental azimuthal mode $m = 0$ can be sustained at the apex of the Au taper[288, 289]. This is called

5.4.2 Electrodynamics Simulations in the FDTD scheme

The mode of excitation sources plays a pivotal role in nanofocusing. A coaxial plane wave as the source does not induce SPs with adiabatic compression, which only induces HE_1-like mode[290] (or HE_1 mode). Adiabatic compression can be realized by SPP of TM_0 mode, whose H_ϕ, E_r, E_ϕ components are non-zero. This mode can be induced by illuminating with the radial polarization (see Chapter 1 for details).

Without imposing the adiabatic approximation, FDTD simulations using Meep[125] with a radial polarized wave as excitation source are performed to calculate transient states according to our experimental conditions.

Simulation Environments

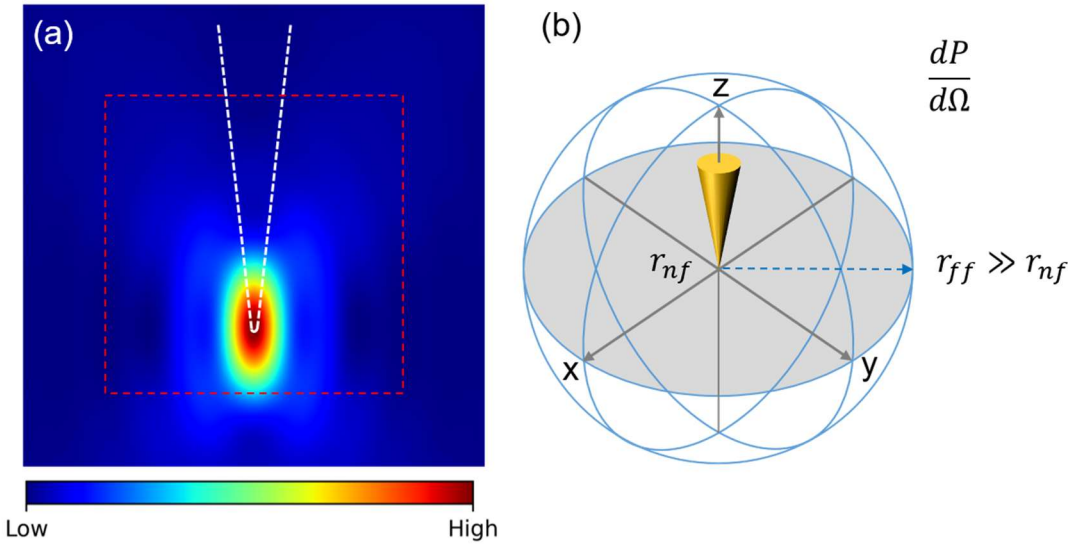

Figure 5.7 Simulation environments for (a) the electric field intensity distributions of radial polarized wave overlaid with the Au tip. The tip geometry is modeled according to tip 1 (see Figure 5.4 (b)) and shown by white dashed curves. The dashed square denotes the area without boundary layers (absorber or PML) The size of the simulation cell is 3^3 cubic μm. The field intensity distributions of 2^2 μm^2 in the yz-plane are shown here. (b) Schematic plot of far-field differential power $dP/d\Omega$ ($r_{ff} \gg r_{nf}$)

In the FDTD simulations, the simulation cell in the Cartesian coordinate system is set as 3^3 μm^3 with perfectly matched layers (PMLs) of 0.5 μm thickness along $\pm x$ and $\pm y$ directions and absorbers of 0.5 μm thickness along with $\pm z$ directions. All the following simulation results will not show the fields in the boundary layers. The boundary layers will be changed due to the extended geometry in some of the following simulation cases. The following simulations only show fields in the spatial regions without boundary layers. This region is highlighted by a red dashed square in Figure 5.7 for this case. The Au conical taper is modeled according to the morphology of Au tip 1 as shown in Figure 5.4 (b). The relative permittivity of Au is determined as $-9.98 + 1.96i$ according to the Drude-Lorentz model in Meep[125]. The explicit formulas of the radial polarization or the

RPDM are fully described in Chapter 1, which are calculated within a Python script and further implemented as the source in the simulation. The field intensity distributions for the following simulations are shown in Figure 5.7 (a). Numerical integrals in each field component of the radial polarized wave range from 0 to $\sin^{-1}(NA)$ with $NA = 0.998$. The source of wavelength $\lambda = 636$ nm propagates from the top of the simulation cell according to our setup configuration. The center of the spatial distribution of the radial polarized wave is set to coincide with the position of the taper apex.

In the following content of this chapter, we will present some simulation cases of the Au taper and the Au taper-Au substrate to elaborate on the radiation process. The size of the simulation cell in 2D shown in the following simulation cases will be $2 \times 2\ \mu m^2$. Note that the size of Case 2 is $100 \times 100\ nm^2$, which is different from the other cases.

Figure 5.7 (b) shows the simulation environment for far-field diffential power $dP/d\Omega$ with $r_{ff} \gg r_{nf}$. The steady-state electromagnetic fields are calculated after sufficient time-stepping. The corresponding time-averaged Ponyting vector are obtained and will be presented in the spherical coordinates (see Chapter 1 for more details). This part of simulation is organized into Case 5 in the following sections.

Case 1: Au taper

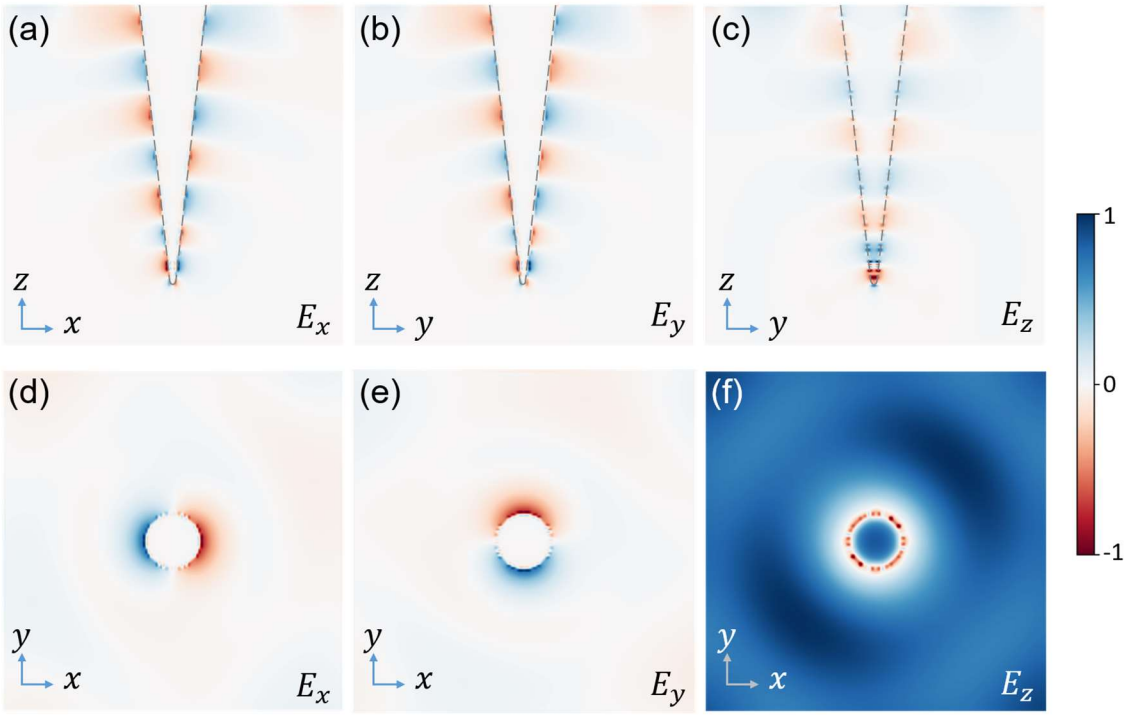

Figure 5.8 Fields of E_x, E_y, E_z by FDTD of Au taper are shown respectively at $t = 0.198$ fs. The conical taper is aligned along the z-axis, and the source of radial polarization propagates from the top of the simulation cell. The absolute values of the amplitude of each field component are normalized to 1. The upper panels (a)-(c) show the fields in the xz- or the yz- plane, and the bottom panels (d)-(f) show the fields in the xy-plane. Adiabatic compression is visualized in the field patterns as shown in the top panels.

Fields of E_x, E_y, E_z in the simulation cell without boundary layers are frozen at a time of 0.198 fs as shown in Figure 5.8. Panels (a)-(c) show the fields in the xz- or yz-plane, and panels (d)-(f) show the fields in the xy-plane. The size of each panel is $2\ \mu m \times 2\ \mu m$.

In this simulation case, adiabatic compression is clearly displayed in the top panels of Figure 5.8, which shows the shortening of the SPPs wavelength on the taper shafts and agrees with the literature[291], i.e. the distance between two nodes of fields on the taper shaft slowly decreases. The fields E_x and E_y are equivalent due to the symmetry of the source

and the geometry of the conical taper. In addition, E_x and E_y show anti-phase relation on the two sides of the Au taper, while E_z shows in-phase relation.

From the bottom panels of Figure 5.8, we observe the fields in the xy-plane at $z = 0.7\ \mu m$. The fields E_x and E_y show two lobes in the vicinity of the Au taper, which alternate in the x- and the y-direction respectively as time evolves. The field E_z possesses rotational symmetry in the xy- plane.

This time-dependent simulation by FDTD provides a clear picture of the radiation process of the plasmonic modes of the Au conical taper. After illumination by the radially polarized wave, an LSP is induced at the taper apex and radiates energy into free space. Simultaneously, the LSP generates propagating SPPs traveling along the taper shaft, which confirms the reciprocal picture of adiabatic compression.

Lcalized and propagating SPPs have been found to influence over the fluorescence of molecules[292, 293]. It is worth noting that the role of propagating SPPs on the Au taper shaft is difficult to determine quantitatively. Issa and Gurkenberger[294] consider a system of a molecule influenced by a nearby tip through numerical approach. The non-radiative decay rate γ_{nr} accounts for power dissipation in the surrounding medium. More quantitatively, γ_{nr} for the infinitely long tip can be expressed by

$$\gamma_{nr} = \frac{1}{\hbar\omega}\int_{tip} Re(\boldsymbol{J}^* \cdot \boldsymbol{E})dV \qquad (5\text{-}4)$$

where $\boldsymbol{J}^*$ is the complex conjugate of the current density $\boldsymbol{J} = \omega\varepsilon_0 \cdot Im(\varepsilon_{metal})\boldsymbol{E}$ due to Joule heating. This can be further expressed as $\gamma_{nr} = \gamma_{SPP} + \gamma_{LET}$, where γ_{SPP} is non-radiative SPP rate and γ_{LET} is the rate of non-radiative energy transfer to the apex of the tip (local energy transfer, LET)[295]. γ_{SPP} is composed of two contributions from the intrinsic thermal dissipation inside the taper and propagating SPPs on the surface at the end the taper shaft.

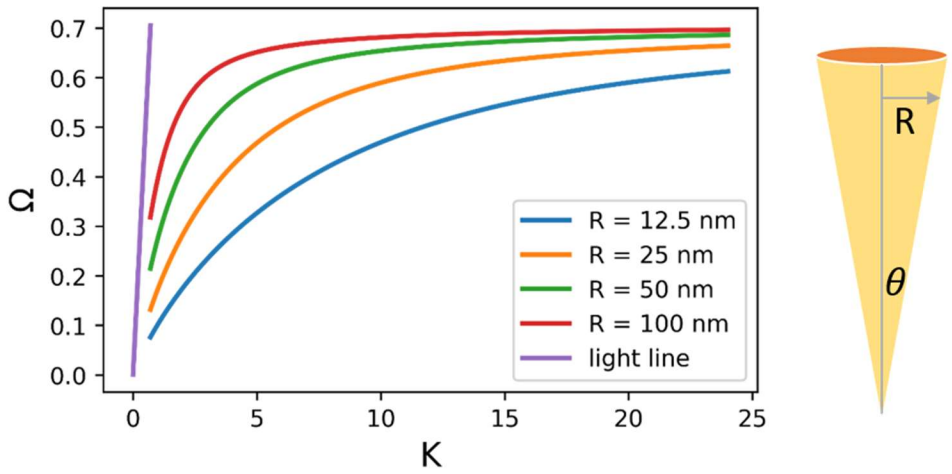

Figure 5.9 Dispersion relation of $m = 0$ mode on the Au taper with different local radius R. $\Omega = \omega/\omega_p$ and $K = k_z/k_p = k_z c/\omega_p \sim k_z/10^6 m^{-1}$

In particular, the role of the SPPs (γ_{SPP}) on the Au taper is mainly non-radiative as thermal dissipation. Let us pay attention to the dispersion relation of SPPs, which helps us to understand the radiation properties of SPPs. For the case of planar or large cylindrical materials, its dispersion relation can be written as $k_{SPP} = k_0 n_{eff}$ with effective refractive index n_{eff}

$$n_{eff} = \left[\frac{\varepsilon_1 \varepsilon_2}{\varepsilon_1 + \varepsilon_2}\right]^{1/2} \qquad (5\text{-})$$

where ε_1 and ε_2 denote the relative permittivity of metal and medium. For $Re(\varepsilon_1) < 0$ and $|Re(\varepsilon_1)| > 1$, n_{eff} will be always greater 1 for noble metals. This means $k_{SPP} > k_0$ and SPP waves only exist at metal/dielectric surfaces. Inevitably, $Im(\varepsilon_1) > 0$ renders the propagating SPPs attenuated due to ohmic loss. For small local radius R, the dispersion relation (see Figure 5.9) can be obtained numerically by solving the transcendental equation[278, 284, 296]. As discussed in the previous section, the azimuthally asymmetric modes with $m \geq 1$ are forbidden due to diverging $n_{eff}(R)$ as R is decreased in nanofocusing[297].

Momentum mismatch in the dispersion relation can be overcome to launch SPPs through grating coupling or attenuated total internal reflection (ATR)[33, 34]. It is

demonstrated that the grating can be fabricated by focus ion beam (FIB) milling onto the shaft of nanofocusing waveguides[211, 298].

The structure of the electrochemically etched Au tip with poly-crystallinity or surface roughness in our case will enable propagating SPPs to radiate instead of thermal dissipation on the long Au taper shaft. The better way to control the efficiency of decoupling SPPs out as far fields with grating couplers would be preferable. While the fabrication of Au tips of grating goes beyond the scope of the dissertation.

The field enhancement does not solely depend on the radius of curvature of the Au taper apex. Since the highly concentrated fields with much greater intensity in the gap contribute to the far-field intensity through the process of transforming the gap plasmons into SPPs. Thus, we can predict that the measured far-field intensities will be subjected to the adiabatic condition if the momentum mismatch for SPPs can be properly overcome. If one can fulfill the momentum mismatch in dispersion relation of SPP on the taper with a more well-defined structure on the taper shaft, more radiated power from the SPPs can be collected and also imaged by properly designed collection optics.

Case 2: Au Taper-Au Substrate with a Small Simulation Cell

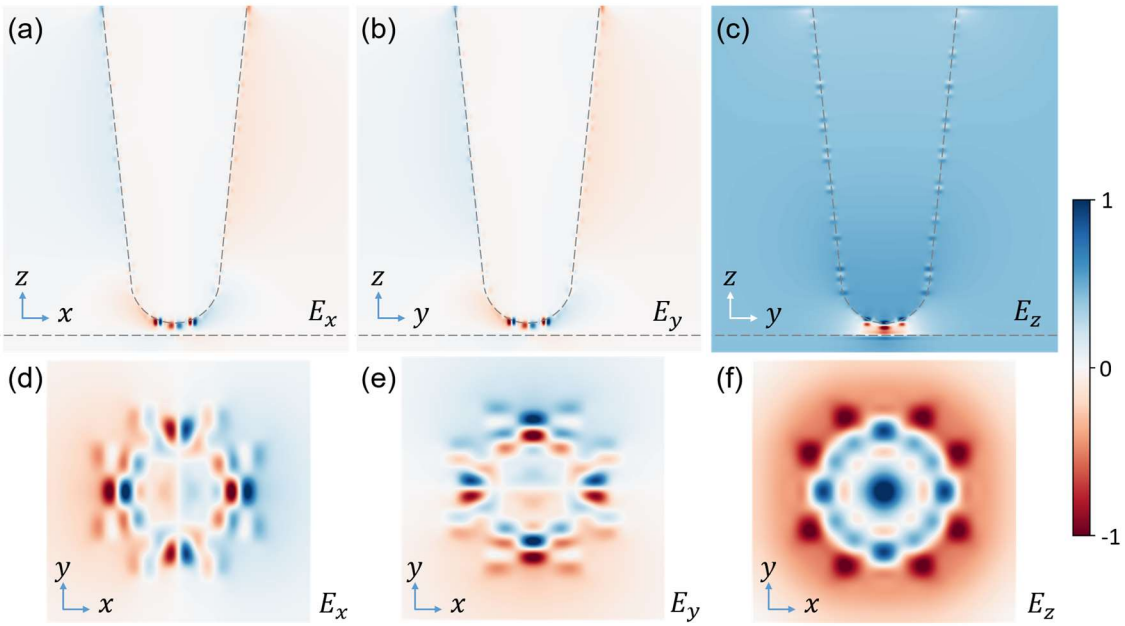

Figure 5.10 Fields of E_x, E_y, E_z by FDTD are shown and frozen at $t = 7.04$ attosecond (as). Panels (a)-(c) are the field patterns in the xz- or yz-plane. Panel (d)-(f) are field patterns of the gap mode in the xy-plane. (a)-(c) and 20 nm × 20 nm for panels (d)-(f). The absolute values of the maximal amplitudes of each component of fields are normalized to 1.

In addition to Au taper geometry, we pay attention to fields in the Au taper-Au substrate configuration in this case. Fields E_x, E_y and E_z on the taper shafts in a smaller simulation cell with a finer mesh are calculated by FDTD, which are frozen at $t = 7.04$ attosecond and shown in Figure 5.10. The simulation cell is set as 200 nm × 200 nm × 200 nm of 1 nm per pixel with absorber layers of 50 nm thickness in directions of $\pm x$, $\pm y$ and $\pm z$. The size of the simulation cell without absorber layers is 100 nm × 100 nm × 100 nm. Panels (a)-(c) show the fields in the xz- or yz- plane, and panels (d)-(f) show fields within the 3-nm gap in the xy-plane. Under these conditions of simulations, the gap mode between Au taper (tip 1) and Au substrate is visualized in Figure 5.10.

Higher-order modes in the nanometer-sized gap are clearly shown in Figure 5.10. The fields E_x, E_y and E_z of the gap mode in the xy-plane are shown in panels (d)-(f). There

are three strong local wave envelopes concentrated in the gap according to panels (a)-(c). Nodal lines appear at the center of these envelopes for the amplitudes of the fields E_x, E_y. While the field E_z shows different distributions, the gap mode is concentrated in the longitudinal direction and the nodal lines appear in the longitudinal direction. These mode amplitudes alternate in the longitudinal direction and nodal lines occur at the surface of the Au taper apex.

Case 3: Au Taper-Au Substrate with a Large Simulation Cell

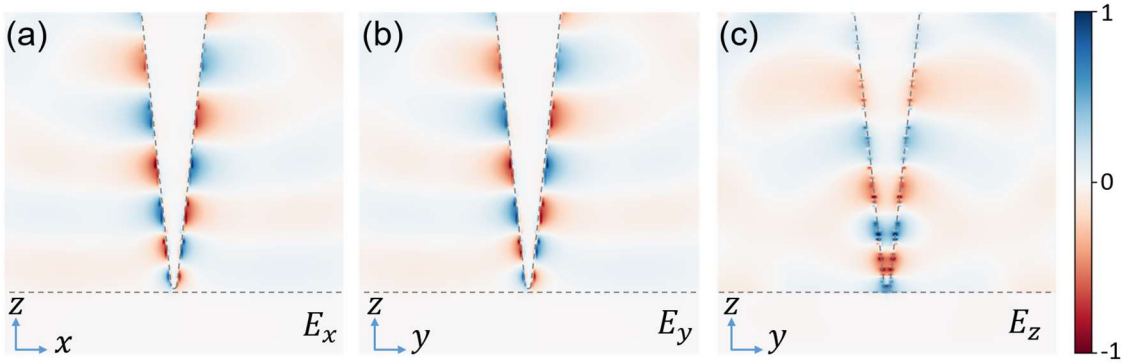

Figure 5.11 Fields E_x, E_y and E_z of the Au taper in the proximity to the Au substrate. Panels (a)-(c) show these field components respectively. The field patterns are in the xz- or yz-plane as indicated in each panel. Adiabatic compression still holds for the Au taper-Au substrate configuration. The field intensities of each field component below the surface of the Au substrate are negligible.

One should also note that SPPs also appear in Case 2 but are not clearly presented. Figure 5.11 provides clear evidence of the reciprocal picture of turning the concentrated fields in the gap into SPPs in a limited observation window. For a clear view of SPPs on the taper shafts in the Au taper-Au substrate configuration, simulations with the same simulation cell size as Case 1 (see Figure 5.8) are calculated. Figure 5.11 depicts fields E_x, E_y and E_z of the Au taper in the proximity to the Au substrate frozen at $t = 142$ attosecond. The Au substrate is introduced into the simulation environments and the boundary layers in directions of $\pm x, \pm y$ are replaced with the absorber.

In the animation, the fields are concentrated at the gap as previously demonstrated. The time-dependent radiation process is observed after the illumination of the radially polarized wave. E_x and E_y shows anti-phase relation on the two sides of the taper shafts,

while E_z shows in-phase relation. This relation remains the same as the fields on Au taper in Figure 5.8 (a)-(c). The power radiated below the Au substrate is negligible. Interestingly, the reciprocal process of adiabatic compression holds and is clearly shown in Figure 5.11. Propagating SPPs guided by the taper shaft direct the concentrated energy in the gap into free space. The field intensity is symmetric about the z-axis. This simulation predicts that the Au tip is properly aligned parallel to the optical axis (see in Figure 5.5 (k)). The emission pattern $I_{Au(2)-Au}(\kappa)$ as well as its $I_{Au(2)-Au}(\theta)$ (see in Figure 5.5 (n) (p)) may imply that there is no significant tilted tip or tilted substrate in the tip-surface configuration.

Based upon these two simulation cases of the Au taper-Au substrate (Case 2 and Case 3), we now can infer that the field enhancement depends not only on near-field intensity in the gap but also on coupling the near fields to the far fields. The simulation result shows that the gap mode does not radiate directly to free space. The reciprocal picture of adiabatic compression is visualized in the simulation that the converting of the gap plasmons into propagating SPPs along the long Au taper shaft.

Case 4: Au Taper-tilted Au Substrate

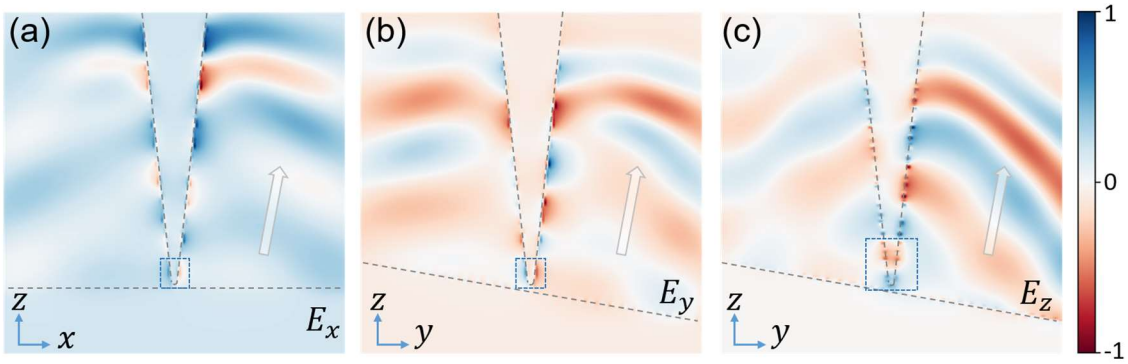

Figure 5.12 Fields E_x, E_y and E_z of the Au taper in the proximity to the Au substrate Panels (a)-(c) show these field components respectively. The field patterns are in the xz- or yz-plane as indicated in each panel. The Au substrate is tilted by 10° about x axis. Anisotropic radiation in the Au taper-tilted Au substrate configuration is visualized.

Fields E_x, E_y and E_z are calculated in the gap geometry of a Au taper-tilted Au substrate and are shown in Figure 5.12 (a)-(c) as the last simulation case. The Au substrate is tilted by 10° about the x-axis (see Figure 5.12 (b) and (c)), which significantly influences

the field patterns. All the field components exhibit anisotropic radiation. The power radiated from the Au taper-tilted Au substrate is directed more toward the sub-region of $+y$ in the yz-plane as shown in Figure 5.12 (b) (c), which are highlighted with a thick white arrow in each panel.

Notably, the phase relations between fields on the two sides of the taper shafts are affected due to the tilted substrate. The geometries of the Au taper and the Au substrate of preceding simulations possess rotational symmetry. The fields are shown in Figure 5.8 and Figure 5.11, whose E_x and E_y show anti-phase on the two sides of Au taper shaft and E_z shows in phase. These relations here do not show the same as the previous cases. In adiabatic compression of the long taper, the SPPs propagate along the sides of the taper shaft with the same slowing speeds.

It can be seen from this case that the relations exist only in the vicinity of the Au taper apex highlighted with a navy dashed square in each panel. This estimated sub-region of E_x and E_y is smaller than that of E_z, which means the tilted Au substrate has more critical influence over the phase relations of E_x and E_y than that of E_z. The reflection from the Au substrate interfere with the SPPs on the Au taper, which is assumed to cause the unequal propagating speeds of the SPPs on the two sides of Au taper shaft.

The back-scattered field intensities are relevant to what we have measured. The simulations help us to understand the reason for the anisotropic radiation patterns. The simulations with perfect geometry of Au taper and perfect alignment of Au taper-Au substrate cannot predict the radiation from tilted configurations nor from a Au tip of an irregular shape (not resembling a perfect conical taper). Case 4 includes a possible and inevitable condition in the experiments, which provides deeper insight into the radiation of the plasmonic gap. The experimental results in Section 5.3.2 do not show the dependence on the Au taper geometry but the dependence on the alignment of the Au taper and Au taper-Au substrate with respect to the optical axis.

If emission photons are directed more toward the directions of the taper shaft, the side-illumination and side-collection configuration[185] for tip-enhanced optical measurements cannot collect all enhanced optical signals. If the configuration contains a tilted Au taper or Au substrate (or both tilted at a certain angle), anisotropic radiation will

occur. On the condition that a minority of emission photons radiate at a solid angle $\Delta\Omega_{mi}$ and a majority of emission photons radiate at a preferential solid angle $\Delta\Omega_{ma}$. This part of emission photons radiated at $\Delta\Omega_{ma}$ may not be collected by the side-collection configuration with a limited solid angle. Since the tilted configuration (Au tip or Au substrate) cannot be well controlled in experiments, this may lead to limited enhancements of far-field optical intensities.

As we expect the alignment of Au taper or Au taper-Au substrate induces different radiation patterns. With the high-NA PM for emission collection, one can measure directionality variations by BFP imaging and collect most of the back-scattered photons with the large solid angle $\Delta\Omega_{PM}$. One can further predict whether or not the Au taper-Au substrate is tilted based upon the FDTD simulations.

Case 5: Differential Power

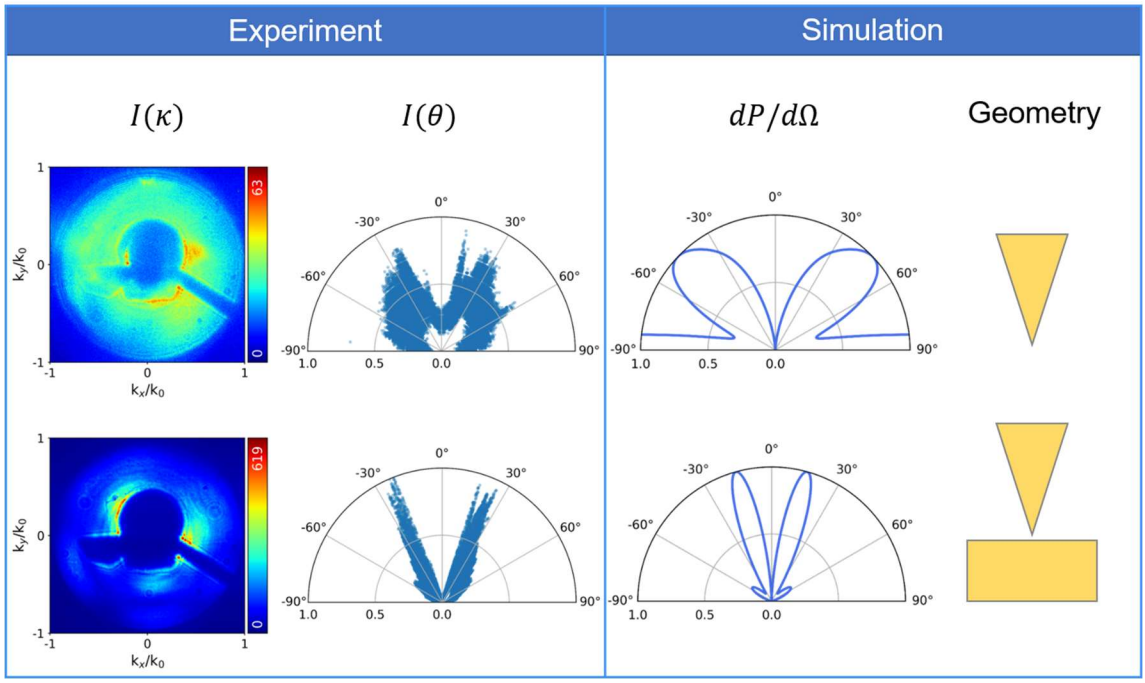

Figure 5.13 Comparisons between experimental radiation and simulated differential power in the radiation zone

The experimental results from Figure 5.5 are compared with the simulated differential power in the radiation zone (Figure 5.13). Nice agreement between the experimental and calculated results are clearly shown. The beamwidth of radiation pattern

becomes narrower in the Au tip-Au substrate configuration than that in the Au tip alone. It is now clear that the far-field intensity are greatly modified for the Au tip of larger taper angle α in the normal configuration (not tilted).

5.5 Conclusion

We systematically measure the radiation patterns of the PL of Au conical tapers and Au-Au configurations using home-built tip-enhanced optical spectroscopy. Positioning the Au taper apex in the optical focus influences the directionality of the radiation patterns. The radiation patterns of the Au tapers of two different geometries are compared. The mechanism of radiation in the Au taper is studied by calculating the transient states of fields in the vicinity of the Au taper impinged with a radial mode as the excitation source in the FDTD scheme. Radiation of the Au taper and its reciprocal picture with adiabatic compression is fully visualized based upon the calculations. Furthermore, the plasmonic gap modes of a higher-order mode are visualized, which converts the localized SPPs into propagating SPPs. The simulations with consideration of the tilted configuration show anisotropic radiation, which improves our understanding of the experiments. The physical picture of Au taper radiation is realized based upon the experiments of the BFP images and the FDTD simulations.

Chapter 6
Summary and Outlook

6.1 Summary

During my Ph.D. work, the technique of the tip-enhanced (TE) measurements using shear-force feedback has been further advanced. Approach curves of the TE optical signals using the piezoelectric scanner and back-focal plane imaging to observe far-field radiation have been fully experimentally realized.

The fundamental physics and mechanisms underlying TE optical spectroscopy and microscopy in the ambient are discussed in the Ph.D. work. The two-color SERS and TERS unravel the EM enhancement and the chemical enhancement. The tip-sample distance-dependent measurements are demonstrated to quantify the moving range and reveal its surface plasmon resonance. The optical resolution of sub-10 nm is achieved with the ambient shear-force SNOM. These works are verified by the electrodynamics simulations in the FDTD scheme and lay groundworks into chemical mapping and optical imaging using plasmonic structures. The radiation processes of Au taper and plasmonic gap illuminated by radial polarization are unraveled and the physical picture is clearly shown. This helps people to gain deeper insights into radiation and to optimize the collection efficiency or engineering of the probe in TE spectroscopy.

There are still plenty of future works to investigate and could even deepen the fundamental knowledge of the light-matter interactions at the nanometer scale. This part is organized in the next section.

6.2 Outlook

6.2.1 Shear-force SNOM Combined with the STM Feedback

All the tip-enhanced measurements in the Ph.D. work are obtained by performing shear-force SNOM. Furthermore, the STM feedback could be implemented on the same scanning probe on the quartz tuning fork[80], which can determine the zero-gap width and further realize a smaller tip-sample distance[80] than shear-force SNOM. This technique facilitates investigation of coupling in quantum tunneling regime, which will require combined FDTD and quantum mechanics[299, 300], or FDTD with consideration of nonlocality[301].

6.2.2 Quenching

It is corroborated that the Raman intensity is not quenched even as the gap size turns < 1 nm[80]. Interestingly, it is theoretically predicted that quenching does not occur for non-resonant Raman scattering. While resonant Raman enhancements are assumed to be subject to quenching for the smaller the tip-molecule distance[302] theoretically. A design with different excitation wavelengths for resonant and non-resonant Raman scattering can be realized and compared with this theoretical prediction.

6.2.3 Nanofocusing

Using plasmonic structures to perform nanofocusing is still open and it is required more applications of nanofocusing[297] in the field of optical imaging. Usually, direct excitation of the Au tip apex, as well as the sample, induces a large background in spectra. The properties of propagating SPPs transformed into LSPs can be further utilized for background-free[297] nanoscale Raman imaging. In addition, the back-focal plane (BFP) imaging technique of background-free TERS can be further realized as well.

6.2.4 Time-Resolved Raman Spectroscopy

Time-resolved Raman scattering can be realized by pump-probe spectroscopy[303-305]. Dynamic behaviors of Raman scattering could be influenced by the tip-induced plasmons. With the application of nanofocusing, the experimental of TERS with a carefully designed probe could be carried out in the future.

6.2.5 Surface Selection Rule

Moskovits formulated the surface selection rule[47, 61, 306, 307], and the polarization-dependent SERS of a single molecule is discussed. The corresponding experimental demonstration of the surface selection rule is also provided[308].

With a single-molecule sample, the corresponding TE Raman scattering can be observed using the side-illumination configuration. The TERS selection rule may be modified, which is predicted theoretically[309, 310]. The gradual change in TERS intensity with different polarizations (from s-polarized to p-polarized) due to the surface selection rule can be measured and compared with the theory.

Appendix A
Vibrational Analysis

Vibrational analysis requires Lagrangian mechanics, which had been introduced in detail in the book by Thornton and Marion[311]. *Lagrange's equations* are equations of motion resulting from the application of *Hamilton's principle*. Let us first discuss the vibrational modes from a classical point of view. And then we take a step further into the quantum mechanical descriptions.

A.1 Hamilton's Principle and Lagrangian Mechanics

Minimal principles in physics predicted the concept of minimizing certain important quantities. Hamilton's principle can be mathematically formulated as[311]

$$\delta \int_{t_1}^{t_2} (T - U) dt = 0 \qquad \text{(A-1)}$$

where the symbol δ denotes variation, T denotes kinetic energy and U denotes potential energy. Equation (A-1) shows that the actual path of a motion moving from one point to another occurs by minimizing the time integral of the difference between the kinetic energy T and the potential energy U. The difference $T - U$ will be an extremum instead of a minimum according to the variational statement. But in almost all important dynamical problems in physics, the minimum takes place.

The kinetic energy T of a particle can be expressed in terms of $\dot{x}_i$ (first-order derivative with respect to time). The potential U can be written as a function of x_i if the particle is placed in a conservative field:

$$T = T(\dot{x}_i), \quad U = U(x_i) \tag{A-2}$$

The difference between them will be defined as

$$L \equiv T - U = L(\dot{x}_i, x_i) \tag{A-3}$$

Thus equation (A-1) will be

$$\delta \int_{t_1}^{t_2} L(x_i, \dot{x}_i) dt = 0 \tag{A-4}$$

The function L can be identified with the function of the variational integral[311]

$$\delta \int_{t_1}^{t_2} f(y'(x), y(x); x) dt = 0 \tag{A-5}$$

The *Euler-Lagrange equations* are therefore derived

$$\frac{\partial L}{\partial x_i} - \frac{d}{dt}\frac{\partial L}{\partial \dot{x}_i} = 0 \tag{A-6}$$

where $i = 1,2,3 \ldots etc.$

Equation (A-6) is called the Euler-Lagrange equation (or Lagrange equation) for the particle, and L is called *Lagrangian* for the particle. This can be further applied to many mechanical problems.

A.2 Normal Modes of Vibration

The details of this part can be also found in the books[20, 29]. Let us consider a molecule of N atoms (index $i = 1,2, \ldots N$) with m_i for each atom. The coordinates of the

atoms are described in terms of displacements u_i. The kinetic energy T of the Hamltonian is written as

$$T = \frac{1}{2}\sum_{i=1}^{N} m_i \dot{u}_i^2 = \frac{1}{2}\sum_{i=1}^{3N} \dot{q}_i^2 \tag{A-7}$$

where q_i (index $i = 1,2,3 \ldots 3N$) denotes the reduced mass coordinates ($\xi_1 = u_{1x}, \xi_2 = u_{1y}, \xi_3 = u_{1z}, \xi_4 = u_{2x}$ and so on)

$$q_i = m_i^{1/2}\xi_i \tag{A-8}$$

The potential U of the Hamiltonian can be expanded with respect to the reduced mass coordinates as

$$\begin{aligned} U &= U_{q_i=0} + \sum_{i=1}^{3N} q_i \left(\frac{\partial U}{\partial q_i}\right)_{q_i=0} \\ &\quad + \frac{1}{2}\sum_{i,j=1}^{3N} q_i q_j \left(\frac{\partial^2 U}{\partial q_i \partial q_j}\right)_{q_i,q_j=0} + \cdots \\ &= U_0 + \sum_{i=1}^{3N} f_i q_i + \sum_{i,j=1}^{3N} f_{ij} q_i q_j + \cdots \end{aligned} \tag{A-9}$$

By choosing the zero energy such that the energy at equilibrium is zero, U_0 can be omitted. Notably, when all displacements q_i are zeros, the energy must be a minimum. In other words, $\left(\frac{\partial U}{\partial q_i}\right)_{q_i=0} = 0$ and leave the potential U

$$U = \frac{1}{2}\sum_{i,j=1}^{3N} q_i q_j \left(\frac{\partial^2 U}{\partial q_i \partial q_j}\right)_{q_i,q_j=0} = \frac{1}{2}\sum_{i,j=1}^{3N} f_{ij} q_i q_j \tag{A-10}$$

Newton's equations of motion can be written in terms of the Lagrangian

$$\frac{\partial L}{\partial q_i} - \frac{d}{dt}\frac{\partial L}{\partial \dot{q}_i} = 0$$
$$\leftrightarrow \frac{\partial U}{\partial q_i} - \frac{d}{dt}\frac{\partial T}{\partial \dot{q}_i} = 0 \tag{A-11}$$

A simple expression can be obtained by substitutions with expressions for T and U from above equations

$$\sum_{i=1}^{3N} \ddot{q}_i + \sum_{j=1}^{3N} f_{i,j}\, q_j = 0 \rightarrow \sum_{i=1}^{3N} \ddot{q}_i + \sum_{j=1}^{3N} f_{i,j}\, q_j = 0 \tag{A-12}$$

With a suggested solution of vibrational modes

$$q_i = A_i \cos(\omega t + \phi) \text{ for } i = 1,2, \dots 3N \tag{A-13}$$

The equations of motion are reduced to an eigenvalue problem

$$\sum_{i=1}^{3N} \left(f_{i,j} - \lambda \delta_{ij}\right) A_i = 0$$
$$\text{for } j = 1,2, \dots 3N \tag{A-14}$$

where λ denotes the eigenvalues (equivalent to ω^2)

The eigenvalues λ satisfying the *secular equations*

$$\begin{vmatrix} f_{1,1} - \lambda & f_{1,2} & \cdots & f_{1,3N} \\ f_{2,1} & f_{2,2} - \lambda & \cdots & f_{2,3N} \\ \vdots & \vdots & \ddots & \vdots \\ f_{3N,1} & f_{3N,2} & \cdots & f_{3N,3N} - \lambda \end{vmatrix} = 0 \tag{A-15}$$

The trivial solutions ($A_i = 0$) are ignored here. The value λ will cause the determinant to vanish. For a fixed eigenvalue λ_k, a corresponding A_{ik} can be obtained. Note that there are no unique solutions for A_{ik}. Thus a convenient way to express the solutions is by introducing l_{ik} for an arbitrary solution A'_{ik}

$$l_{ik} = \frac{A'_{ik}}{\left[\sum_i A'^2_{ik}\right]^{1/2}} \tag{A-16}$$

Note that the amplitudes A'_{ik} are normalized due to

$$\sum_i l_{ik}^2 = 1 \tag{A-17}$$

Hence, the amplitude for the problem can be stated as

$$A_{ik} = K_k l_{ik} \tag{A-18}$$

where K_k are determined by the initial values of q_i and $\dot{q}_i$

According to the secular equations, there are $3N$ solutions for A_i. There are 6 zero roots and the rest of the non-zero roots $(3N-6)$ are vibrational modes for nonlinear molecules. The solution form shows that each atom follows behaviors of the harmonic oscillator with amplitude $A_{ik} = K_k l_{ik}$, angular frequency $\omega_k = \lambda_k^{1/2}$ and phase ϕ_k. A mode with these characteristics is called a *normal mode of vibration*. Some of the roots of the secular equations have the same values, which are called *degenerate*. The degenerate modes will have an infinite number of l_{ik}, which are illustrated in the textbook[29]. The general solution for a normal mode can thus be written as (6 zero values for l_{ik} are included in the sum)

$$q_i = \sum_{k=1}^{3N} l_{ik}\, K_k \cos(\lambda_k^{1/2} t + \phi_k) = \sum_{k=1}^{3N} l_{ik} K_k \cos(\omega_k t + \phi_k) \tag{A-19}$$

A.3 Normal Coordinates

Definitions

The quantum mechanical treatment for molecular vibrations requires the introduction of normal coordinates Q_k (index $k = 1,2,3 \ldots 3N$). The normal coordinates are related to the reduced mass coordinates by linear equations, which can be written as

$$Q_k = \sum_{i=1}^{3N} l''_{ki}\, q_i \tag{A-20}$$

The normal coordinates are used such that the kinetic energy and potential can be expressed in terms of the normal coordinates.

$$\begin{aligned} T &= \frac{1}{2}\sum_{k=1}^{3N} \dot{Q}_k^2 \\ U &= \frac{1}{2}\sum_{k=1}^{3N} \lambda'_k Q_k^2 \end{aligned} \tag{A-21}$$

Linear Transformations

The two sets of quantities can be related by a set of linear algebraic equations, which are called *linear transformations*. The reduced-mass coordinates and the normal coordinates can be expressed as

$$q_i = \sum_{k=1}^{3N} l'_{ik}\, Q_k \tag{A-22}$$

Equations of Motions

If the normal coordinates are applied, the equations of motions become

$$\frac{\partial V}{\partial Q_i} - \frac{d}{dt}\frac{\partial T}{\partial \dot{Q}_i} = 0$$
$$\leftrightarrow \lambda'_k Q_k - \ddot{Q}_k = 0 \text{ for } k = 1,2,3, \dots 3N \tag{A-23}$$

The general solutions in terms of Q's are

$$Q_k = K'_k \cos(\lambda'^{\frac{1}{2}}_k t + \phi_k) \tag{A-24}$$

which can be further expressed in terms of q's with equation (A-22) as

$$q_i = \sum_{k=1}^{3N} l'_{ik} K'_k \cos(\lambda'^{\frac{1}{2}}_k t + \phi'_k) \tag{A-25}$$

It can be seen that $l'_{ik} = l'_{ik}$ and $\lambda'^{1/2}_k = \lambda^{1/2}_k$ by comparison of this form of a solution with the form in equation (A-19). The coefficients l'_{ik} of transformation from the original coordinates q_i to the normal coordinates Q_k are identical with l_{ik}which specify the mode composition of the normal modes.

The normal modes of zero frequencies can be properly solved by introducing special sets of coordinates, *translating-rotating coordinates*[29], which are not shown here.

A.4 Wave Mechanics

Rotation and vibration separation is applied in wave mechanics. The total wave function can be written as a product of ψ_V (vibration) and ψ_R (rotation)

$$\psi \cong \psi_V \psi_R \tag{A-26}$$

With the foundations in the previous section, the kinetic and potential energy of vibrational modes (nonlinear molecules) in terms of the normal coordinates Q_k

$$\begin{aligned} T &= \frac{1}{2}\sum_{k=1}^{3N-6} \dot{Q}_k^2 \\ V &= \frac{1}{2}\sum_{k=1}^{3N-6} \lambda_k Q_k^2 \end{aligned} \tag{A-27}$$

The vibrational wave equations can thus be written as

$$-\frac{\hbar^2}{2}\sum_{k=1}^{3N-6}\frac{\partial \psi_V}{\partial Q_k^2} + \frac{1}{2}\sum_{k=1}^{3N-6}\lambda_k Q_k^2 \psi_V = W_V \psi_V \tag{A-28}$$

where W_V denotes vibrational energy and $\hbar$ represents reduced Plank constant.

The $3N-6$ equations can be separated with

$$W_V = W(1) + W(2) + \cdots + W(3N-6) \tag{A-29}$$

and

$$\psi_V = \psi(Q_1)\psi(Q_2)\ldots\psi(Q_{3N-6}) \tag{A-30}$$

The vibrational wave equation for Q_k is written as

$$-\frac{\hbar^2}{2}\frac{\partial\psi_V(Q_k)}{\partial Q_k^2}+\frac{1}{2}\lambda_k Q_k^2\psi_V(Q_k)=W_V(k)\psi_V(Q_k) \qquad \text{(A-31)}$$

The advantage of applying the normal coordinates becomes evident now. Detailed descriptions of wave mechanics can be found in Ref. [29, 312], which are not included in the dissertation.

Appendix B
Surface Plasmon Modes and Dispersion Relation

B.1 The Maxwell Equations

We begin to solve the EM problem at the metal/medium interface by introducing the Maxwell equations[35]. Current density $\vec{J}$, electric field $\vec{E}$, displacement $\vec{D}$, charge density ρ, magnetic field $\vec{H}$, magnetic flux $\vec{B}$ are interwoven as the Maxwell equations (in SI units):

$$\begin{aligned} \nabla \cdot \vec{E} &= \rho/\epsilon_0 \\ \nabla \times \vec{E} &= -\frac{\partial \vec{B}}{\partial t} \\ \nabla \cdot \vec{B} &= 0 \\ \nabla \times \vec{H} &= \vec{J} + \frac{\partial \vec{D}}{\partial t} \end{aligned} \tag{B-1}$$

and constitutive relations:

$$\begin{aligned} \vec{B} &= \mu_0 \mu \vec{H} \\ \vec{D} &= \epsilon_0 \epsilon \vec{E} \end{aligned} \tag{B-2}$$

with permeability μ and permittivity ϵ. The constitutive relations show material properties in response to a magnetic and an electric field.

B.2 Surface Plasmons at metal/dielectric interface

Stefan A. Maier[33], Lukas Novotny, Bert Hecht[5], and Heinz Raether [34] all elaborate on the physics of surface plasmons with applications. Here, we adopt a similar notation to that of Heinz Raether[34]. A p-polarized electromagnetic (EM) wave is considered incident at metal-dielectric surface $z = 0$. Domain 1 of $z > 0$ and domain 2 of $z < 0$.

The general form of electric and magnetic fields with time harmonics are

$$\vec{E} = \begin{pmatrix} E_x \\ 0 \\ E_z \end{pmatrix} e^{i(k_x x \pm k_z z)} e^{-i\omega t}$$
$$\vec{H} = \begin{pmatrix} 0 \\ H_y \\ 0 \end{pmatrix} e^{i(k_x x \pm k_z z)} e^{-i\omega t} = H_y e^{i(k_x x \pm k_z z)} e^{-i\omega t} \tag{B-3}$$

For $z > 0$, electric and magnetic fields are

$$\vec{E} = \begin{pmatrix} E_{x,1} \\ 0 \\ E_{z,1} \end{pmatrix} e^{i(k_{x,1} x + k_{z,1} z)} e^{-i\omega t}$$
$$\vec{H} = H_{y,1} e^{i(k_{x,1} x + k_{z,1} z)} e^{-i\omega t} \tag{B-4}$$

And for $z < 0$, electric and magnetic fields are

$$\vec{E} = \begin{pmatrix} E_{x,2} \\ 0 \\ E_{z,2} \end{pmatrix} e^{i(k_{x,2} x - k_{z,2} z)} e^{-i\omega t}$$
$$\vec{H} = H_{y,2} e^{i(k_{x,2} x - k_{z,2} z)} e^{-i\omega t} \tag{B-5}$$

These fields require to meet the continuity equations of Maxwell's equations

$$E_{x,1} = E_{x,2} \tag{B-6}$$

$$\epsilon_1 E_{z,1} = \epsilon_2 E_{z,2}$$

$$k_{x,1} = k_{x,2} = k_x$$

$$H_{y,1} = H_{y,2}$$

The curl equation gives

$$\nabla \times \vec{H} = \frac{\partial \vec{D}}{\partial t}$$

$$\rightarrow \frac{\partial H_{y,j}}{\partial z} = \epsilon_j \frac{\omega}{c} E_{x,j} \text{ for } j = 1,2$$

$$\rightarrow k_{z,1} H_{y,1} = \epsilon_1 \frac{\omega}{c} E_{x,1} \text{ for } z > 0 \qquad \text{(B-7)}$$

$$-k_{z,2} H_{y,2} = \epsilon_2 \frac{\omega}{c} E_{x,2} \text{ for } z < 0$$

where c is the speed of light. Equation (B-6) together with (B-7), we have equations

$$-k_{z,2}/\epsilon_2 H_{y,2} + k_{z,1}/\epsilon_2 H_{y,1} = 0$$

$$H_{y,1} = H_{y,2} \qquad \text{(B-8)}$$

And the determinant of equations (B-8) vanishes then the dispersion relation of SP becomes

$$k_x = \frac{\omega}{c} \sqrt{\frac{\epsilon_1 \epsilon_2}{\epsilon_1 + \epsilon_2}} \qquad \text{(B-9)}$$

The $k_{z,j}$ in domains, $j = 1,2$ are deduced as

$$k_{z,j}^2 = \left[\epsilon_j \left(\frac{\omega}{c} \right)^2 - k_x^2 \right]^2 \text{ for } j = 1,2 \qquad \text{(B-10)}$$

It's assumed that ϵ_1 is complex in domain 1 as metal $\epsilon_1 = \epsilon_1{}' + i\epsilon_1{}''$ where $|\epsilon_1{}'| \gg |\epsilon_1{}''|$ is assumed and ϵ_2 is real for the dielectric. Consequently, the wavenumber k_x become complex as $k_x' + ik_x''$

$$k_x' \approx \frac{\omega}{c}\sqrt{\frac{{\epsilon_1}'\epsilon_2}{{\epsilon_1}' + \epsilon_2}}$$
$$k_x'' \approx \frac{\omega}{c}\left(\frac{{\epsilon_1}'\epsilon_2}{{\epsilon_1}' + \epsilon_2}\right)^{3/2}\frac{{\epsilon_1}''}{2(\epsilon_1')^2} \tag{B-11}$$

In z direction, fields fall to $1/e$ perpendicular to the surface and the value of skin depth as $z_{sd,j} = 1/\left|k_{z,j}\right|$ where $j = 1,2$ for domain 1,2.

$$z_{sd,1} = \left|k_{z,1}\right|^{-1} = \frac{\lambda}{2\pi}\left(\frac{\epsilon_1' + \epsilon_2}{\epsilon_2^2}\right)^{1/2}$$
$$z_{sd,2} = \left|k_{z,2}\right|^{-1} = \frac{\lambda}{2\pi}\left(\frac{\epsilon_1' + \epsilon_2}{{\epsilon_1'}^2}\right)^{1/2} \tag{B-12}$$

According to these formulas, we can quantify the skin depths of different metals as described in Chapter 1.

Appendix C
Hertz Waves

Many textbooks[35, 110, 111] provide derivations of the solution to the Hertz dipole field in different ways. The work by J. David Jackson[35] provides profound insights using multipole expansion with concise expressions of the dipole fields. The solutions to the Maxwell equations (see Appendix B) of free-space can be expressed as the homogeneous wave equation. For solutions to the inhomogeneous wave equations with sources ρ and $\vec{J}$, one has to find scalar potential Φ and vector potential $\vec{A}$.

C.1 Definitions

Here, we derive the explicit form of Hertz dipole fields in a straightforward way. Let us consider a pair of charges $\pm q$ with an infinitesimal separation l as shown in Figure 1.6. The dipole moment with time harmonic dependence along the z-axis in Cartesian coordinates is written as $\vec{p}(t) = \hat{z}q(t)l = \hat{z}q_0 l e^{i\omega t}$. The point charges change from $+q$ to $-q$ in a period of $2\pi/\omega$.

C.2 Zones of Interest

The oscillating dipole behaves differently in different spatial regions[35], which are defined as

Near (static) zone $\quad l \ll r \ll \lambda$

Intermediate (induction) zone $\quad l \ll \lambda \sim r$

Far (radiation) zone $l \ll \lambda \ll r$

C.3 Derivation

We will discuss different behaviors of the Hertz dipole in near and far zones.

The relation between charge and current

$$I = \frac{dq(t)}{dt} \tag{C-1}$$

The dipole moment is related to the current by

$$Il = \frac{dq(t)}{dt} l = q_0 li\omega = i\omega p(t) \tag{C-2}$$

Equation C-2 shows that the dipole moment has a phase delay behind the oscilating current. The current density due to the source of oscillating charges can be expressed as

$$\vec{J}(x, y, z) = \hat{z} I_0 \cdot \delta(x) \cdot \delta(y) \text{ for } |z| \leq l/2 \tag{C-3}$$

The vector potential $\vec{A}$ with the sinusoidal time dependence at an observation point $\vec{x}$ is written as

$$\vec{A}(\vec{r}) = \frac{\mu}{4\pi} \int d^3\overrightarrow{r'} \frac{\vec{J}\left(\overrightarrow{r'}\right) e^{ik|\vec{r}-\overrightarrow{r'}|}}{\left|\vec{r} - \overrightarrow{r'}\right|} \tag{C-4}$$

where $\vec{x}'$ source position and $d^3\overrightarrow{x'}$ denotes a 3D infinitesimal volume in source coordinates.

Approximation

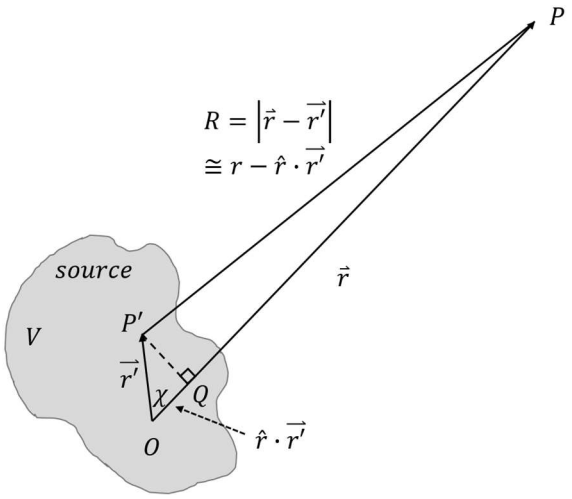

Figure C.1 The approximation for the source at $\vec{r}'$ (P') from observation $\vec{r}$ (P)

A simple approximation can be seen in Figure C.1. The source at point P' of the region V (presented by $\overrightarrow{r'}$), which is observed at point P (represented by $\vec{r}$). For the approximation $r \gg r'$, $R = PP' = OP - OQ$ brings $\left|\vec{r} - \overrightarrow{r'}\right| \cong r - \hat{r} \cdot \overrightarrow{r'} = r - r' \cos\chi$.

An alternative approximation is by obtaining the Taylor series by expanding the denominator in the integral of equation (C-4) $R = \left|\vec{r} - \overrightarrow{r'}\right|$, which is written as

$$R = |\vec{r} - \vec{r}'| = \sqrt{r^2 + r'^2 - 2rr'\cos\chi}$$

$$= r\sqrt{1 + \left(\frac{r'}{r}\right)^2 - 2\left(\frac{r'}{r}\right)\cos\chi} \qquad \text{(C-5)}$$

$$\cong r\left\{1 - \frac{r'}{r}\cos\chi + \frac{1}{2}\left(\frac{r'}{r}\right)^2 - \frac{1}{8}\left[\left(\frac{r'}{r}\right)^2 - 2\left(\frac{r'}{r}\right)\cos\chi\right]^2\right\}$$

This is approximated by $\sqrt{1+\delta} \cong 1 + \frac{1}{2}\delta - \frac{1}{8}\delta^2$ for small δ. And we can go further by expanding the last term

$$\begin{aligned} R &\cong r\left\{1 - \frac{r'}{r}\cos\chi + \frac{1}{2}\left(\frac{r'}{r}\right)^2 \right. \\ &\qquad \left. - \frac{1}{8}\left[\left(\frac{r'}{r}\right)^4 + 4\left(\frac{r'}{r}\right)^2\cos^2\chi - 4\left(\frac{r'}{r}\right)^3\cos\chi\right]\right\} \\ &\cong r\left\{1 - \frac{r'}{r}\cos\chi + \frac{1}{2}\left(\frac{r'}{r}\right)^2[1-\cos^2\chi]\right\} \\ &= r - r'\cos\chi + \frac{r'^2}{2r}\sin^2\chi \end{aligned} \tag{C-6}$$

The first two terms are exactly what we obtain from the simple approximation in Figure C.1. The higher-order terms $\frac{r'^2}{r}$ need to be considered if the observation point becomes comparable to the source point, which is not the case here.

Let us consider the vector potential $\vec{A}$ under the approximation by replacing $R \cong r - \hat{r}\cdot\vec{r}$.

$$\begin{aligned} \vec{A}(\vec{r}) &= \frac{\mu}{4\pi}\int d^3\overrightarrow{r'}\frac{\vec{J}(\overrightarrow{r'})e^{ik\left(r-\hat{r}\cdot\overrightarrow{r'}\right)}}{r-\hat{r}\cdot\overrightarrow{r'}} \\ &\cong \frac{\mu e^{ikr}}{4\pi r}\int d^3\overrightarrow{r'}\left[\vec{J}(\overrightarrow{r'})e^{-ik\hat{r}\cdot\overrightarrow{r'}}\right] \\ &\cong \frac{\mu e^{ikr}}{4\pi r}\int d^3\overrightarrow{r'}[\vec{J}(\overrightarrow{r'})] \end{aligned} \tag{C-7}$$

Note that the denominator becomes r by neglecting $\hat{r}\cdot\overrightarrow{r'}$ due to the far-field zone. The exponent $e^{-ik\hat{r}\cdot\overrightarrow{r'}} \cong 1$ requires that $kr' \ll 1$, which is satisfied by the Hertz dipole of an infinitesimal separation r'.

We continue the derivation with the vector potential under the approximation.

$$\vec{A} = \hat{z}\frac{\mu e^{ikr}}{4\pi r}\int_{-l/2}^{l/2}\int_{-\infty}^{\infty}\int_{-\infty}^{\infty} dx'dy'dz' I_0\delta(x')\delta(y') \\ = \hat{z}\frac{\mu I_0 l}{4\pi}\frac{e^{ik|\vec{r}|}}{|\vec{r}|} = \hat{z}\frac{\mu I_0 l}{4\pi}\frac{e^{ikr}}{r} \tag{C-8}$$

Through coordinate transformations

$$\hat{z} = \cos\theta\ \hat{r} - \sin\theta\ \hat{\theta} \tag{C-9}$$

The original vector potential

$$A_z = \frac{\mu I_0 l}{4\pi}\frac{e^{ikr}}{r} \tag{C-10}$$

becomes

$$A_r = \frac{\mu I_0 l}{4\pi}\frac{e^{ikr}}{r}\cos\theta \\ A_\theta = -\frac{\mu I_0 l}{4\pi}\frac{e^{ikr}}{r}\sin\theta \\ A_\phi = 0 \tag{C-11}$$

Then the magnetic field $\vec{H}$ is given by

$$\vec{H} = \frac{1}{\mu}\nabla \times \vec{A} \tag{C-12}$$

where the curl identity in spherical coordinate

$$\nabla \times \vec{A} = \frac{1}{r^2 \sin\theta} \begin{vmatrix} \hat{r} & r\hat{\theta} & r\sin\theta\,\hat{\phi} \\ \frac{\partial}{\partial r} & \frac{\partial}{\partial \theta} & \frac{\partial}{\partial \phi} \\ A_r & rA_\theta & r\sin\theta\,A_\phi \end{vmatrix} \tag{C-13}$$

The magnetic field $\vec{H}$ becomes

$$\begin{aligned} \vec{H} &= \frac{1}{\mu} \cdot \frac{1}{r^2 \sin\theta} \begin{vmatrix} \hat{r} & r\hat{\theta} & r\sin\theta\,\hat{\phi} \\ \frac{\partial}{\partial r} & \frac{\partial}{\partial \theta} & \frac{\partial}{\partial \phi} \\ \frac{I_0 l}{4\pi}\frac{e^{ikr}}{r}\cos\theta & -\frac{I_0 l}{4\pi}e^{ikr}\sin\theta & 0 \end{vmatrix} \\ &= \hat{\phi}\,\frac{1}{\mu r}\left[-ik\frac{I_0 l}{4\pi}e^{ikr}\sin\theta + \frac{I_0 l}{4\pi}\frac{e^{ikr}}{r}\sin\theta\right] \\ &= \hat{\phi}\,\frac{I_0 l e^{ikr}}{4\pi\mu r}\sin\theta\left[-ik + \frac{1}{r}\right] \end{aligned} \tag{C-14}$$

The electric field is given by

$$\vec{E} = \frac{iZ_0}{k}\nabla \times \vec{H} \tag{C-15}$$

where $Z_0 = \sqrt{\mu_0/\varepsilon_0}$ is the impedance of free space

$$\nabla \times \vec{H} = \frac{1}{\mu r^2 \sin\theta} \begin{vmatrix} \hat{r} & r\hat{\theta} & r\sin\theta\,\hat{\phi} \\ \frac{\partial}{\partial r} & \frac{\partial}{\partial \theta} & \frac{\partial}{\partial \phi} \\ 0 & 0 & \frac{e^{ikr}}{4\pi}\sin^2\theta\left[-ik + \frac{1}{r}\right] \end{vmatrix} \tag{C-16}$$

$$= \frac{I_0 l}{\mu r^2 \sin\theta}\left\{\hat{r}\frac{\partial}{\partial\theta}\left[\frac{e^{ikr}}{4\pi}\sin^2\theta\left(-ik+\frac{1}{r}\right)\right] - \hat{\theta}\, r\frac{\partial}{\partial r}\left[\frac{e^{kr}}{4\pi}\sin^2\theta\left[-ik+\frac{1}{r}\right]\right]\right\} \tag{C-17}$$

$$= \frac{I_0 l}{\mu r^2 \sin\theta}\left\{\hat{r}\frac{e^{ikr}}{4\pi}\left(-ik+\frac{1}{r}\right)\frac{\partial}{\partial\theta}[\sin^2\theta] - \hat{\theta}\,\frac{r}{4\pi}\sin^2\theta\frac{\partial}{\partial r}\left[e^{ikr}\left(-ik+\frac{1}{r}\right)\right]\right\} \tag{C-18}$$

$$= \frac{I_0 l}{\mu r^2 \sin\theta}\left\{\hat{r}\frac{e^{ikr}}{4\pi}\left(-ik+\frac{1}{r}\right)\sin 2\theta - \hat{\theta}\,\frac{r}{4\pi}\sin^2\theta\left[k^2 e^{ikr}+e^{ikr}\left(\frac{ik}{r}-\frac{1}{r^2}\right)\right]\right\} \tag{C-19}$$

$$= \hat{r}\frac{I_0 l\cdot e^{ikr}}{4\pi\mu}\left(-\frac{ik}{r^2}+\frac{1}{r^3}\right)2\cos\theta - \hat{\theta}\,\frac{I_0 l\cdot e^{ikr}}{4\pi\mu}\sin\theta\left(\frac{k^2}{r}+\frac{ik}{r^2}-\frac{1}{r^3}\right) \tag{C-20}$$

The electric field with replacement of dipole moment becomes

$$\vec{E} = \hat{r}\frac{p_0\cdot e^{ikr}}{4\pi\varepsilon}2\cos\theta\left(\frac{ik}{r^2}-\frac{1}{r^3}\right) + \hat{\theta}\,\frac{p_0\cdot e^{ikr}}{4\pi\varepsilon}\sin\theta\left(\frac{k^2}{r}+\frac{ik}{r^2}-\frac{1}{r^3}\right) \tag{C-21}$$

These fields are what we presented in Chapter 1. It can be seen that the r^{-n}-dependence (n =1, 2, 3) in each field component. These components with r^{-n} of different n will dominate in different spatial regions. We now discuss their behaviors in the different zones as defined previously.

Case I. Near Zone

In the case of the near zone, the condition $l \ll r \ll \lambda$ is satisfied. $e^{ikr} \cong 1$ due to $k \cdot r \ll 1$. The r^{-3} terms will survive under the condition. The electric field is

$$\vec{E} = \frac{p_0}{4\pi\varepsilon r^3}\left(\hat{r}2\cos\theta + \hat{\theta}\,\sin\theta\right) \tag{C-22}$$

And the magnitude of the magnetic field $\left|\vec{H}\right| \ll \left|\vec{E}\right|$, which can be neglected. Then we obtain the electrostatic solution of the dipole.

Case II. Far Zone

In the case of the far zone, the condition $l \ll r \ll \lambda$ is satisfied. The r^{-1} terms will survive under the condition, and the corresponding electromagnetic fields are written as

$$\vec{E} = \hat{\theta}\,\frac{k^2 p_0}{4\pi r\varepsilon} e^{ikr}\sin\theta \tag{C-23}$$

$$\vec{H} = -\hat{\phi}\,\frac{k\omega p_0}{4\pi r} e^{ikr}\sin\theta \tag{C-24}$$

Notably, the ratio of their magnitude is $\left|\vec{E}/\vec{H}\right| = \frac{\frac{k^2}{\varepsilon}}{k\omega} = Z_0$, the impedance of free space. For the calculations in the intermediate (induction) zone, one can find more details in the textbook by J. David Jackson[35]. The expressions in Chapter 1 (Section 1.6) are the same as the forms here.

Acknowledgments

This Ph.D. work is a challenging journey for me as a foreign student. I have never been to any European countries before. I have no experience of living abroad and using a second or even third language for years as well. I believe all the scenery in this journey is beautiful and what I have learned during these years will reshape my future life. I appreciate all the following people's help and company:

PD Dai Zhang and Prof. Alfred Meixner, my supervisors, for accepting me to work as a doctoral student at the University of Tübingen

Anke Horneber and Marius van den Berg for teaching me techniques in the lab

Dr. Diana Davila Pineda, Prof. Dr. Raul D. Rodriguez, and Katharina Greulich for preparing samples

Prof. Monika Fleischer for allowing me to use the dark-field microscope for measurements

Dr. Kai Braun for helping me use the AFM (Bruker)

Prof. Dr. Heiko Peisert for fruitful discussion about the energy diagram of metal-CoPc

Ms. Nadler, Quan Liu for measuring Au and Ag tips by SEM

The Python community on Stack Overflow, who help me with data visualization, analysis

Meep developer group of Prof. Steven G. Johnson and Linux OS, for providing a powerful numerical tool for simulations regarding my research

Andrii Trelin, Nikolaos-MAtthaiakakis for sharing useful Python scripts on Github

Tobias Köninger for accompanying me to rent an apartment enjoy beers together in Tübingen

My high school English teacher for providing me with some useful writing guides

My cousin for supporting me in many aspects of life in Germany

My friend, Yi-Chun**,** for talking with me during my vacation in Taiwan

My grandparents and parents for supporting, encouraging me, and talking to me remotely

The nurses, doctors, and the midwife for helping us to take care of our child

My wife and my daughter stay with me in Germany during my difficult time

Bibliography

1. Feynman, R.P., *There's plenty of room at the bottom.* California Institute of Technology, Engineering and Science magazine, 1960.
2. Born, M. and E. Wolf, *Principles of optics: electromagnetic theory of propagation, interference and diffraction of light*. 2013: Elsevier.
3. Abbe, E., *Beiträge zur Theorie des Mikroskops und der mikroskopischen Wahrnehmung.* Archiv für mikroskopische Anatomie, 1873. **9**(1): p. 413-468.
4. Rayleigh, L., *Investigations in optics, with special reference to the spectroscope.* Monthly Notices of the Royal Astronomical Society, 1880. **40**: p. 254.
5. Novotny, L. and B. Hecht, *Principles of nano-optics*. 2012: Cambridge university press.
6. Minsky, M., *Memoir on inventing the confocal scanning microscope.* Scanning, 1988. **10**(4): p. 128-138.
7. Hell, S.W. and J. Wichmann, *Breaking the diffraction resolution limit by stimulated emission: stimulated-emission-depletion fluorescence microscopy.* Optics letters, 1994. **19**(11): p. 780-782.
8. Klar, T.A., et al., *Fluorescence microscopy with diffraction resolution barrier broken by stimulated emission.* Proceedings of the National Academy of Sciences, 2000. **97**(15): p. 8206-8210.
9. Gustafsson, M.G., *Nonlinear structured-illumination microscopy: wide-field fluorescence imaging with theoretically unlimited resolution.* Proceedings of the National Academy of Sciences, 2005. **102**(37): p. 13081-13086.
10. Rust, M.J., M. Bates, and X. Zhuang, *Sub-diffraction-limit imaging by stochastic optical reconstruction microscopy (STORM).* Nature methods, 2006. **3**(10): p. 793-796.
11. Hess, S.T., T.P. Girirajan, and M.D. Mason, *Ultra-high resolution imaging by fluorescence photoactivation localization microscopy.* Biophysical journal, 2006. **91**(11): p. 4258-4272.
12. Leung, B.O. and K.C. Chou, *Review of super-resolution fluorescence microscopy for biology.* Applied spectroscopy, 2011. **65**(9): p. 967-980.
13. Synge, E., *XXXVIII. A suggested method for extending microscopic resolution into the ultra-microscopic region.* The London, Edinburgh, and Dublin Philosophical Magazine and Journal of Science, 1928. **6**(35): p. 356-362.
14. Ash, E. and G. Nicholls, *Super-resolution aperture scanning microscope.* Nature, 1972. **237**(5357): p. 510-512.
15. Pohl, D.W., W. Denk, and M. Lanz, *Optical stethoscopy: Image recording with resolution λ/20.* Applied physics letters, 1984. **44**(7): p. 651-653.
16. Lewis, A., et al., *Development of a 500 Å spatial resolution light microscope: I. light is efficiently transmitted through λ/16 diameter apertures.* Ultramicroscopy, 1984. **13**(3): p. 227-231.
17. Demtröder, W., *Laser Spectroscopy*. Vol. 2. 2015: Springer.

18. Valeur, B. and M.N. Berberan-Santos, *Molecular fluorescence: principles and applications*. 2012: John Wiley & Sons.
19. Haken, H. and H.C. Wolf, *Molecular physics and elements of quantum chemistry: introduction to experiments and theory*. 2013: Springer Science & Business Media.
20. Le Ru, E. and P. Etchegoin, *Principles of Surface-Enhanced Raman Spectroscopy: and related plasmonic effects*. 2008: Elsevier.
21. So, P.T. and C.Y. Dong, *Fluorescence spectrophotometry.* e LS, 2001.
22. Freed, K.F. and A. Nitzan, *Intramolecular vibrational energy redistribution and the time evolution of molecular fluorescence.* The Journal of Chemical Physics, 1980. **73**(10): p. 4765-4778.
23. Lunghi, A., et al., *Intra-molecular origin of the spin-phonon coupling in slow-relaxing molecular magnets.* Chemical science, 2017. **8**(9): p. 6051-6059.
24. Stratton, J.A., *Electromagnetic theory*. Vol. 33. 2007: John Wiley & Sons.
25. Öhrn, Y., *Elements of molecular symmetry*. 2000: John Wiley & Sons.
26. Tinkham, M., *Group theory and quantum mechanics*. 2003: Courier Corporation.
27. Hayes, W., R. Loudon, and J.F. Scott, *Scattering of light by crystals.* American Journal of Physics, 1979. **47**(6): p. 571-571.
28. Long, D.A., *The Raman effect: a unified treatment of the theory of Raman scattering by molecules*. 2002: Wiley.
29. Wilson, E.B., J.C. Decius, and P.C. Cross, *Molecular vibrations: the theory of infrared and Raman vibrational spectra*. 1980: Courier Corporation.
30. Bachmann, P., *Die analytische zahlentheorie*. Vol. 2. 1894: Teubner.
31. Landau, E., *Handbuch der Lehre von der Verteilung der Primzahlen*. Vol. 1. 2000: Рипол Классик.
32. *Vibrational Resonance Raman Scattering*, in *The Raman Effect*. 2002. p. 221-270.
33. Maier, S.A., *Plasmonics: fundamentals and applications*. 2007: Springer Science & Business Media.
34. Raether, H., *Surface plasmons on smooth surfaces*, in *Surface plasmons on smooth and rough surfaces and on gratings*. 1988, Springer. p. 4-39.
35. Jackson, J.D., *Classical electrodynamics*. 1999, American Association of Physics Teachers.
36. Ding, S.-Y., et al., *Electromagnetic theories of surface-enhanced Raman spectroscopy.* Chemical Society Reviews, 2017. **46**(13): p. 4042-4076.
37. Yuan, C., D. Zhang, and Y. Gan, *Invited Review Article: Tip modification methods for tip-enhanced Raman spectroscopy (TERS) and colloidal probe technique: A 10 year update (2006-2016) review.* Review of Scientific Instruments, 2017. **88**(3): p. 031101.
38. Meyer, R., X. Yao, and V. Deckert, *Latest instrumental developments and bioanalytical applications in tip-enhanced Raman spectroscopy.* TrAC Trends in Analytical Chemistry, 2018. **102**: p. 250-258.
39. Geddes, C.D. and J.R. Lakowicz, *Metal-enhanced fluorescence.* Journal of fluorescence, 2002. **12**(2): p. 121-129.
40. Gerton, J.M., et al., *Tip-enhanced fluorescence microscopy at 10 nanometer resolution.* Physical review letters, 2004. **93**(18): p. 180801.

41. Zrimsek, A.B., et al., *Single-molecule chemistry with surface-and tip-enhanced Raman spectroscopy.* Chemical reviews, 2017. **117**(11): p. 7583-7613.
42. Shim, S., C.M. Stuart, and R.A. Mathies, *Resonance Raman cross-sections and vibronic analysis of Rhodamine 6G from broadband stimulated Raman spectroscopy.* ChemPhysChem, 2008. **9**(5): p. 697-699.
43. Meyer, S.A., E.C.L. Ru, and P.G. Etchegoin, *Quantifying resonant Raman cross sections with SERS.* The Journal of Physical Chemistry A, 2010. **114**(17): p. 5515-5519.
44. Fleischmann, M., P.J. Hendra, and A.J. McQuillan, *Raman spectra of pyridine adsorbed at a silver electrode.* Chemical physics letters, 1974. **26**(2): p. 163-166.
45. Jeanmaire, D.L. and R.P. Van Duyne, *Surface Raman spectroelectrochemistry: Part I. Heterocyclic, aromatic, and aliphatic amines adsorbed on the anodized silver electrode.* Journal of electroanalytical chemistry and interfacial electrochemistry, 1977. **84**(1): p. 1-20.
46. Albrecht, M.G. and J.A. Creighton, *Anomalously intense Raman spectra of pyridine at a silver electrode.* Journal of the american chemical society, 1977. **99**(15): p. 5215-5217.
47. Moskovits, M. and D. DiLella, *Surface-enhanced Raman spectroscopy of benzene and benzene-d 6 adsorbed on silver.* The Journal of Chemical Physics, 1980. **73**(12): p. 6068-6075.
48. Kneipp, K., et al., *Single molecule detection using surface-enhanced Raman scattering (SERS).* Physical review letters, 1997. **78**(9): p. 1667.
49. Nie, S. and S.R. Emory, *Probing single molecules and single nanoparticles by surface-enhanced Raman scattering.* science, 1997. **275**(5303): p. 1102-1106.
50. Mulvihill, M.J., et al., *Anisotropic etching of silver nanoparticles for plasmonic structures capable of single-particle SERS.* Journal of the American Chemical Society, 2010. **132**(1): p. 268-274.
51. Sonntag, M.D., et al., *Molecular plasmonics for nanoscale spectroscopy.* Chemical Society Reviews, 2014. **43**(4): p. 1230-1247.
52. Talley, C.E., et al., *Surface-enhanced Raman scattering from individual Au nanoparticles and nanoparticle dimer substrates.* Nano letters, 2005. **5**(8): p. 1569-1574.
53. Wiley, B.J., et al., *Synthesis and optical properties of silver nanobars and nanorice.* Nano letters, 2007. **7**(4): p. 1032-1036.
54. Anderson, M.S., *Locally enhanced Raman spectroscopy with an atomic force microscope.* Applied Physics Letters, 2000. **76**(21): p. 3130-3132.
55. Hayazawa, N., et al., *Metallized tip amplification of near-field Raman scattering.* Optics Communications, 2000. **183**(1-4): p. 333-336.
56. Pettinger, B., et al., *Surface enhanced Raman spectroscopy: towards single molecule spectroscopy.* Electrochemistry, 2000. **68**(12): p. 942-949.
57. Stöckle, R.M., et al., *Nanoscale chemical analysis by tip-enhanced Raman spectroscopy.* Chemical Physics Letters, 2000. **318**(1-3): p. 131-136.
58. Zhang, R., et al., *Chemical mapping of a single molecule by plasmon-enhanced Raman scattering.* Nature, 2013. **498**(7452): p. 82.
59. Pettinger, B., *Single-molecule surface-and tip-enhanced Raman spectroscopy.* Molecular Physics, 2010. **108**(16): p. 2039-2059.

60. Lombardi, J.R., et al., *Charge-transfer theory of surface enhanced Raman spectroscopy: Herzberg–Teller contributions.* The Journal of chemical physics, 1986. **84**(8): p. 4174-4180.
61. Moskovits, M., *Surface-enhanced spectroscopy.* Reviews of modern physics, 1985. **57**(3): p. 783.
62. Schatz, G.C. and R.P. Van Duyne, *Electromagnetic mechanism of surface-enhanced spectroscopy*. 2002, Wiley: New York. p. 759-774.
63. Le Ru, E.C. and P.G. Etchegoin, *Quantifying SERS enhancements.* MRS bulletin, 2013. **38**(8): p. 631-640.
64. Le Ru, E.C., et al., *Surface enhanced Raman scattering enhancement factors: a comprehensive study.* The Journal of Physical Chemistry C, 2007. **111**(37): p. 13794-13803.
65. Camden, J.P., et al., *Probing the structure of single-molecule surface-enhanced Raman scattering hot spots.* Journal of the American Chemical Society, 2008. **130**(38): p. 12616-12617.
66. Kleinman, S.L., et al., *Creating, characterizing, and controlling chemistry with SERS hot spots.* Physical Chemistry Chemical Physics, 2013. **15**(1): p. 21-36.
67. Le Ru, E., P. Etchegoin, and M. Meyer, *Enhancement factor distribution around a single surface-enhanced Raman scattering hot spot and its relation to single molecule detection.* The Journal of chemical physics, 2006. **125**(20): p. 204701.
68. Ding, S.-Y., et al., *Nanostructure-based plasmon-enhanced Raman spectroscopy for surface analysis of materials.* Nature Reviews Materials, 2016. **1**(6): p. 1-16.
69. Alvarez-Puebla, R., L.M. Liz-Marzán, and F.J. García de Abajo, *Light concentration at the nanometer scale.* The Journal of Physical Chemistry Letters, 2010. **1**(16): p. 2428-2434.
70. Le Ru, E. and P. Etchegoin, *Rigorous justification of the| E| 4 enhancement factor in surface enhanced Raman spectroscopy.* Chemical Physics Letters, 2006. **423**(1-3): p. 63-66.
71. Wessel, J., *Surface-enhanced optical microscopy.* JOSA B, 1985. **2**(9): p. 1538-1541.
72. Tersoff, J. and D.R. Hamann, *Theory of the scanning tunneling microscope.* Physical Review B, 1985. **31**(2): p. 805.
73. Lee, J., et al., *Visualizing vibrational normal modes of a single molecule with atomically confined light.* Nature, 2019. **568**(7750): p. 78-82.
74. Huber, C., et al., *Optical near-field excitation at commercial scanning probe microscopy tips: a theoretical and experimental investigation.* Physical chemistry chemical physics, 2014. **16**(6): p. 2289-2296.
75. Meng, L., et al., *Gold-coated AFM tips for tip-enhanced Raman spectroscopy: theoretical calculation and experimental demonstration.* Optics express, 2015. **23**(11): p. 13804-13813.
76. Karrai, K. and R.D. Grober, *Piezoelectric tip-sample distance control for near field optical microscopes.* Applied physics letters, 1995. **66**(14): p. 1842-1844.
77. Sackrow, M., et al., *Imaging nanometre-sized hot spots on smooth Au films with high-resolution tip-enhanced luminescence and Raman near-field optical microscopy.* ChemPhysChem, 2008. **9**(2): p. 316-320.

78. Stanciu, C., M. Sackrow, and A. Meixner, *High NA particle-and tip-enhanced nanoscale Raman spectroscopy with a parabolic-mirror microscope.* Journal of microscopy, 2008. **229**(2): p. 247-253.
79. Tang, X., et al., *Local Observation of Phase Segregation in Mixed-Halide Perovskite.* Nano letters, 2018. **18**(3): p. 2172-2178.
80. Kravtsov, V., et al., *Control of plasmon emission and dynamics at the transition from classical to quantum coupling.* Nano letters, 2014. **14**(9): p. 5270-5275.
81. Dorn, R., S. Quabis, and G. Leuchs, *Sharper focus for a radially polarized light beam.* Physical review letters, 2003. **91**(23): p. 233901.
82. Stadler, J., et al., *Tighter focusing with a parabolic mirror.* Optics Letters, 2008. **33**(7): p. 681-683.
83. Lieb, M.A. and A.J. Meixner, *A high numerical aperture parabolic mirror as imaging device for confocal microscopy.* Optics Express, 2001. **8**(7): p. 458-474.
84. Drechsler, A., et al., *Confocal microscopy with a high numerical aperture parabolic mirror.* Optics Express, 2001. **9**(12): p. 637-644.
85. Stadler, J., et al., *Tighter focusing with a parabolic mirror.* Optics letters, 2008. **33**(7): p. 681-683.
86. Ren, B., G. Picardi, and B. Pettinger, *Preparation of gold tips suitable for tip-enhanced Raman spectroscopy and light emission by electrochemical etching.* Review of Scientific Instruments, 2004. **75**(4): p. 837-841.
87. Karrai, K. and I. Tiemann, *Interfacial shear force microscopy.* Physical Review B, 2000. **62**(19): p. 13174.
88. Ruiter, A., et al., *Tuning fork shear-force feedback.* Ultramicroscopy, 1998. **71**(1-4): p. 149-157.
89. Ruiter, A., et al., *Dynamic behavior of tuning fork shear-force feedback.* Applied physics letters, 1997. **71**(1): p. 28-30.
90. Betzig, E., P. Finn, and J. Weiner, *Combined shear force and near-field scanning optical microscopy.* Applied physics letters, 1992. **60**(20): p. 2484-2486.
91. Atia, W.A. and C.C. Davis, *A phase-locked shear-force microscope for distance regulation in near-field optical microscopy.* Applied Physics Letters, 1997. **70**(4): p. 405-407.
92. Youngworth, K.S. and T.G. Brown, *Focusing of high numerical aperture cylindrical-vector beams.* Optics Express, 2000. **7**(2): p. 77-87.
93. Züchner, T., A.V. Failla, and A.J. Meixner, *Light microscopy with doughnut modes: a concept to detect, characterize, and manipulate individual nanoobjects.* Angewandte Chemie International Edition, 2011. **50**(23): p. 5274-5293.
94. Richards, B. and E. Wolf, *Electromagnetic diffraction in optical systems, II. Structure of the image field in an aplanatic system.* Proceedings of the Royal Society of London. Series A. Mathematical and Physical Sciences, 1959. **253**(1274): p. 358-379.
95. Born, M. and R. Oppenheimer, *Zur quantentheorie der molekeln.* Annalen der physik, 1927. **389**(20): p. 457-484.
96. Bishop, D.M., *Group theory and chemistry*. 1993: Courier Corporation.
97. Anger, P., P. Bharadwaj, and L. Novotny, *Enhancement and quenching of single-molecule fluorescence.* Physical review letters, 2006. **96**(11): p. 113002.

98. Kongsuwan, N., et al., *Suppressed quenching and strong-coupling of purcell-enhanced single-molecule emission in plasmonic nanocavities.* Acs Photonics, 2018. **5**(1): p. 186-191.
99. Fleischer, M., et al., *Gold nanocone near-field scanning optical microscopy probes.* ACS nano, 2011. **5**(4): p. 2570-2579.
100. Failla, A.V., et al., *Orientational imaging of subwavelength Au particles with higher order laser modes.* Nano letters, 2006. **6**(7): p. 1374-1378.
101. Kazemi-Zanjani, N., S. Vedraine, and F. Lagugné-Labarthet, *Localized enhancement of electric field in tip-enhanced Raman spectroscopy using radially and linearly polarized light.* Optics Express, 2013. **21**(21): p. 25271-25276.
102. Chen, Y.-T., et al., *Charge transfer and electromagnetic enhancement processes revealed in the SERS and TERS of a CoPc thin film.* Nanophotonics, 2019. **8**(9): p. 1533-1546.
103. Wang, D., et al., *Directional Raman scattering from single molecules in the feed gaps of optical antennas.* Nano letters, 2013. **13**(5): p. 2194-2198.
104. Zhu, W., D. Wang, and K.B. Crozier, *Direct observation of beamed Raman scattering.* Nano letters, 2012. **12**(12): p. 6235-6243.
105. Huang, J.-S., et al., *Impedance matching and emission properties of nanoantennas in an optical nanocircuit.* Nano letters, 2009. **9**(5): p. 1897-1902.
106. Curto, A.G., et al., *Unidirectional emission of a quantum dot coupled to a nanoantenna.* Science, 2010. **329**(5994): p. 930-933.
107. Hertz, H., *Ueber sehr schnelle electrische Schwingungen.* Annalen der Physik, 1887. **267**(7): p. 421-448.
108. Hertz, H., *Ueber einen Einfluss des ultravioletten Lichtes auf die electrische Entladung.* Annalen der Physik, 1887. **267**(8): p. 983-1000.
109. Hertz, H., *'The Forces of Electric Oscillations Treated According to Maxwell's Theory,''first available in English in Nature 39, 402–404, 450–452 1889; reprinted in H. Hertz, Electric Waves*. 1962, Dover, New York.
110. Orfanidis, S.J., *Electromagnetic waves and antennas.* 2002.
111. Kong, J.A., *Electromagnetic wave theory*. 1990: Wiley-Interscience.
112. Lee, K.F., *Principles of antenna theory.* Chichester, 1984.
113. Mie, G., *Beiträge zur Optik trüber Medien, speziell kolloidaler Metallösungen.* Annalen der physik, 1908. **330**(3): p. 377-445.
114. Xu, Y.-l., *Electromagnetic scattering by an aggregate of spheres.* Applied optics, 1995. **34**(21): p. 4573-4588.
115. Lock, J.A. and G. Gouesbet, *Generalized Lorenz–Mie theory and applications.* Journal of Quantitative Spectroscopy and Radiative Transfer, 2009. **110**(11): p. 800-807.
116. Aubry, A., et al., *Interaction between plasmonic nanoparticles revisited with transformation optics.* Physical review letters, 2010. **105**(23): p. 233901.
117. Khurgin, J. and G. Sun, *Enhancement of optical properties of nanoscaled objects by metal nanoparticles.* JOSA B, 2009. **26**(12): p. B83-B95.
118. Sun, G. and J.B. Khurgin, *Theory of optical emission enhancement by coupled metal nanoparticles: An analytical approach.* Applied Physics Letters, 2011. **98**(11): p. 113116.

119. Taflove, A. and S.C. Hagness, *Computational electrodynamics: the finite-difference time-domain method*. 2005: Artech house.
120. Downes, A., D. Salter, and A. Elfick, *Finite element simulations of tip-enhanced Raman and fluorescence spectroscopy.* The Journal of Physical Chemistry B, 2006. **110**(13): p. 6692-6698.
121. Zienkiewicz, O.C. and R.L. Taylor, *The finite element method, vol. 2*. 2000: Butterworth-Heinemann.
122. De Abajo, F.G. and A. Howie, *Retarded field calculation of electron energy loss in inhomogeneous dielectrics.* Physical Review B, 2002. **65**(11): p. 115418.
123. Davis, T.J., K.C. Vernon, and D.E. Gómez, *Effect of retardation on localized surface plasmon resonances in a metallic nanorod.* Optics express, 2009. **17**(26): p. 23655-23663.
124. Yee, K., *Numerical solution of initial boundary value problems involving Maxwell's equations in isotropic media.* IEEE Transactions on antennas and propagation, 1966. **14**(3): p. 302-307.
125. Oskooi, A.F., et al., *MEEP: A flexible free-software package for electromagnetic simulations by the FDTD method.* Computer Physics Communications, 2010. **181**(3): p. 687-702.
126. Sun, J., et al., *Far-field radiation patterns of second harmonic generation from gold nanoparticles under tightly focused illumination.* Optics express, 2016. **24**(7): p. 7477-7487.
127. Cialla, D., et al., *Surface-enhanced Raman spectroscopy (SERS): progress and trends.* Analytical and bioanalytical chemistry, 2012. **403**(1): p. 27-54.
128. Tao, A., et al., *Langmuir− Blodgett silver nanowire monolayers for molecular sensing using surface-enhanced Raman spectroscopy.* Nano letters, 2003. **3**(9): p. 1229-1233.
129. de Araujo Nicolai, S.H., et al., *Electrochemical and spectroelectrochemical (SERS) studies of the reduction of methylene blue on a silver electrode.* Journal of Electroanalytical Chemistry, 2002. **527**(1-2): p. 103-111.
130. Gale, R.J., *Spectroelectrochemistry: theory and practice*. 2012: Springer Science & Business Media.
131. Hope, G., et al., *A SERS spectroelectrochemical investigation of the interaction of butylethoxycarbonylthiourea with copper surfaces.* Colloids and Surfaces A: Physicochemical and Engineering Aspects, 2004. **232**(2-3): p. 129-137.
132. Lee, Y., et al., *Enhanced Raman scattering of rhodamine 6G films on two-dimensional transition metal dichalcogenides correlated to photoinduced charge transfer.* Chemistry of Materials, 2015. **28**(1): p. 180-187.
133. Lin, J., et al., *Enhanced Raman scattering on in-plane anisotropic layered materials.* Journal of the American Chemical Society, 2015. **137**(49): p. 15511-15517.
134. Cui, L., et al., *Charge-transfer enhancement involved in the SERS of adenine on Rh and Pd demonstrated by ultraviolet to visible laser excitation.* The Journal of Physical Chemistry C, 2010. **114**(39): p. 16588-16595.
135. Uihlein, J., et al., *Influence of graphene on charge transfer between CoPc and metals: The role of graphene–substrate coupling.* The Journal of Physical Chemistry C, 2015. **119**(27): p. 15240-15247.

136. Peisert, H., et al., *Orientation and electronic properties of phthalocyanines on polycrystalline substrates.* Physica Status Solidi B-Basic Solid State Physics, 2009. **246**(7): p. 1529-1545.
137. Newville, M., et al., *LMFIT: Non-linear least-square minimization and curve-fitting for Python.* Astrophysics Source Code Library, 2016: p. ascl: 1606.014.
138. Lombardi, J.R. and R.L. Birke, *A unified view of surface-enhanced Raman scattering.* Accounts of chemical research, 2009. **42**(6): p. 734-742.
139. Lombardi, J.R. and R.L. Birke, *A unified approach to surface-enhanced Raman spectroscopy.* The Journal of Physical Chemistry C, 2008. **112**(14): p. 5605-5617.
140. Johnson, P.B. and R.-W. Christy, *Optical constants of the noble metals.* Physical review B, 1972. **6**(12): p. 4370.
141. Petraki, F., et al., *Electronic structure of Co-phthalocyanine on gold investigated by photoexcited electron spectroscopies: indication of Co ion− metal interaction.* The Journal of Physical Chemistry C, 2010. **114**(41): p. 17638-17643.
142. Kuwata, H., et al., *Resonant light scattering from metal nanoparticles: Practical analysis beyond Rayleigh approximation.* Applied physics letters, 2003. **83**(22): p. 4625-4627.
143. Keilmann, F. and R. Hillenbrand, *Near-field microscopy by elastic light scattering from a tip.* Philosophical Transactions of the Royal Society of London. Series A: Mathematical, Physical and Engineering Sciences, 2004. **362**(1817): p. 787-805.
144. Kittel, C., *Introduction to solid state physics.* 1976.
145. Giannini, V., et al., *Plasmonic nanoantennas: fundamentals and their use in controlling the radiative properties of nanoemitters.* Chemical reviews, 2011. **111**(6): p. 3888-3912.
146. Kuzmany, H., *Solid-state spectroscopy: an introduction*. 2009: Springer Science & Business Media.
147. Mihaljevic, J., C. Hafner, and A.J. Meixner, *Simulation of a metallic SNOM tip illuminated by a parabolic mirror.* Optics Express, 2013. **21**(22): p. 25926-25943.
148. Le, F., et al., *Plasmons in the metallic nanoparticle− film system as a tunable impurity problem.* Nano Letters, 2005. **5**(10): p. 2009-2013.
149. Lei, D.Y., et al., *Revealing plasmonic gap modes in particle-on-film systems using dark-field spectroscopy.* Acs Nano, 2012. **6**(2): p. 1380-1386.
150. Mock, J.J., et al., *Distance-dependent plasmon resonant coupling between a gold nanoparticle and gold film.* Nano letters, 2008. **8**(8): p. 2245-2252.
151. Gersten, J. and A. Nitzan, *Electromagnetic theory of enhanced Raman scattering by molecules adsorbed on rough surfaces.* The Journal of Chemical Physics, 1980. **73**(7): p. 3023-3037.
152. Liao, P. and A. Wokaun, *Lightning rod effect in surface enhanced Raman scattering.* The Journal of Chemical Physics, 1982. **76**(1): p. 751-752.
153. Sun, M.T., et al., *Chemical and electromagnetic mechanisms of tip-enhanced Raman scattering.* Physical Chemistry Chemical Physics, 2009. **11**(41): p. 9412-9419.
154. Chen, J., et al., *Tip-enhanced Raman scattering of p-thiocresol molecules on individual gold nanoparticles.* Applied Physics Letters, 2008. **92**(9).

155. Yang, Z.L., J. Aizpurua, and H.X. Xu, *Electromagnetic field enhancement in TERS configurations.* Journal of Raman Spectroscopy, 2009. **40**(10): p. 1343-1348.
156. . Londero, P.S., M. Leona, and J.R. Lombardi, *Definitive evidence for linked resonances in surface-enhanced Raman scattering: Excitation profile of Cu phthalocyanine.* Applied Physics Letters, 2013. **102**(11): p. 111101.
157. Birmingham, B., et al., *Probing interaction between individual submonolayer nanoislands and bulk MoS2 using ambient TERS.* The Journal of Physical Chemistry C, 2018. **122**(5): p. 2753-2760.
158. Sevinc, P.C., et al., *Simultaneous spectroscopic and topographic near-field imaging of TiO2 single surface states and interfacial electronic coupling.* Nano letters, 2011. **11**(4): p. 1490-1494.
159. Wang, X., et al., *Probing the Nanoscale Phase Separation and Photophysics Properties of Low-Bandgap Polymer: Fullerene Blend Film by Near-Field Spectroscopic Mapping.* Small, 2011. **7**(19): p. 2793-2800.
160. Wang, X., et al., *Interfacial electron transfer energetics studied by high spatial resolution tip-enhanced Raman spectroscopic imaging.* Angewandte Chemie (International ed. in English), 2011. **50**(37): p. A25-9.
161. Imura, K., T. Nagahara, and H. Okamoto, *Near-field two-photon-induced photoluminescence from single gold nanorods and imaging of plasmon modes.* The Journal of Physical Chemistry B, 2005. **109**(27): p. 13214-13220.
162. Beversluis, M.R., A. Bouhelier, and L. Novotny, *Continuum generation from single gold nanostructures through near-field mediated intraband transitions.* Physical Review B, 2003. **68**(11): p. 115433.
163. Hu, H., et al., *Plasmon-modulated photoluminescence of individual gold nanostructures.* Acs Nano, 2012. **6**(11): p. 10147-10155.
164. Wang, J., et al., *Carrier recombination and plasmonic emission channels in metallic photoluminescence.* Nanoscale, 2018. **10**(17): p. 8240-8245.
165. Vosgröne, T. and A. Meixner, *Surface-and resonance-enhanced micro-Raman spectroscopy of xanthene dyes: from the ensemble to single molecules.* ChemPhysChem, 2005. **6**(1): p. 154-163.
166. Meixner, A.J., T. Vosgröne, and M. Sackrow, *Nanoscale surface-enhanced resonance Raman scattering spectroscopy of single molecules on isolated silver clusters.* Journal of luminescence, 2001. **94**: p. 147-152.
167. Derkowska, B., et al., *Influence of the central metal atom on the nonlinear optical properties of MPcs solutions and thin films.* Optics Communications, 2007. **274**(1): p. 206-212.
168. Liao, M.-S. and S. Scheiner, *Electronic structure and bonding in metal phthalocyanines, metal= Fe, Co, Ni, Cu, Zn, Mg.* The Journal of Chemical Physics, 2001. **114**(22): p. 9780-9791.
169. Fan, W., et al., *Free-Standing Silver Nanocube/Graphene Oxide Hybrid Paper for Surface-Enhanced Raman Scattering.* Chinese Journal of Chemistry, 2016. **34**(1): p. 73-81.
170. Nalbant Esenturk, E. and A. Hight Walker, *Surface-enhanced Raman scattering spectroscopy via gold nanostars.* Journal of Raman Spectroscopy: An International Journal for Original Work in all Aspects of Raman Spectroscopy,

Including Higher Order Processes, and also Brillouin and Rayleigh Scattering, 2009. **40**(1): p. 86-91.
171. Kumar, P.S., et al., *High-yield synthesis and optical response of gold nanostars.* Nanotechnology, 2007. **19**(1): p. 015606.
172. Nelayah, J., et al., *Mapping surface plasmons on a single metallic nanoparticle.* Nature Physics, 2007. **3**(5): p. 348-353.
173. Jin, R., et al., *Photoinduced conversion of silver nanospheres to nanoprisms.* science, 2001. **294**(5548): p. 1901-1903.
174. Blatchford, C.-G., J. Campbell, and J.A. Creighton, *Plasma resonance—enhanced raman scattering by absorbates on gold colloids: the effects of aggregation.* Surface Science, 1982. **120**(2): p. 435-455.
175. Aravind, P. and H. Metiu, *The effects of the interaction between resonances in the electromagnetic response of a sphere-plane structure; applications to surface enhanced spectroscopy.* Surface science, 1983. **124**(2-3): p. 506-528.
176. Aravind, P., A. Nitzan, and H. Metiu, *The interaction between electromagnetic resonances and its role in spectroscopic studies of molecules adsorbed on colloidal particles or metal spheres.* Surface Science, 1981. **110**(1): p. 189-204.
177. McMahon, J.M., S.K. Gray, and G.C. Schatz, *Fundamental behavior of electric field enhancements in the gaps between closely spaced nanostructures.* Physical Review B, 2011. **83**(11): p. 115428.
178. He, L., et al., *The distance-dependence of colloidal Au-amplified surface plasmon resonance.* The Journal of Physical Chemistry B, 2004. **108**(30): p. 10973-10980.
179. Kennedy, B., et al., *Determination of the distance dependence and experimental effects for modified SERS substrates based on self-assembled monolayers formed using alkanethiols.* The Journal of Physical Chemistry B, 1999. **103**(18): p. 3640-3646.
180. Dieringer, J.A., et al., *Introductory lecture surface enhanced Raman spectroscopy: new materials, concepts, characterization tools, and applications.* Faraday discussions, 2006. **132**: p. 9-26.
181. Stiles, P.L., et al., *Surface-enhanced Raman spectroscopy.* Annu. Rev. Anal. Chem., 2008. **1**: p. 601-626.
182. Li, J.F., et al., *Shell-isolated nanoparticle-enhanced Raman spectroscopy.* nature, 2010. **464**(7287): p. 392-395.
183. Fang, P.P., et al., *Optimization of SERS activities of gold nanoparticles and gold-core–palladium-shell nanoparticles by controlling size and shell thickness.* Journal of Raman Spectroscopy: An International Journal for Original Work in all Aspects of Raman Spectroscopy, Including Higher Order Processes, and also Brillouin and Rayleigh Scattering, 2008. **39**(11): p. 1679-1687.
184. Shanthil, M., et al., *Ag@ SiO2 core–shell nanostructures: distance-dependent plasmon coupling and SERS investigation.* The journal of physical chemistry letters, 2012. **3**(11): p. 1459-1464.
185. Pettinger, B., et al., *Tip-enhanced Raman scattering: influence of the tip-surface geometry on optical resonance and enhancement.* Surface Science, 2009. **603**(10-12): p. 1335-1341.
186. Mooradian, A., *Photoluminescence of metals.* Physical Review Letters, 1969. **22**(5): p. 185.

187. Ashcroft, N.W. and N.D. Mermin, *Solid state physics*. 1976, holt, rinehart and winston, new york London.
188. Kittel, C., P. McEuen, and P. McEuen, *Introduction to solid state physics*. Vol. 8. 1996: Wiley New York.
189. Imura, K., T. Nagahara, and H. Okamoto, *Plasmon mode imaging of single gold nanorods.* Journal of the American Chemical Society, 2004. **126**(40): p. 12730-12731.
190. Shoenberg, D., *The Fermi surfaces of copper, silver and gold. I. the de Haas-van Alphen effect.* Philosophical Transactions of the Royal Society of London. Series A, Mathematical and Physical Sciences, 1962. **255**(1052): p. 85-133.
191. Bigioni, T., R. Whetten, and Ö. Dag, *Near-infrared luminescence from small gold nanocrystals.* The Journal of Physical Chemistry B, 2000. **104**(30): p. 6983-6986.
192. Wu, X., et al., *High-photoluminescence-yield gold nanocubes: for cell imaging and photothermal therapy.* ACS nano, 2010. **4**(1): p. 113-120.
193. Shahbazyan, T.V., *Theory of plasmon-enhanced metal photoluminescence.* Nano letters, 2013. **13**(1): p. 194-198.
194. Bouhelier, A., et al., *Surface plasmon characteristics of tunable photoluminescence in single gold nanorods.* Physical review letters, 2005. **95**(26): p. 267405.
195. Boyd, G., Z. Yu, and Y. Shen, *Photoinduced luminescence from the noble metals and its enhancement on roughened surfaces.* Physical Review B, 1986. **33**(12): p. 7923.
196. Mohamed, M.B., et al., *Thelightning'gold nanorods: fluorescence enhancement of over a million compared to the gold metal.* Chemical Physics Letters, 2000. **317**(6): p. 517-523.
197. Dulkeith, E., et al., *Plasmon emission in photoexcited gold nanoparticles.* Physical Review B, 2004. **70**(20): p. 205424.
198. Wackenhut, F., A.V. Failla, and A.J. Meixner, *Multicolor microscopy and spectroscopy reveals the physics of the one-photon luminescence in gold nanorods.* The Journal of Physical Chemistry C, 2013. **117**(34): p. 17870-17877.
199. Whitaker, D.A. and K. Hayes, *A simple algorithm for despiking Raman spectra.* Chemometrics and Intelligent Laboratory Systems, 2018. **179**: p. 82-84.
200. Eilers, P.H., *Parametric time warping.* Analytical chemistry, 2004. **76**(2): p. 404-411.
201. Neacsu, C.C., et al., *Scanning-probe Raman spectroscopy with single-molecule sensitivity.* Physical Review B, 2006. **73**(19): p. 193406.
202. Neacsu, C.C., G. Steudle, and M.B. Raschke, *Plasmonic light scattering from nanoscopic metal tips.* Applied Physics B, 2005. **80**(3): p. 295-300.
203. Sönnichsen, C., et al., *Drastic reduction of plasmon damping in gold nanorods.* Physical review letters, 2002. **88**(7): p. 077402.
204. Hu, M., et al., *Dark-field microscopy studies of single metal nanoparticles: understanding the factors that influence the linewidth of the localized surface plasmon resonance.* Journal of materials chemistry, 2008. **18**(17): p. 1949-1960.
205. Hartland, G.V., *Optical studies of dynamics in noble metal nanostructures.* Chemical reviews, 2011. **111**(6): p. 3858-3887.

206. Rechberger, W., et al., *Optical properties of two interacting gold nanoparticles.* Optics communications, 2003. **220**(1-3): p. 137-141.
207. Garcia de Abajo, F.J., *Nonlocal effects in the plasmons of strongly interacting nanoparticles, dimers, and waveguides.* The Journal of Physical Chemistry C, 2008. **112**(46): p. 17983-17987.
208. McMahon, J.M., S.K. Gray, and G.C. Schatz, *Nonlocal optical response of metal nanostructures with arbitrary shape.* Physical review letters, 2009. **103**(9): p. 097403.
209. McMahon, J.M., S.K. Gray, and G.C. Schatz, *Optical properties of nanowire dimers with a spatially nonlocal dielectric function.* Nano letters, 2010. **10**(9): p. 3473-3481.
210. Raza, S., et al., *Nonlocal optical response in metallic nanostructures.* Journal of Physics: Condensed Matter, 2015. **27**(18): p. 183204.
211. Becker, S.F., et al., *Gap-plasmon-enhanced nanofocusing near-field microscopy.* Acs Photonics, 2016. **3**(2): p. 223-232.
212. Barnes, W., *Fluorescence near interfaces: the role of photonic mode density.* journal of modern optics, 1998. **45**(4): p. 661-699.
213. Yoshino, K., et al., *Emission spectra of phthalocyanine crystals.* Journal of the Physical Society of Japan, 1973. **34**(2): p. 441-445.
214. Zuloaga, J., E. Prodan, and P. Nordlander, *Quantum description of the plasmon resonances of a nanoparticle dimer.* Nano letters, 2009. **9**(2): p. 887-891.
215. Savage, K.J., et al., *Revealing the quantum regime in tunnelling plasmonics.* Nature, 2012. **491**(7425): p. 574-577.
216. Scholl, J.A., et al., *Observation of quantum tunneling between two plasmonic nanoparticles.* Nano letters, 2013. **13**(2): p. 564-569.
217. Zhu, W., et al., *Quantum mechanical effects in plasmonic structures with subnanometre gaps.* Nature communications, 2016. **7**(1): p. 1-14.
218. Wang, X., et al., *Enhancement of radiative plasmon decay by hot electron tunneling.* ACS nano, 2015. **9**(8): p. 8176-8183.
219. Mortensen, N.A., et al., *A generalized non-local optical response theory for plasmonic nanostructures.* Nature communications, 2014. **5**(1): p. 1-7.
220. Ciracì, C., et al., *Probing the ultimate limits of plasmonic enhancement.* Science, 2012. **337**(6098): p. 1072-1074.
221. Shen, Y., F. Hu, and W. Min, *Raman imaging of small biomolecules.* Annual review of biophysics, 2019. **48**: p. 347-369.
222. Smith, G.P., et al., *Raman imaging of drug delivery systems.* Advanced drug delivery reviews, 2015. **89**: p. 21-41.
223. Stavitski, E. and B.M. Weckhuysen, *Infrared and Raman imaging of heterogeneous catalysts.* Chemical Society Reviews, 2010. **39**(12): p. 4615-4625.
224. Stewart, S., et al., *Raman imaging.* Annual Review of Analytical Chemistry, 2012. **5**: p. 337-360.
225. Ando, J., et al., *High-speed Raman imaging of cellular processes.* Current opinion in chemical biology, 2016. **33**: p. 16-24.
226. Graf, D., et al., *Raman imaging of graphene.* Solid State Communications, 2007. **143**(1-2): p. 44-46.

227. Zhang, J., et al., *Small unnatural amino acid carried Raman tag for molecular imaging of genetically targeted proteins.* The journal of physical chemistry letters, 2018. **9**(16): p. 4679-4685.
228. Palonpon, A.F., M. Sodeoka, and K. Fujita, *Molecular imaging of live cells by Raman microscopy.* Current opinion in chemical biology, 2013. **17**(4): p. 708-715.
229. Hartschuh, A., et al., *High-resolution near-field Raman microscopy of single-walled carbon nanotubes.* Physical Review Letters, 2003. **90**(9): p. 095503.
230. Steidtner, J. and B. Pettinger, *High-resolution microscope for tip-enhanced optical processes in ultrahigh vacuum.* Review of Scientific Instruments, 2007. **78**(10): p. 103104.
231. Steidtner, J. and B. Pettinger, *Tip-enhanced Raman spectroscopy and microscopy on single dye molecules with 15 nm resolution.* Physical Review Letters, 2008. **100**(23): p. 236101.
232. Chen, C., N. Hayazawa, and S. Kawata, *A 1.7 nm resolution chemical analysis of carbon nanotubes by tip-enhanced Raman imaging in the ambient.* Nature communications, 2014. **5**(1): p. 1-5.
233. Chiang, N., et al., *Conformational contrast of surface-mediated molecular switches yields Ångstrom-scale spatial resolution in ultrahigh vacuum tip-enhanced Raman spectroscopy.* Nano letters, 2016. **16**(12): p. 7774-7778.
234. Jiang, N., et al., *Nanoscale chemical imaging of a dynamic molecular phase boundary with ultrahigh vacuum tip-enhanced Raman spectroscopy.* Nano letters, 2016. **16**(6): p. 3898-3904.
235. Wang, X., et al., *High-Resolution Spectroscopic Mapping of the Chemical Contrast from Nanometer Domains in P3HT: PCBM Organic Blend Films for Solar-Cell Applications.* Advanced Functional Materials, 2010. **20**(3): p. 492-499.
236. Zhang, D., et al., *Nanoscale spectroscopic imaging of organic semiconductor films by plasmon-polariton coupling.* Physical review letters, 2010. **104**(5): p. 056601.
237. Zhang, D., et al., *Parabolic mirror-assisted tip-enhanced spectroscopic imaging for non-transparent materials.* Journal of Raman Spectroscopy: An International Journal for Original Work in all Aspects of Raman Spectroscopy, Including Higher Order Processes, and also Brillouin and Rayleigh Scattering, 2009. **40**(10): p. 1371-1376.
238. Anger, P., et al., *Near-field and confocal surface-enhanced resonance Raman spectroscopy at cryogenic temperatures.* Journal of microscopy, 2003. **209**(3): p. 162-166.
239. Jäger, S., et al., *Au nanotip as luminescent near-field probe.* Nano letters, 2013. **13**(8): p. 3566-3570.
240. van den Berg, M., et al., *Revealing the local crystallinity of single silicon core–shell nanowires using tip-enhanced Raman spectroscopy.* Beilstein journal of nanotechnology, 2020. **11**(1): p. 1147-1156.
241. Zhang, B., J. Zerubia, and J.-C. Olivo-Marin, *Gaussian approximations of fluorescence microscope point-spread function models.* Applied optics, 2007. **46**(10): p. 1819-1829.

242. Zhang, B., J. Zerubia, and J.-C. Olivo-Marin. *A study of Gaussian approximations of fluorescence microscopy PSF models*. in *Three-Dimensional and Multidimensional Microscopy: Image Acquisition and Processing XIII*. 2006. International Society for Optics and Photonics.
243. DeGarmo, E.P., et al., *Materials and process in manufacturing*. 1997: Prentice Hall Upper Saddle River.
244. Hamam, K.J., et al., *Dielectric response of branched copper phthalocyanine.* Materials Research Express, 2017. **4**(9): p. 095101.
245. Yang, M., et al., *Tip-enhanced Raman excitation spectroscopy (TERES): direct spectral characterization of the gap-mode plasmon.* Nano letters, 2019. **19**(10): p. 7309-7316.
246. Novotny, L. and N. Van Hulst, *Antennas for light.* Nature photonics, 2011. **5**(2): p. 83-90.
247. Fang, Z., et al., *Plasmonic coupling of bow tie antennas with Ag nanowire.* Nano letters, 2011. **11**(4): p. 1676-1680.
248. Rauhut, N., et al., *Antenna-enhanced photocurrent microscopy on single-walled carbon nanotubes at 30 nm resolution.* ACS nano, 2012. **6**(7): p. 6416-6421.
249. Huth, F., et al., *Resonant antenna probes for tip-enhanced infrared near-field microscopy.* Nano letters, 2013. **13**(3): p. 1065-1072.
250. Farahani, J.N., et al., *Bow-tie optical antenna probes for single-emitter scanning near-field optical microscopy.* Nanotechnology, 2007. **18**(12): p. 125506.
251. Neubrech, F., et al., *Resonant plasmonic and vibrational coupling in a tailored nanoantenna for infrared detection.* Physical review letters, 2008. **101**(15): p. 157403.
252. Taminiau, T.H., et al., *λ/4 resonance of an optical monopole antenna probed by single molecule fluorescence.* Nano letters, 2007. **7**(1): p. 28-33.
253. Kinkhabwala, A., et al., *Large single-molecule fluorescence enhancements produced by a bowtie nanoantenna.* Nature Photonics, 2009. **3**(11): p. 654-657.
254. Engheta, N., *Circuits with light at nanoscales: optical nanocircuits inspired by metamaterials.* Science, 2007. **317**(5845): p. 1698-1702.
255. Huang, K.C., et al., *Electrically driven subwavelength optical nanocircuits.* Nature Photonics, 2014. **8**(3): p. 244-249.
256. Alu, A. and N. Engheta, *Tuning the scattering response of optical nanoantennas with nanocircuit loads.* Nature photonics, 2008. **2**(5): p. 307-310.
257. Smythe, E.J., et al., *Optical antenna arrays on a fiber facet for in situ surface-enhanced Raman scattering detection.* Nano letters, 2009. **9**(3): p. 1132-1138.
258. Mitsui, K., Y. Handa, and K. Kajikawa, *Optical fiber affinity biosensor based on localized surface plasmon resonance.* Applied Physics Letters, 2004. **85**(18): p. 4231-4233.
259. Barnard, E.S., et al., *Imaging the hidden modes of ultrathin plasmonic strip antennas by cathodoluminescence.* Nano letters, 2011. **11**(10): p. 4265-4269.
260. Kim, S., et al., *High-harmonic generation by resonant plasmon field enhancement.* Nature, 2008. **453**(7196): p. 757-760.
261. Gillibert, R., et al., *Directional surface enhanced Raman scattering on gold nano-gratings.* Nanotechnology, 2016. **27**(11): p. 115202.

262. Dominguez, D., et al., *Fourier plane imaging microscopy.* Journal of Applied Physics, 2014. **116**(10): p. 103102.
263. Wagner, R., et al., *Back focal plane imaging spectroscopy of photonic crystals.* Applied Physics Letters, 2012. **101**(8): p. 081904.
264. Kim, J., et al., *Using Fourier-Plane Imaging Microscopy for Determining Transition-Dipole-Moment Orientations in Organic Light-Emitting Devices.* Physical Review Applied, 2020. **14**(3): p. 034048.
265. Hartmann, N., et al., *Radiation channels close to a plasmonic nanowire visualized by back focal plane imaging.* ACS nano, 2013. **7**(11): p. 10257-10262.
266. Budde, H., et al., *Raman radiation patterns of graphene.* ACS nano, 2016. **10**(2): p. 1756-1763.
267. Hohenau, A., et al., *Surface plasmon leakage radiation microscopy at the diffraction limit.* Optics express, 2011. **19**(25): p. 25749-25762.
268. Esmann, M., et al., *k-space imaging of the eigenmodes of sharp gold tapers for scanning near-field optical microscopy.* Beilstein journal of nanotechnology, 2013. **4**(1): p. 603-610.
269. Shegai, T., et al., *Angular distribution of surface-enhanced Raman scattering from individual Au nanoparticle aggregates.* Acs Nano, 2011. **5**(3): p. 2036-2041.
270. Chen, Y., et al., *Back focal plane imaging of Tamm plasmons and their coupled emission.* Laser & photonics reviews, 2014. **8**(6): p. 933-940.
271. Wang, D., et al., *High directivity optical antenna substrates for surface enhanced Raman scattering.* Advanced Materials, 2012. **24**(32): p. 4376-4380.
272. Hancu, I.M., et al., *Multipolar interference for directed light emission.* Nano letters, 2014. **14**(1): p. 166-171.
273. Zhang, T., et al., *Single bipyramid plasmonic antenna orientation determined by direct photoluminescence pattern imaging.* Advanced Optical Materials, 2013. **1**(4): p. 335-342.
274. Dominguez, D., et al., *Fourier plane imaging microscopy for detection of plasmonic crystals with periods beyond the optical diffraction limit.* Plasmonics, 2015. **10**(6): p. 1337-1344.
275. Hartschuh, A., *Tip-enhanced near-field optical microscopy.* Angewandte Chemie International Edition, 2008. **47**(43): p. 8178-8191.
276. Goodman, J.W., *Introduction to Fourier optics*. 2005: Roberts and Company Publishers.
277. Meng, L. and Z. Yang, *Directional surface plasmon-coupled emission of tilted-tip enhanced spectroscopy.* Nanophotonics, 2018. **7**(7): p. 1325-1332.
278. Stockman, M.I., *Nanofocusing of optical energy in tapered plasmonic waveguides.* Physical review letters, 2004. **93**(13): p. 137404.
279. Issa, N.A. and R. Guckenberger, *Optical nanofocusing on tapered metallic waveguides.* Plasmonics, 2007. **2**(1): p. 31-37.
280. Gramotnev, D.K. and S.I. Bozhevolnyi, *Nanofocusing of electromagnetic radiation.* Nature Photonics, 2014. **8**(1): p. 13.
281. Guo, S., et al., *Far-field radiation of three-dimensional plasmonic gold tapers near apexes.* ACS photonics, 2019. **6**(10): p. 2509-2516.

282. Chikkaraddy, R., et al., *How ultranarrow gap symmetries control plasmonic nanocavity modes: from cubes to spheres in the nanoparticle-on-mirror.* Acs Photonics, 2017. **4**(3): p. 469-475.
283. Baumberg, J.J., et al., *Extreme nanophotonics from ultrathin metallic gaps.* Nature materials, 2019. **18**(7): p. 668-678.
284. Pfeiffer, C., E. Economou, and K. Ngai, *Surface polaritons in a circularly cylindrical interface: surface plasmons.* Physical review B, 1974. **10**(8): p. 3038.
285. Ashley, C., *Dispersion relations for non-radiative surface plasmons on cylinders.* Surf. Sci., 1974. **41**: p. 615-618.
286. Talebi, N., et al., *Excitation of mesoscopic plasmonic tapers by relativistic electrons: phase matching versus eigenmode resonances.* ACS nano, 2015. **9**(7): p. 7641-7648.
287. Tserkezis, C., et al., *Hybridization of plasmonic antenna and cavity modes: Extreme optics of nanoparticle-on-mirror nanogaps.* Physical Review A, 2015. **92**(5): p. 053811.
288. Böckmann, H., et al., *Near-field manipulation in a scanning tunneling microscope junction with plasmonic Fabry-Pérot tips.* Nano letters, 2019. **19**(6): p. 3597-3602.
289. Chang, D., et al., *Quantum optics with surface plasmons.* Physical review letters, 2006. **97**(5): p. 053002.
290. Balanis, C., *Advanced Engineering Electromagnetics Wiley.* New York, 1989.
291. Zaccaria, R.P., et al., *Surface plasmon polariton compression through radially and linearly polarized source.* Optics letters, 2012. **37**(4): p. 545-547.
292. Stefani, F., et al., *Surface-plasmon-mediated single-molecule fluorescence through a thin metallic film.* Physical review letters, 2005. **94**(2): p. 023005.
293. Sugawa, K., et al., *Metal-enhanced fluorescence platforms based on plasmonic ordered copper arrays: wavelength dependence of quenching and enhancement effects.* ACS nano, 2013. **7**(11): p. 9997-10010.
294. Issa, N.A. and R. Guckenberger, *Fluorescence near metal tips: The roles of energy transfer and surface plasmon polaritons.* Optics Express, 2007. **15**(19): p. 12131-12144.
295. Ford, G.W. and W.H. Weber, *Electromagnetic interactions of molecules with metal surfaces.* Physics Reports, 1984. **113**(4): p. 195-287.
296. Ruppin, R., *Effect of non-locality on nanofocusing of surface plasmon field intensity in a conical tip.* Physics Letters A, 2005. **340**(1-4): p. 299-302.
297. Berweger, S., et al., *Light on the Tip of a Needle: Plasmonic Nanofocusing for Spectroscopy on the Nanoscale.* The Journal of Physical Chemistry Letters, 2012. **3**(7): p. 945-952.
298. Ropers, C., et al., *Grating-coupling of surface plasmons onto metallic tips: a nanoconfined light source.* Nano letters, 2007. **7**(9): p. 2784-2788.
299. Chen, H., et al., *Classical electrodynamics coupled to quantum mechanics for calculation of molecular optical properties: a RT-TDDFT/FDTD approach.* The Journal of Physical Chemistry C, 2010. **114**(34): p. 14384-14392.
300. Mullin, J., et al., *Combined quantum mechanics (TDDFT) and classical electrodynamics (Mie theory) methods for calculating surface enhanced Raman*

and hyper-Raman spectra. The Journal of Physical Chemistry A, 2012. **116**(38): p. 9574-9581.
301. McMahon, J.M., S.K. Gray, and G.C. Schatz, *Calculating nonlocal optical properties of structures with arbitrary shape.* Physical Review B, 2010. **82**(3): p. 035423.
302. Sun, G. and J. Khurgin, *Origin of giant difference between fluorescence, resonance, and nonresonance Raman scattering enhancement by surface plasmons.* Physical Review A, 2012. **85**(6): p. 063410.
303. Pozzi, E.A., et al., *Ultrahigh-vacuum tip-enhanced Raman spectroscopy.* Chemical reviews, 2017. **117**(7): p. 4961-4982.
304. Sun, Z., et al., *Wave packet theory of dynamic stimulated Raman spectra in femtosecond pump-probe spectroscopy.* The Journal of chemical physics, 2007. **126**(17): p. 174104.
305. Hashimoto, H. and Y. Koyama, *The C C stretching Raman lines of [β-carotene isomers in the S1 state as detected by pump-probe resonance Raman spectroscopy.* Chemical physics letters, 1989. **154**(4): p. 321-325.
306. Moskovits, M., *Surface selection rules.* The Journal of Chemical Physics, 1982. **77**(9): p. 4408-4416.
307. Moskovits, M. and J. Suh, *Surface selection rules for surface-enhanced Raman spectroscopy: calculations and application to the surface-enhanced Raman spectrum of phthalazine on silver.* The Journal of Physical Chemistry, 1984. **88**(23): p. 5526-5530.
308. Le Ru, E., et al., *Experimental demonstration of surface selection rules for SERS on flat metallic surfaces.* Chemical Communications, 2011. **47**(13): p. 3903-3905.
309. Liu, P., D.V. Chulhai, and L. Jensen, *Single-molecule imaging using atomistic near-field tip-enhanced Raman spectroscopy.* ACS nano, 2017. **11**(5): p. 5094-5102.
310. Chen, X., et al., *High-resolution tip-enhanced Raman scattering probes sub-molecular density changes.* Nature communications, 2019. **10**(1): p. 1-9.
311. Marion, J.B., *Classical dynamics of particles and systems*. 2013: Academic Press.
312. Pauling, L. and E.B. Wilson, *Introduction to quantum mechanics with applications to chemistry*. 2012: Courier Corporation.